

NORTHWESTERN UNIVERSITY

Metal-Organic Frameworks as Hydrogen Storage Materials:
Effects of Framework Reduction and Cation Doping

A DISSERTATION

SUBMITTED TO THE GRADUATE SCHOOL
IN PARTIAL FULFILLMENT OF THE REQUIREMENTS

for the degree

DOCTOR OF PHILOSOPHY

Field of Chemistry

By

Karen Lynn Mulfort

EVANSTON, ILLINOIS

December 2008

© Copyright by Karen Lynn Mulfort 2008
All rights reserved

ABSTRACT

Metal-Organic Frameworks as Hydrogen Storage Materials: Effects of Framework Reduction and Cation Doping

Karen L. Mulfort

The safe and efficient storage of hydrogen is possibly the chief obstacle to its use as a fuel on a large scale. Metal-organic frameworks (MOFs) are well poised to provide unique solutions to hydrogen storage, and gas storage in general, a result of their crystalline, porous networks that present the potential for immense structural and chemical tunability. However, the H₂-MOF interactions that govern the storage properties are too weak to realistically use MOFs as a storage medium. The focus of this research is to discover and fully understand methods by which to augment the interactions of hydrogen with MOFs in particular and potentially solid porous materials more generally.

Several new mixed-ligand MOFs based on Zn(II)-paddlewheel geometry have been designed and synthesized. Chemical reduction of the framework struts through either direct contact with solvated lithium metal or alkali-metal naphthalenide solutions and subsequent framework doping with Li⁺, Na⁺, or K⁺ has been successfully accomplished. At low cation loading levels, H₂ uptake is significantly enhanced, but with little change in the H₂ binding energy. Parallel nitrogen adsorption studies suggest that the enhanced uptake is not necessarily from H₂-cation interactions, but more likely structural changes induced by the dopant cations. Additionally, lithium and magnesium alkoxide-functionalized frameworks were pursued to introduce strong

specific H₂ binding sites with two new framework materials. These metal-alkoxide frameworks exhibit increasing H₂ heat of adsorption with loading, uncharacteristic of normal H₂ physisorption. This behavior, coupled with slight increases in uptake, suggests site specific H₂ binding within the alkoxide functionalized frameworks.

ACKNOWLEDGMENTS

Although only my name ends up on the cover page, I realize that there have been quite a few supporting authors along with way, and I'd like to thank them here. I probably never would have made it to Northwestern in the first place had it not been for my parents, Ted and Barb Mulfort. They've given me the foundation and continuing encouragement from which I can be independent, trust in myself, and find value in a hard day's work. I can never repay them for this, but I thank them for it every day. My siblings Ellen, Greg, and Patrick make me really proud to be a member of our family. I thank them for not rolling their eyes too obviously when I talk about chemistry at the dinner table.

Joe Hupp has an excitement for science that's extremely contagious and inspiring...after every meeting with him I can't help but run back in to the lab and try to save the world. I've been lucky to be able to work with Dave Tiede at Argonne, learning the nuances of X-ray scattering. I'd like to thank my thesis committee, Professors Randy Snurr, Ken Poeppelmeier, and Jim Ibers for keeping me on my toes every time we meet.

I've been lucky to encounter some amazing people in the Hupp group who just so happen to be excellent chemists as well. My classmates Alex Martinson, Tendai Gadzikwa, and Mohammed Parpia deserve special mention. They've let me bounce crazy ideas off them, joined me in complaining about unintelligible data, and helped me relish jumping through each hoop along the way. Pete Dinolfo left me not only with a great office space but also a few molecules that made it in to this thesis. Baoqing Ma taught me a little something about crystals and I'm lucky to have apprenticed with such an accomplished crystallographer. Omar Farha has shared with me his synthetic skills, chemical insights, and general excitement for neat ideas.

And of course, Marcus Stephens. He helps me celebrate my accomplishments, reminds me that my failures are temporary, and makes every other day sparkle when it might not otherwise. I thank him for sticking with me through it all.

TABLE OF CONTENTS

ABSTRACT	3
ACKNOWLEDGMENTS	5
TABLE OF CONTENTS	7
LIST OF TABLES	13
LIST OF FIGURES	15
LIST OF SCHEMES	21
 Chapter 1. Introduction to Hydrogen Storage and Metal-Organic Frameworks	 22
1.1. Motivation	23
1.1.1. Energy concerns	23
1.1.2. Hydrogen as an energy carrier	24
1.2. Hydrogen Storage	27
1.2.1. Liquid or compressed gas storage	27
1.2.2. Chemical storage: H ₂ absorption	27
1.2.3. Physisorptive storage: H ₂ adsorption	28
1.3. Metal-Organic Frameworks	29
1.3.1 Background	29
1.3.2 Strategies for H ₂ storage in MOFs	32
1.4. Thesis Directions and Introduction	34

Chapter 2. Microporous Pillared Paddlewheel Frameworks Based on Mixed Ligand Coordination of Zinc Ions	37
2. Chapter Overview	38
2.1. Introduction	38
2.2. Experimental	43
2.2.1. Materials and methods	43
2.2.2. Ligand synthesis	43
2.2.3. MOF synthesis	45
2.2.4. Crystal structure determination	51
2.2.5. Adsorption measurements	58
2.2.6. H ₂ isosteric heat of adsorption calculation	58
2.3. Results and Discussion	58
2.3.1. Synthesis	58
2.3.2. Two-fold interpenetrated Zn(II) paddlewheels (1 – 8)	59
2.3.3. Three-fold interpenetrated Zn(II) paddlewheels (9, 10)	70
2.3.4. Perylene-diimide Zn(II) paddlewheels (11, 12)	72
2.3.5. Non-interpenetrated Zn(II) paddlewheels (13 – 15)	76
2.4. Conclusions	81
Chapter 3. Chemical Reduction of Metal-Organic Framework Materials as a Method to Enhance Gas Uptake and Binding	82
3. Chapter Overview	83
3.1. Introduction	83
3.2. Experimental	84
3.2.1. Materials and methods	84

	9
3.2.2. Framework reduction	85
3.3. Results and Discussion	85
3.3.1. Framework reduction	85
3.3.2. Nitrogen adsorption of 4 and 4·Li⁺	90
3.3.3. Hydrogen adsorption of 4 and 4·Li⁺	93
3.4. Conclusions	95
Chapter 4. Alkali Metal Cation Effects in Hydrogen Uptake and Binding in Metal-Organic Frameworks	96
4. Chapter Overview	97
4.1. Introduction	97
4.2. Experimental	98
4.2.1. Methods	98
4.2.2. Framework reduction	99
4.2.3. Adsorption measurements	100
4.3. Results and Discussion	100
4.3.1. Framework reduction	100
4.3.2. Hydrogen adsorption of 4 and 4·M	101
4.3.3. Nitrogen adsorption of 4 and 4·M	107
4.4. Conclusions	113
Chapter 5. Framework Reduction and Alkali-Metal Doping of a Triply Catenating Metal-Organic Framework Enhances and then Diminishes H₂ Uptake	114
5. Chapter Overview	115

	10
5.1. Introduction	115
5.2. Experimental	120
5.2.1. General methods	120
5.2.2. Framework reduction	120
5.2.3. Adsorption measurements	120
5.2.4. EPR measurements	120
5.3. Results and Discussion	121
5.3.1. Structure of 9	121
5.3.2. Framework reduction	121
5.3.3. Hydrogen adsorption of 9 and 9·M	127
5.3.4. ¹ H NMR analysis of 9 and 9·M	131
5.3.5. Nitrogen adsorption of 9 and 9·M	134
5.4. Conclusions	139
Chapter 6. Hydrogen Binding in Alkoxide Functionalized Metal-Organic Frameworks	140
6. Chapter Overview	141
6.1. Introduction	142
6.2. Experimental	145
6.2.1. Materials and methods	145
6.2.2. Synthesis of 16	145
6.2.3. Synthesis of 17	146
6.2.4. Crystallographic analysis of 16 and 17	146
6.2.5. Alkoxide formation	148

	11
6.2.6. Low-pressure adsorption measurements	149
6.2.7. Atomic layer deposition	149
6.3. Results and Discussion	149
6.3.1. Structure of 16	149
6.3.2. Formation and characterization of 16-Li	152
6.3.3. Nitrogen and hydrogen adsorption of 16	154
6.3.4. Structure of 17	156
6.3.5. Nitrogen and hydrogen adsorption of 17	159
6.3.6. Formation and characterization of 17-Li	163
6.3.7. Formation and characterization of 17-Mg	169
6.3.8. Atomic layer deposition of Mg^{2+} in 17	173
6.3.9. Nitrogen and hydrogen adsorption of 17-Mg-ALD	174
6.4. Conclusions	177
Chapter 7. An Interpenetrated Framework Material with Gated N_2	
Sorption and Hysteretic CO_2 Uptake	179
7. Chapter Overview	180
7.1. Introduction	181
7.2. Experimental	182
7.2.1. Materials and methods	182
7.2.2. Synthesis of 18	182
7.2.3. Crystallographic analysis of 18	183
7.2.4. Low-pressure adsorption measurements	185
7.2.5. High-pressure CO_2 adsorption measurements	185

	12
7.3. Results and Discussion	186
7.3.1. Structure of 18	186
7.3.2. Hydrogen adsorption of 18	191
7.3.3. Nitrogen and argon adsorption of 18	193
7.3.4. Low-pressure CO ₂ adsorption of 18	197
7.3.5. High-pressure CO ₂ adsorption of 18	203
7.3.6. Discussion of structural effects on adsorption behavior	205
7.4. Conclusions	210
Chapter 1 References	212
Chapter 2 References	215
Chapter 3 References	218
Chapter 4 References	220
Chapter 5 References	222
Chapter 6 References	225
Chapter 7 References	227
Appendix	231
VITA	238

LIST OF TABLES

Chapter 1

Table 1.1 Energy densities of hydrogen and common fuel sources. Adapted from reference 4	26
--	----

Chapter 2

Table 2.1 Structures of L (carboxylate) ligands for 1 – 15	40
Table 2.2 Structures of L' (pyridyl) ligands for 1 – 15	41
Table 2.3 Summary of structural elements of 1 – 15 . All structures are of the general formula $Zn_2(L)_2(L') \cdot nDMF$	42
Table 2.4 Crystallographic data for 1 – 3	52
Table 2.5 Crystallographic data for 4 and 5	53
Table 2.6 Crystallographic data for 6 – 8	54
Table 2.7 Crystallographic data for 9 and 10	55
Table 2.8 Crystallographic data for 11 and 12	56
Table 2.9 Crystallographic data for 13 and 14	57

Chapter 4

Table 4.1 Summary of N_2 and H_2 low-pressure and temperature adsorption measurements of 4 and 4·M	103
Table 4.2 Quantification of residual solvent in 4·K materials by 1H NMR	112

Chapter 5

Table 5.1 Summary of N_2 and H_2 adsorption measurements for 9 and 9·M	125
Table 5.2 Summary of 1H NMR quantification of solvent in 9·M	133

	14
Table 5.3 Full t-plot analysis of 9 and 9·M materials	137

Chapter 6

Table 6.1. Summary of crystallographic data for 16 and 17	147
Table 6.2 Summary of N ₂ and H ₂ adsorption measurements for 17	162

Chapter 7

Table 7.1 Summary of crystallographic analysis of 18	184
--	-----

LIST OF FIGURES

Chapter 1

- Figure 1.1** MOF synthesis. Metal nodes (yellow circles) are mixed with organic ligands (red rods) under appropriate conditions to yield open framework structures30
- Figure 1.2** Illustration of two types of catentation possible in MOFs.
A) Interwoven frameworks, in which frameworks have many close contacts and pore volume is maximized. B) Interpenetrated frameworks, in which frameworks are maximally displaced and pore volume is significantly decreased from completely non-interpenetrated analogue31
- Figure 1.3** Impact of MOF pore size (gray slab) on H₂ (orange circle) interaction energy. A) Large pore scenario: only significant attractive H₂-MOF interaction energy when H₂ very closely approaches pore wall. B) Medium pore scenario: H₂ may interact with both pore walls, but considerable “wasted” pore volume where $u_{disp} \sim 0$. C) Small pore scenario: H₂ interacts with both pore walls, resulting in an additive effect in observed H₂-MOF interaction energy33

Chapter 2

- Figure 2.1** A) Crystal structures of **1** – **3**, only one network shown for clarity. The yellow polyhedra represent the zinc ions. Carbon: gray. Oxygen: red. Nitrogen: blue. Hydrogens omitted for clarity. B) Packing diagram for **1** – **3** down bipyr axis showing two-fold interpenetration61
- Figure 2.2** A) N₂ adsorption isotherm of **2**. Closed symbols, adsorption; open symbols, desorption. B) PXRD of **2** as synthesized, evacuated, and resolvated; demonstrating dynamic framework behavior62
- Figure 2.3** A) Crystal structures of **4** and **5**, only one network shown for clarity. B) Packing diagrams of **4** and **5** down dipyriddy axis, illustrating two-fold catentation64
- Figure 2.4** A) Color change of **4** (left) upon exposure to lithium naphthalenide (right). B) Color change of **2** (left) upon exposure to lithium naphthalenide (right)65

Figure 2.5	A) Crystal structure of 6 , one network (left) and packing diagram (right). B) 77K H ₂ uptake (left) and isosteric heat of adsorption (right) of 6 compared with 4	67
Figure 2.6	A) Crystal structure of 8 , one network and packing diagram. B) PXRD of 8 , reaction mixture and purified	69
Figure 2.7	A) Crystal structures of 9 and 10 , one network only. B) Packing diagram of 9 and 10 , illustrating three-fold interpenetration	71
Figure 2.8	A) Crystal structures of 11 and 12 , one network only. B) Packing diagram of 11 and 12 , illustrating two-fold interpenetration	74
Figure 2.9	A) N ₂ adsorption isotherms for 11 and 12 . B) 77K H ₂ isotherms (left) and H ₂ isosteric heat of adsorption (right) plots for 11 and 12	75
Figure 2.10	A) Crystal structures of 13 (left) and 14 (right). B) Packing diagram of 13 down b-axis (left) and 14 down a-axis (right), illustrating non-catenated frameworks	77
Figure 2.11	Packing diagrams of crystal structure for 15 (partially solved), illustrating non-catenated framework. Distances shown for Zn-Zn positions; distances in () are those for structure 6 . A) View down c axis, B) view down b axis	79
Figure 2.12	A) PXRD and TGA of as synthesized 15 . B) N ₂ adsorption isotherms under various activation conditions	80

Chapter 3

Figure 3.1	A) Crystal structure of 4 omitting interwoven second network. The yellow polyhedra represent the zinc ions. Carbon: gray. Oxygen: red. Nitrogen: blue. B) Packing diagram of 4 down diPyNI axis showing two-fold interpenetration	87
Figure 3.2	A) PXRD and B) TGA of 4 and oxidized 4Li⁺	89
Figure 3.3	A) N ₂ isotherms of 4 and 4Li⁺ . Closed symbols, adsorption; open symbols, desorption. B) N ₂ isotherm cycling of 4Li⁺	91
Figure 3.4	N ₂ isotherms of 4Li⁺ at 77K and 87K	92
Figure 3.5	A) H ₂ adsorption isotherms of 4 and 4Li⁺ at 77K. B) Isosteric H ₂ heat of adsorption of 4 and 4Li⁺	94

Chapter 4

Figure 4.1 77K H ₂ isotherms for 4 and 4·M . Closed symbols, adsorption; open symbols, desorption	104
Figure 4.2 Isosteric H ₂ heat of adsorption for 4 and 4·M	105
Figure 4.3 77K H ₂ isotherms for 4·K materials	106
Figure 4.4 N ₂ isotherms for 4 and 4·M . Closed symbols, adsorption; open symbols, desorption	110
Figure 4.5 H ₂ uptake at 1atm plotted against BET surface area. Data for 4 is omitted in linear fit	111
Figure 4.6 500 MHz ¹ H NMR of dissolved 4 in D ₂ SO ₄	112

Chapter 5

Figure 5.1 A) Single crystal structure of 9 . For clarity, disordered solvent molecules, hydrogens, and two levels of interpenetration are omitted. The yellow polyhedra represent the zinc ions; C, gray; N, blue; O, red. B) Packing diagram of 9	119
Figure 5.2 A) Color change of 9 upon exposure to lithium naphthalenide. B) PXRD of 9 and 9·M	124
Figure 5.3 A) Solid-state room temperature CW-EPR spectra of 9 (red) and 9·Li (black). Microwave power was 2 mW with a frequency modulation depth of 100 KHz. The small EPR signal present in the neutral sample 9 is attributed to light sensitivity of the material, as it has been demonstrated that the intensity of this signal increases upon photoirradiation (Figure 5.4B). Samples 9·Na and 9·K exhibited similar EPR signals. B) Solid-state room temperature CW-EPR spectra of 9 (red) and 9 after ~20 minutes of irradiation with a 100 W hand lamp (black). Microwave power was 2 mW with a frequency modulation depth of 100 KHz	126
Figure 5.4 77K H ₂ adsorption isotherms of 9 and 9·M . Open symbols, adsorption; closed symbols, desorption	129

Figure 5.5	Isosteric H ₂ heat of adsorption of 9•M . Detail of behavior at low loading is depicted in inset	130
Figure 5.6	N ₂ adsorption isotherms of 9 and 9•M	136
Figure 5.7	Correlation of H ₂ uptake at 1 atm and 77K with (A) BET surface area and (B) micropore volume derived from t-plot analysis	138

Chapter 6

Figure 6.1	A) Reaction scheme and crystal structure of 16 . Yellow polyhedra represent zinc ions; gray, carbon; blue, nitrogen; red, oxygen. B) Packing diagrams of 16	151
Figure 6.2	A) Proton-lithium exchange scheme. B) 400 MHz ¹ H NMR of DPG (bottom) and DPG-2Li ⁺ (top) in DMSO-d ₆ . Note hydroxyl proton peak at 5.7 ppm is not present in lithium alkoxide spectra	153
Figure 6.3	A) N ₂ adsorption isotherm of 16 , BET surface area 52 m ² /g. Closed symbols, adsorption; open symbols, desorption. B) 77K H ₂ isotherm of 16	155
Figure 6.4	A) Reaction scheme and crystal structure of 17 . Yellow polyhedra represent zinc ions; gray, carbon; blue, nitrogen; red, oxygen, hydrogens omitted for clarity B) Packing diagrams of 17	157
Figure 6.5	Bulk characterization of 17 by PXRD (A) and TGA (B)	158
Figure 6.6	N ₂ adsorption isotherm of 17 . Closed symbols, adsorption; open symbols, desorption	160
Figure 6.7	A) 77K H ₂ adsorption of 17 , and B) H ₂ isosteric heat of adsorption of 17	161
Figure 6.8	N ₂ adsorption isotherms of 17 and 17-Li materials. Closed symbols, adsorption; open symbols, desorption	166
Figure 6.9	77K H ₂ adsorption isotherms of 17 and 17-Li	167
Figure 6.10	H ₂ isosteric heat of adsorption of 17 and 17-Li materials	168
Figure 6.11	N ₂ adsorption isotherms of 17 and 17-Mg . Closed symbols, adsorption; open symbols, desorption	171

Figure 6.12	A) 77K H ₂ adsorption isotherms of 17 and 17-Mg . B) Isothermic H ₂ heat of adsorption plots for 17 and 17-Mg	172
Figure 6.13	N ₂ isotherms of Mg-ALD materials. Closed symbols, adsorption; open symbols, desorption	175
Figure 6.14	A) 77K H ₂ adsorption isotherms of Mg-ALD materials. B) H ₂ isothermic heat of adsorption of Mg-ALD materials	176

Chapter 7

Figure 7.1	A) Chemical structure of L1 and L2 , B) Crystal structure of 18 , one level of interpenetration is omitted to illustrate connectivity. Yellow polyhedra represent zinc ions; gray, carbon; blue, nitrogen; red, oxygen. Hydrogens omitted for clarity. C) Catenation of 18	188
Figure 7.2	Packing diagrams of 18 to illustrate interpenetration. Individual frameworks are different colors. A) Stick models down a, b, and c axes. B) Spacefilling models down a, b, and c axes	189
Figure 7.3	Characterization of bulk phase of 18 by (A) PXRD and (B) TGA	190
Figure 7.4	A) 77K H ₂ adsorption and B) isothermic heat of adsorption of 18	192
Figure 7.5	N ₂ adsorption isotherm of 18 . Closed symbols, adsorption; open symbols, desorption. Inset depicts adsorption/desorption on a log scale	195
Figure 7.6	Ar adsorption isotherm of 18 at 87K. Closed symbols, adsorption; open symbols, desorption. Inset depicts adsorption/desorption on a log scale	196
Figure 7.7	273K CO ₂ adsorption isotherm of 18 . Closed symbols, adsorption; open symbols, desorption. Lines connecting data points are intended to guide the eye	199
Figure 7.8	273K CO ₂ adsorption isotherms of 18 . A) Back-to-back adsorption/desorption isotherms. B) Increase of equilibration time to verify width of hysteresis	200
Figure 7.9	Low pressure CO ₂ isotherms of 18 at various temperatures. Lines connecting data points are intended to guide the eye	202

- Figure 7.10** CO₂ adsorption of **18** at various temperatures as a function of relative pressure. Closed symbols, adsorption; open symbols, desorption. Lines connecting data points are intended to guide the eye202
- Figure 7.11** High-pressure CO₂ adsorption of **18**. Closed symbols, adsorption; open symbols, desorption. Lines connecting data points are intended to guide the eye204
- Figure 7.12** 273K CO₂ adsorption of **18** and Langmuir fits to adsorption and desorption branches of isotherm. Langmuir fit to adsorption branch gives surface area of 335 m²/g; Langmuir fit to desorption branch gives surface area of 691 m²/g209

LIST OF SCHEMES

Chapter 3

- Scheme 3.1** Reduction of **4** in DMF to form **4**⁻Li⁺. N₂ adsorption measurements suggest a reversible structural change, represented speculatively here as framework displacement88

Chapter 5

- Scheme 5.1** Chemical reduction of MOF using metal naphthalenide (M(NAP)) in THF: A) addition of metal to naphthalene in THF, B) introduce M(NAP)-THF solution to solid MOF, C) isolate reduced MOF by filtration. M is Li, Na, or K123

Chapter 6

- Scheme 6.1** Proposed exchange scheme and structures of **17**-Li and **17**-Mg170

Chapter 7

- Scheme 7.1** Potential dynamic structural behavior of **18** upon framework synthesis, activation, and guest adsorption. A) Reversible framework collapse. B) Interpenetrated structure formed during synthesis; interwoven structure on removal of solvents to maximize framework-framework interactions; interpenetrated structure reformed on introduction of gaseous adsorbate. C) Ligand rotation upon removal of solvents to block pore access and further rotation on introduction of gaseous adsorbate206

1. Introduction to Hydrogen Storage and Metal-Organic Frameworks

1.1 Motivation

1.1.1 Energy concerns

The world's dwindling supply of fossil fuels has driven the pursuit of reliable and renewable energy sources. The world currently consumes approximately 13 TW of energy, an astounding 3.2 TW in the United States alone.¹ The industrial growth of developing areas, coupled with a rapidly expanding population, can only exponentially increase the demand for current sources of energy; recent estimates place the world's total demand in 2050 at 40 TW. This will drive costs ever higher and, perhaps more dangerously, raise geopolitical tensions over the supply of and access to fossil fuel resources. To address these concerns, scientists and engineers have turned to sustainable energy sources such as solar, wind, geothermal, biomass, and hydroelectric.² Significant progress has been made in each of these arenas, although in addition to stationary energy sources, much of the world economy requires also clean and portable fuels to power the transportation sector. The ultimate goal is to use any of the above renewable energy sources to produce a clean, portable fuel which can be stored easily, transported efficiently, and used on demand.

Perhaps more distressing than the potential depletion of fossil fuel resources is the alarming rate at which global temperatures are rising.³ Anthropogenic global temperature fluctuation may have catastrophic effects, some of which can already be observed: melting ice shelves and rising sea levels, extinction of large numbers of species, etc. This spike in global temperatures is largely attributed to the accumulation of CO₂ in the atmosphere, the largest byproduct of burning carbon-based fuel sources. Swift implementation of carbon-free fuel sources is necessary to mitigate these effects and stem devastating environmental consequences.

1.1.2 Hydrogen as an energy carrier

Molecular hydrogen, the simplest of all molecules, possesses a gravimetric energy density greater than that of any other known fuel, see Table 1.1.⁴ Moreover, burning H_2 in a fuel cell configuration in the presence of oxygen produces electricity, with water and heat as the only byproducts.⁵ These two factors render H_2 an extremely attractive potential fuel. It is stressed that hydrogen is not a primary energy *source*, but rather an energy *carrier*; hydrogen is produced to store energy, and released when it is needed.

Hydrogen is certainly not without its detractors. Admittedly, there are three lofty challenges to the fulfillment of a global hydrogen economy: 1) production, 2) transport, and 3) storage.⁶ While hydrogen is the most abundant atom on earth, appearing in water and hydrocarbons, the functional form of dihydrogen does not naturally occur in large quantities. Therefore, it cannot be “harvested” like solar or wind energy, extracted like petroleum resources or mined like coal reserves. About 95% of hydrogen produced today is from the steam reforming of methane.⁷ This process is relatively cheap and efficient, but produces CO_2 in its wake, which negates the use of H_2 as a “carbon-free” fuel source. Water electrolysis can produce H_2 and O_2 cleanly, especially if driven by renewable energy sources. However, current technologies rely on precious metal catalysts which are quite expensive and not particularly efficient.^{8,9} Transport is the second major challenge to the hydrogen economy. The current pipeline infrastructure of the United States is established to move large quantities of liquid fuels, such as gasoline, or more dense gases, such as methane.¹⁰ Methane pipelines can be and have been refurbished to transport H_2 , but this will require strict engineering controls and severe upgrades to the existing infrastructure. The third topic, hydrogen storage, will be covered in the next section. In the face of this “grand

challenge”, the promise of a clean and efficient energy carrier in hydrogen justifies further resources to overcome the current obstacles to lead to widespread realization.

Table 1.1 Energy densities of hydrogen and common fuel sources. Adapted from reference 4.

energy carrier	form	gravimetric energy density (kWh/kg)	volumetric energy density (kWh/l)
Hydrogen	gas (30 MPa)	33.3	0.75
	liquid (-253°C)	33.3	2.36
Natural gas	gas (30 MPa)	13.9	3.38
	liquid (-162°C)	13.9	5.8
Propane	liquid	12.9	7.5
Gasoline	liquid	12.7	8.76
Diesel	liquid	11.6	9.7
Methanol	liquid	5.6	4.42

1.2 Hydrogen storage

1.2.1 Liquid or compressed gas storage

The storage of hydrogen in a safe and efficient manner such that it could become as commonly used as gasoline is a daunting challenge. The elegant simplicity of H_2 , which endows it with an extraordinarily high energy density, is also its demise when one considers its storage. Hydrogen is the lightest liquid known (density 0.07 g/cm^3) with the lowest boiling point except helium (20K). Therefore, to maintain the liquid or compressed gas phase in a space not much larger than the typical automobile's gas tank, one needs to cool or compress it significantly, both very energy intensive processes. Another concern with H_2 storage as a liquid or compressed gas is boil-off, estimated in current systems at the rate of 0.06-0.4% daily.¹¹ Additionally, the tank materials necessary to maintain low temperature and/or high pressure increase storage cost, weight, and volume. Nevertheless, storage of hydrogen as a liquid or compressed gas is the current technology used in prototype H_2 fuel cell vehicles. In order to bring these vehicles to a wider market however, it is necessary to address many of these technological issues.

1.2.2 Chemical storage: H_2 absorption

Metal hydrides and chemical hydrides are materials under investigation for chemisorptive hydrogen storage. Metal hydrides such as $NaAlH_4$ or Li_2NH can reversibly desorb H_2 by rearrangement of the crystal lattice at relatively low temperatures and pressures. However, these materials often suffer from low gravimetric capacity. For example, the maximum materials-based storage (not yet the total system storage) for these two representative materials is 7.4 and 3.4 wt% respectively, well below the 2015 DOE targets for on-board H_2 storage. Additionally, though they can be regenerated reversibly on-board, the metal hydrides often entail slow H_2 uptake and release and can be prohibitively expensive.

Chemical hydrides such as NaBH_4 or MgH_2 can also store hydrogen within their crystal lattice. Unlike the metal hydrides which release H_2 only upon heat or pressure, these rely on a chemical reaction with another small molecule, generally water or ethanol, to produce H_2 . These materials generally have very high gravimetric capacity, $\sim 10\%$ for the examples mentioned above. However, the total system weight suffers due to the additional water or ethanol that must be carried on board, and the hydrolysis or alcoholysis byproducts cannot be regenerated on-board.

1.2.3 Physisorptive storage: H_2 adsorption

Carbon-based materials have also been identified as potential H_2 storage materials through a physisorptive mechanism. As opposed to the metal and chemical hydrides, hydrogen is stored molecularly, there is no energy penalty associated with making or breaking bonds or disrupting the crystal lattice. Some of the first materials identified as potential materials in which to store H_2 by a physisorptive mechanism are high-surface area activated carbons and carbon nanotubes (CNTs).¹² The enormous surface area of these compounds is exploited to provide many sites on which H_2 to adsorb. Since reports of astonishingly high H_2 gravimetric capacity in CNTs have been irreproducible,^{12,13} most studies now conclude that pristine CNTs cannot meet DOE targets. Ongoing research with these materials includes metal-doped CNTs.¹⁴

Clearly, the safe and efficient storage of molecular hydrogen will require a concerted effort in the discovery of new materials. That objective is the technological focus of this thesis research.

1.3 Metal-Organic Frameworks

1.3.1 Background

Metal-organic frameworks (MOFs) are a class of materials whose crystalline nature, permanent porosity, and wide degree of structural and chemical tunability has rendered them ideal compounds in which to study gas storage,¹⁵⁻¹⁹ molecular separations,²⁰⁻²² and highly size- and enantio-selective catalysis.²³⁻²⁵ MOFs are comprised of metal vertices held apart in space by organic struts, and the appropriate synthetic conditions will yield permanently porous open frameworks,^{26,27} Figure 1.1. By combining well-understood metal coordination chemistry with the vast diversity of accessible organic ligands, the sheer number of achievable MOF structures is limitless. Perhaps most interestingly, MOFs are suitable to isorecticular design, the design of many materials having the same overall topology^{28,29} (see Chapter 2 for examples from our own lab). MOFs can form either as single networks or in multiple levels of catenation. The catenated networks can grow as interwoven, where there are many close contacts between the frameworks and pore volume is maximized or interpenetrated, where the frameworks are maximally displaced and pore volume is minimized,¹⁵ Figure 1.2. This control over pore size and chemical functionality therein allows one to map out the structure-function landscape for a given application.

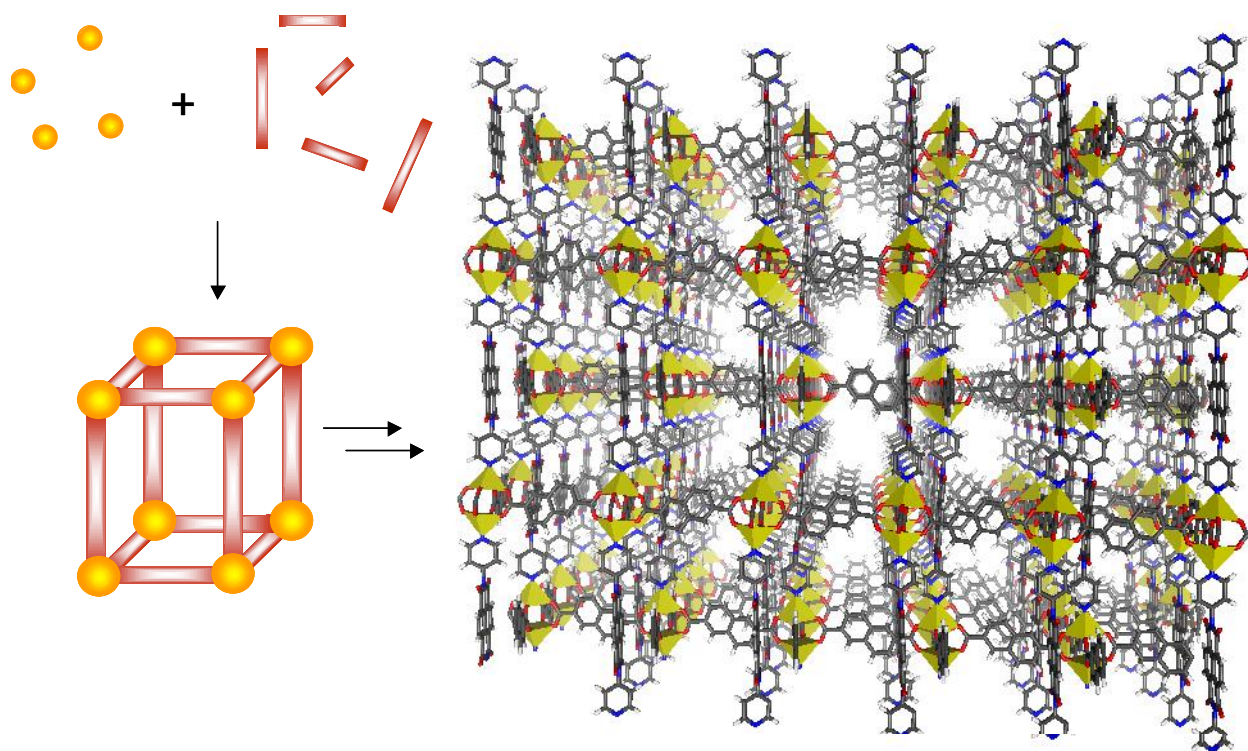


Figure 1.1 MOF synthesis. Metal nodes (yellow circles) are mixed with organic ligands (red rods) under appropriate conditions to yield open framework structures.

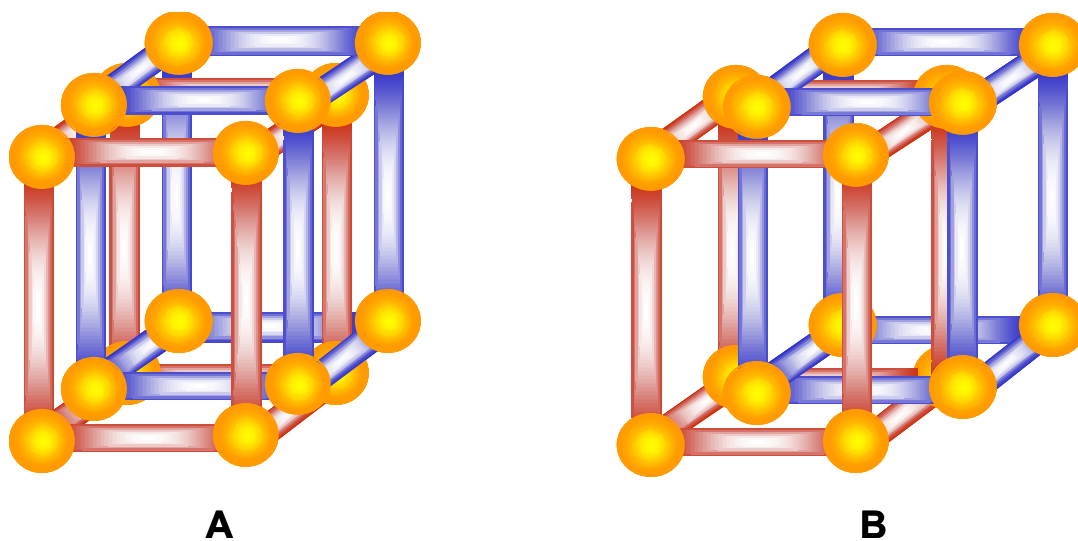


Figure 1.2 Illustration of two types of catenation possible in MOFs. A) Interwoven frameworks, in which frameworks have many close contacts and pore volume is maximized. B) Interpenetrated frameworks, in which frameworks are maximally displaced and pore volume is significantly decreased from completely non-interpenetrated analogue.

1.3.2 Strategies for H₂ storage in MOFs

The quest for viable H₂ storage in MOFs has recently reached a fever pitch, with two central strategies emerging to enhance uptake: 1) the optimization of pore size and geometry to effect the high-density H₂ packing, and 2) the creation of exceptionally strong H₂ binding sites within the framework.

The immense surface areas, huge pore volumes, and extra-low densities achievable in MOF materials immediately distinguish them as prospective candidates for gravimetric H₂ storage applications. Hydrogen is a particularly difficult adsorbate to work with; with only two electrons and no dipole moment, the only real interactions we can attempt to effect are London dispersion forces between the pore wall and H₂. The dispersion forces between two atoms or molecules can be described by the following equation:

$$u_{disp}(r) = -\frac{3}{2} \left(\frac{I_1 I_2}{I_1 + I_2} \right) \frac{\alpha_1 \alpha_2}{(4\pi\epsilon_0)^2} \frac{1}{r^6} \quad (1.1)$$

where I is the ionization energy of the atom or molecule (J), α is the polarizability (C·m²·V⁻¹), ϵ_0 is the permittivity of vacuum (8.85419 × 10⁻¹² C²·N⁻¹·m⁻²) and r is the distance between the two atoms or molecules, in this case H₂ and the pore wall. Note that the interaction energy is proportional to the product of the polarizabilities, and this is often the dominant contribution to the dispersion forces. Not only are these interactions relatively weak, but also decay as 1/ r^6 , so that any incoming H₂ guest molecules must be very close to the pore wall to effectively “feel” the MOF. Therefore, particularly at low pressures, there is no incentive to create huge pores in which H₂ is unlikely to reach near the pore wall. Through sensible choice of metal node and ligand length and geometry, an ideal pore size for the adsorption of H₂ can be achieved, Figure 1.3. The manipulation of pore width can enhance the coverage and strength of these forces and provide an ideal environment in which to adsorb H₂.

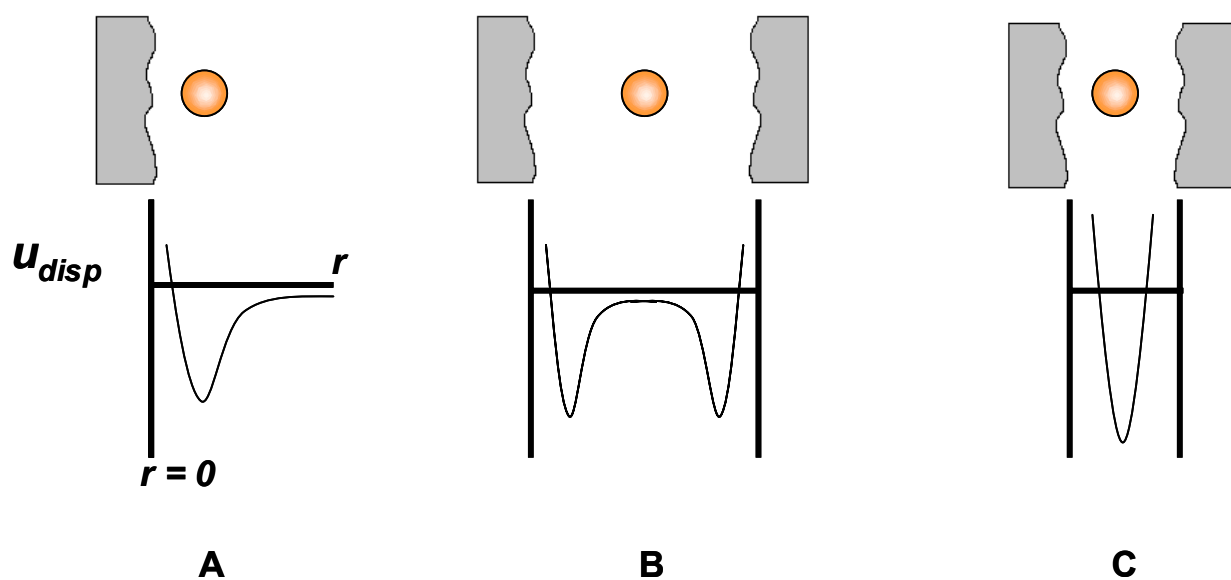


Figure 1.3 Impact of MOF pore size (gray slab) on H₂ (orange circle) interaction energy. A) Large pore scenario: only significant attractive H₂-MOF interaction energy when H₂ very closely approaches pore wall. B) Medium pore scenario: H₂ may interact with both pore walls, but considerable “wasted” pore volume where $u_{disp} \sim 0$. C) Small pore scenario: H₂ interacts with both pore walls, resulting in an additive effect in observed H₂-MOF interaction energy.

The impact of MOF structural properties on H₂ uptake has been studied both computationally and experimentally. In the IRMOF series, H₂ uptake was examined in three different pressure regimes.³⁰ Interestingly, at low pressure, the heat of adsorption, or H₂-framework interactions, played the largest role in uptake, while at high pressure, the accessible pore volume was the strongest influence on total uptake. These simulations have been confirmed experimentally in a Cu(II) paddlewheel-carboxylate isostructural MOF series.³¹ The structure with the smallest pores achieved the highest uptake at 77K and 1 bar, but was surpassed by the largest structure at 77K and 20 bar. Similar relations have been reported between uptake and pressure range when comparing catenated and non-catenated structures, both experimentally³² and computationally.³³

In addition to structural parameters which influence H₂ uptake, the chemical environment of the pore can be modulated to present highly attractive sites for specific H₂ sorption. This has been most frequently attempted by creating unsaturated metal centers (UMCs) via the removal of coordinated solvent molecules at the metal nodes.¹⁸ Indeed, neutron diffraction measurements have identified these UMCs as preferred binding sites within MOF materials.^{34,35} These UMC-H₂ interactions have been suggested to be Kubas-like interactions, in which H₂ binds side-on to the UMC.³⁶

1.4 Thesis direction and introduction

The aim of this thesis research is to design and synthesize new MOFs for H₂ storage applications. However, the intended contribution to this burgeoning area of research is not only to produce new and novel structures that could be used in H₂ storage applications, but the introduction and development of a technique to enhance H₂ uptake and binding in porous materials more generally. The only significant H₂-solid interactions stem from London

dispersion forces, see Equation 1.1. Increasing the polarizability, α , of the framework should enhance these interactions and thereby enhance total H₂ uptake. Given a particular framework geometry, (including the metal node), the polarizability of the framework can be regulated by 1) changing the organic ligand to another containing a highly polarizable functionality, or 2) chemically reducing each organic ligand in a post-synthetic manner which will increase the polarizability of the entire solid framework. This second approach will allow us to synthesize new structures and characterize them fully by X-ray crystallography and adsorption techniques, and then incrementally modulate the solid's polarizability via framework reduction. Furthermore, chemical reduction of the frameworks necessitates a counter-ion to balance charge; here we will use small alkali metal and alkaline earth cations. Several computational studies examining alkali-metal and transition metal doping of CNTs and C₆₀ indicate that these doped materials bind many more H₂ molecules than the pristine samples.^{37,38} More recently, computational studies suggest that lithium-doped MOFs also display stronger binding and higher H₂ uptake than their neutral counterparts.^{39,40}

High H₂ uptake and H₂-framework binding will be obtained not only by targeting the structural features of MOFs, but also by tailoring their electronic properties. The chapters that follow outline incremental steps towards the complete understanding of how the framework reduction and cation doping of MOFs impacts their H₂ sorption properties.

Chapter 2 describes the development of a library of fifteen new mixed-ligand MOFs based on Zn(II)-paddlewheel geometry. This framework motif has been particularly advantageous in the growth of new structures which can be reduced in the solid state and also withstand complete solvent evacuation.

Chapter 3 introduces the first experimental demonstration of a MOF reduced with Li-metal that enhances H₂ uptake. The heat of adsorption is also enhanced, but not as strongly to be from direct H₂-Li⁺ interactions. Nitrogen adsorption in the reduced material suggests structural changes, perhaps induced by doping, which may be the chief contribution to H₂ uptake enhancement.

Chapter 4 expands upon the work in Chapter 3, now using not only Li⁺, but also Na⁺ and K⁺ to framework reduce the same MOF structure. H₂ uptake is enhanced for all materials, but only at very low doping levels. From these studies of this two-fold interpenetrated framework we conclude that structural changes are the largest factor to H₂ uptake enhancement.

Chapter 5 provides another example of a reduced interpenetrated MOF that demonstrates H₂ uptake enhancement. This provides a generalization of the method of framework reduction and doping. And for this structure as well, variation in the structure upon doping is proposed to have the greatest impact on H₂ uptake.

Chapter 6 introduces a different method of doping MOFs with various cations: the formation of metal-alkoxide MOFs from hydroxyl groups on the struts. Quantitative alkoxide formation is achieved in two structures containing hydroxyl groups. Little to no structural changes are observed upon alkoxide formation, and porosity is preserved.

Chapter 7 examines an interpenetrated Zn(II)-paddlewheel with that displays unique structural changes upon activation and adsorption. Unique gated adsorption is observed in the N₂ and Ar isotherms and novel hysteresis is observed in the CO₂ isotherms. The results presented here clearly demonstrate structural flexibility within a material similar to those previously studied for H₂ storage and binding.

**Chapter 2. Microporous Pillared Paddlewheel Frameworks Based on Mixed Ligand
Coordination of Zinc Ions**

2. Chapter Overview

As discussed in Chapter 1, the virtually limitless structural diversity of MOFs renders them attractive potential materials to address several technological applications. Practically though, it is oftentimes difficult to reliably obtain a desired framework structure and functionality that can also withstand complete pore evacuation. Additionally, as applications become more demanding towards materials specificity, a premium will be placed on the ability to finely tailor chemical functionality in addition to pore geometry, even perhaps anisotropy. In this chapter I will describe the development of a new library of fifteen isostructural MOFs based on mixed-ligand coordination to zinc paddlewheel clusters. These structures are unique in that they contain more than one type of organic ligand whereas the majority of MOFs only contain one type of metal cluster and one type of ligand. This newfound ability to incorporate two types of ligand not only allows one to create a wide degree of structural diversity through the series, but present an opportunity to straightforwardly modulate functional diversity as well. The impetus of my efforts in developing this library of structures is to introduce redox-active ligands into the frameworks, allowing for the possibility of post-synthetic framework reduction and cation doping to enhance H₂ binding and uptake within these materials. Here I will demonstrate their synthesis and structural characterization by single crystal X-ray diffraction, PXRD, TGA, and adsorption measurements. Subsequent chapters will be devoted to framework reduction and H₂ sorption capabilities.

2.1 Introduction

Much of the current interest in the rapidly growing field of metal-organic-framework (MOF) materials derives from the potential of microporous crystalline versions of these materials to

provide interesting solutions to difficult problems in gas storage,¹⁻⁶ sensing,⁷ separations,⁸ and catalysis.^{9,10} To engender permanent microporosity, synthesis schemes must avoid both channel clogging (e.g., due to excessive framework interpenetration or unfavorable positioning of counter ions) and channel collapse (e.g., upon solvent removal). In many cases metal dimer or cluster/carboxylate linkages have proven sufficiently strong to stabilize networks against collapse,¹¹⁻¹³ whereas metal/pyridine linkages, although widely employed, generally have not stabilized open frameworks against channel collapse. A further drawback of pyridine-only frameworks is that ions required for charge compensation may block any channels obtained. We reasoned that both problems might be overcome by combining pyridine coordination with carboxylate coordination in mixed-ligand framework compounds. We further reasoned that mixed coordination could facilitate the incorporation of functionality. Of particular interest to us are redox reactivity and visible-region light collection and re-emission. Additionally, mixed-ligand compounds might be expected to display useful anisotropic optical, guest-transport, and/or other properties.

Here we report the synthesis and characterization of fifteen examples of mixed-ligand MOF materials. These new compounds make use of robust carboxylate paddlewheel type coordination^{14,15} of Zn(II) pairs to define perforated 2D sheets that are pillared with more delicate pyridine-Zn linkages to yield open mixed-ligand frameworks. The compounds can be formulated as Zn_2L_2L' -solvent, where L and L' are denoted in Tables 2.1 – 2.3 for structures **1-15**.

Table 2.1 Structures of L (carboxylate) ligands for **1 – 15**

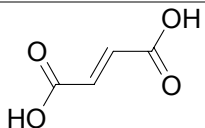
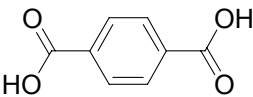
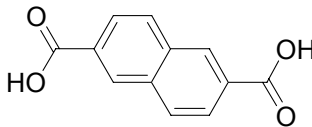
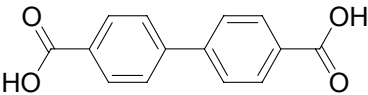
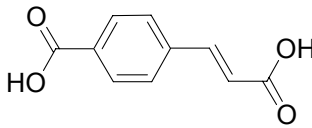
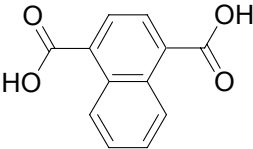
abbreviation	chemical name	structure
fa	fumaric acid	
BDC	1,4-benzenedicarboxylic acid	
NDC	2,6-naphthalenedicarboxylic acid	
bpdc	4,4'-biphenyldicarboxylic acid	
cca	4-carboxycinnamic acid	
1,4-NDC	1,4-naphthalenedicarboxylic acid	

Table 2.2 Structures of L' (pyridyl) ligands for **1 – 15**

abbreviation	chemical name	structure
bipy	4,4'-dipyridyl	
diPyNI	<i>N,N'</i> -di(4-pyridyl)-1,4,5,8-naphthalenetetracarboxydiimide	
diQuNI	<i>N,N'</i> -di-(5-aminoquinoline)-1,4,5,8-naphthalenetetracarboxydiimide	
diPyTz	Di-3,6-(4-pyridyl)-1,2,4,5-tetrazine	
diPyPI-Cl ₄	<i>N,N'</i> -di(4-pyridyl)-1,6,7,12-tetrachloro-3,4,9,10-perylenetetracarboxylic diimide	
diPyPI-Br ₂	<i>N,N'</i> -di(4-pyridyl)-1,7-dibromo-3,4,9,10-perylenetetracarboxylic diimide	
m-diPyNI	<i>N,N'</i> -di(3-pyridyl)-1,4,5,8-naphthalenetetracarboxydiimide	
m-diPyTz	Di-3,6-(3-pyridyl)-1,2,4,5-tetrazine	

Table 2.3 Summary of structural elements of **1** – **15**. All structures are of the general formula $\text{Zn}_2(\text{L})_2(\text{L}')\cdot n\text{DMF}$.

structure	L	L'
1	fa	bipy
2	BDC	bipy
3	NDC	bipy
4	NDC	diPyNI
5	bpdc	diPyNI
6	BDC	diPyNI
7	cca	diPyNI
8	NDC	diQuNI
9	NDC	diPyTz
10	cca	diPyTz
11	NDC	diPyPI-Cl ₄
12	NDC	diPyPI-Br ₂
13	NDC	m-diPyNI
14	NDC	m-diPyTz
15	1,4-NDC	diPyNI

2.2 Experimental

2.2.1 Materials and methods

Commercial reagents were purchased from Sigma Aldrich unless otherwise noted. ^1H NMR were taken on either a Mercury 400 or an Inova 500 spectrometer. All spectra were referenced to the residual solvent peak. Low-resolution laser desorption mass spectra were obtained with a PE Voyager DE-Pro MALDI-TOF mass spectrometer. Elemental analyses were performed by Atlantic Microlabs, Inc. (Norcross, GA). Powder X-ray diffraction (PXRD) patterns were recorded with a Rigaku XDS 2000 diffractometer using nickel-filtered Cu K α radiation ($\lambda = 1.5418 \text{ \AA}$) over a range of $5^\circ < 2\theta < 40^\circ$ in 0.1° steps with a 1-s counting time per step. Powder samples were placed in the diffractometer mounted on a stainless steel holder with double-sided tape. Thermogravimetric analyses (TGA) were performed on a Mettler-Toledo TGA/SDTA851e. Samples (3-5 mg) in alumina pans were heated from 25°C to 700°C at $10^\circ\text{C}/\text{minute}$ under N_2 .

2.2.2 Ligand synthesis

The following ligands are commercially available and were obtained from Sigma-Aldrich: fumaric acid, 1,4-benzenedicarboxylic acid (terephthalic acid), 2,6-naphthalenedicarboxylic acid, 4,4'-biphenyldicarboxylic acid, and 1,4-naphthalenedicarboxylic acid. 4-carboxycinnamic acid was obtained from Lancaster Synthesis. The syntheses of diPyNI, diPyTz,¹⁶ and m-diPyTz¹⁷ have been reported previously.

Synthesis of diQuNI: 1,4,5,8-naphthalenetetracarboxydianhydride (400 mg, 1.49 mmol), 5-aminoquinoline (472 mg, 3.27 mmol), and 40 ml pyridine were combined in a 100 ml 2-neck round bottom flask and heated to reflux overnight. After cooling, the solid was isolated by filtration and washed with acetone and hexanes and allowed to dry in air. Isolated yield: 279

mg, 36%. ^1H NMR (TFA-d): δ 9.16 (d, J = 5.0 Hz, 2H), 9.04 (d, J = 9.0 Hz, 2H), 8.98 (s, 4H), 8.49 (d, J = 9.0 Hz, 2H), 8.35 (t, J = 9.0 Hz, 2H), 8.12 (d, J = 8.0 Hz, 2H), 8.07 (t, J = 8.0 Hz, 2H). MALDI-TOF MS: obs 521.98; calcd $[\text{M}+\text{H}]^+$ 521.49. Anal. calcd. for diQuNI, $\text{C}_{32}\text{H}_{16}\text{N}_4\text{O}_4$: C, 73.84; H, 3.10; N, 10.76. Found: C, 72.98; H, 3.34; N, 11.10.

Synthesis of diPyPI-Cl₄: 1,6,7,12-Tetrachloro-3,4:9,10-perylenetetracarboxylic dianhydride (SYNTHON Chemicals, 500 mg, 0.94 mmol), 4-aminopyridine (267 mg, 2.8 mmol), and 50 ml pyridine were combined in a 100 ml 2-neck round bottom flask and heated to reflux overnight. After cooling, the solid was isolated by filtration and washed with water, acetone, and hexanes and allowed to dry in air. Isolated yield: 462 mg, 72%. 500 MHz ^1H NMR (TFA-d): δ 9.05 (d, J = 6.0 Hz, 4H), 8.80 (s, 4H), 8.30 (d, J = 6.0 Hz, 4H). MALDI-TOF MS: obs 680.6; calcd $[\text{M}-\text{H}]^-$ 681.3. Anal. calcd. for diPyPI-Cl₄, $\text{C}_{34}\text{H}_{12}\text{Cl}_4\text{N}_4\text{O}_4$: C, 59.85; H, 1.77; N, 8.21. Found: C, 59.76; H, 1.85; N, 8.34.

Synthesis of diPyPI-Br₂: The synthesis is completed in two steps: 1) condensation of the unmodified perylene dianhydride with 4-aminopyridine, and 2) bromination of the perylene bay region.

3,4:9,10-perylenetetracarboxylic dianhydride (110 mg, 0.30 mmol), 4-aminopyridine (85 mg, 0.90 mmol) and Zn(OAc) \cdot 2H₂O (330 mg, 1.50 mmol) were added to 6 ml quinoline in a 100 ml 2-neck round bottom flask and heated to reflux overnight. After cooling, 50 ml 2M HCl was added dropwise to the flask and stirred one hour. The resultant solid was isolated by filtration and washed with H₂O, 2M HCl, methanol, and acetone, dried in air and then placed in a 100°C vacuum oven overnight to dry completely. Isolated yield: 150 mg, 92%. MALDI-TOF MS: obs 545.9; calcd $[\text{M}+\text{H}]^+$ 545.5. This product (diPyPI) was used without further purification.

The bromination follows a slightly modified literature procedure:¹⁸ diPyPI (1.0 g, 1.80 mmol) was added to 50 ml concentrated H₂SO₄ with stirring in a round bottom flask and heated to 55°C overnight. Iodine (24 mg, 0.09 mmol) was then added and stirred an additional 4 hours. Bromine (1.0 ml, 19.5 mmol) was added dropwise to the reaction flask over 20 minutes and stirred for 3 hours at 85° C. Excess bromine was then displaced by bubbling nitrogen through the reaction mixture. Water (100 ml) was added dropwise to the cooled mixture and the precipitate filtered off. The solid product was washed with copious amounts of water, acetone and hexanes to dry, and then dried under vacuum at 100°C overnight to afford diPyPI-Br₂ (1.20 g, 95%). 500MHz ¹H NMR (TFA-d): δ 9.77 (d, J = 8.0 Hz, 2H), 9.13 (d, J = 5.0 Hz, 4H), 9.10 (s, 2H), 8.88 (d, J = 8.0 Hz, 2H), 8.37 (d, J = 5.0 Hz, 4H). MALDI-TOF MS: obs 703.7; calcd [M+H]⁺ 703.3.

Synthesis of m-diPyNI: 1,4,5,8-naphthalenetetracarboxylic dianhydride (1.00 g, 3.7 mmol), 3-aminopyridine (787 mg, 8.4 mmol), and 50 ml DMF were combined in a 100 ml 2-neck round bottom flask and heated to reflux overnight. After cooling, the solid was isolated by filtration and washed with water, acetone and hexanes and allowed to dry in air. Isolated yield: 1.15 g, 73%. 500MHz ¹H NMR (TFA-d): δ 9.16 (s, 2H), 8.94 (d, J = 6.0 Hz, 2H), 8.92 (s, 4H), 8.76 (d, J = 8.5 Hz, 2H), 8.27 (m, 2H). MALDI-TOF MS: obs 421.6; calcd [M+H]⁺ 421.4. Anal. calcd. for m-diPyNI, C₂₄H₁₂N₄O₄: C, 68.57; H, 2.88; N, 13.33. Found: C, 68.55; H, 2.87; N, 13.34.

2.2.3 MOF synthesis

Structures **1** – **3** were designed, synthesized, and solved by Dr. Bao-Qing Ma.

Synthesis of **1**: Zn(NO₃)₂·6H₂O (30 mg, 0.1mmol), H₂fa (11.8 mg, 0.1 mmol) and bipy (8 mg, 0.05mmol) were mixed in a solution containing 10 mL DMF, 1 mL ethanol and 1mL water

in a small vial, which was capped and heated to 60 °C in an oil bath for 2 days, and then cooled to room temperature. X-ray quality single crystals of **1** were formed and collected by filtration and washed with DMF several times. Anal. calcd. for **1**, C₁₈H₁₉Zn₂N₂O_{8.5}, C 41.25, H 2.50, N 5.35; found: C 41.02, H 2.55, N 5.35.

Synthesis of **2**: Zn(NO₃)₂·6H₂O (30 mg, 0.1mmol), H₂BDC (16.6mg, 0.1 mmol) and bipy (8 mg, 0.05mmol) were mixed with 10 mL DMF in a small vial, which was capped and heated to 80 °C in an oil bath for 2 days, and then cooled to room-temperature. X-ray quality single crystals of **2** were formed and collected by filtration and washed with DMF several times. Anal. calcd. for **2** C₂₆H₁₈Zn₂N₂O₉, C 50.30, H 2.90, N 4.52; found: C 49.03, H 2.40, N 4.22. A large-scale preparation method has been developed for bulk characterization. A sample preparation follows: Zn(NO₃)₂·6H₂O (500 mg, 1.68 mmol), H₂BDC (275 mg, 1.66 mmol), and bipy (187 mg, 1.20 mmol) were added to a 250 ml round bottom flask containing 125 ml DMF. The contents were then sonicated until dissolved and the flask was added to an oil bath and heated to 130°C with stirring for 5 hours. The contents were allowed to cool and the white microcrystalline solid (**2**) was isolated by filtration, washed with DMF, and allowed to dry in air (567 mg, 83% yield based on Zn).

Synthesis of **3**: Zn(NO₃)₂·6H₂O (30 mg, 0.1mmol), H₂NDC (21.6 mg, 0.1 mmol) and bipy (8 mg, 0.05mmol) were mixed with 10 mL DMF solution in a small vial, which was capped and heated to 80°C in an oil bath for 2 days, and then cooled to room temperature. X-ray quality single crystals of **3** were formed and collected by filtration and washed with DMF several times. Anal. calcd. for **3** C₃₀H₂₂Zn₂N₂O₉, C 52.63, H 3.22, N 4.09; found: C 52.71, H 2.96, N 4.05.

Synthesis of **4**: Zn(NO₃)₂·6H₂O (30 mg, 0.1mmol), H₂NDC (11 mg, 0.05 mmol) and diPyNI (11 mg, 0.025mmol) were mixed with 10 mL DMF in a small vial, which was capped

and heated to 80°C in an oil bath for 2 days, and then cooled to room-temperature. Bright yellow X-ray quality single crystals of **4** were formed and collected by filtration and washed with DMF several times. A large-scale preparation method has also been developed for bulk characterization. A sample preparation follows: $\text{Zn}_2(\text{NO}_3)_2 \cdot 6\text{H}_2\text{O}$ (600mg, 2.0 mmol), H_2NDC (87mg, 0.4 mmol), diPyNI (170mg, 0.4 mmol), and 200 ml DMF were added to a 500 ml flat-bottom flask. The flask was sonicated until all contents were dissolved and then placed in an 80°C oil bath for two days. The bright yellow crystalline product was removed from the flask, isolated via filtration, washed with DMF, and allowed to dry in air. $\text{Zn}_2(\text{NDC})_2(\text{diPyNI})$ (**4**) recovered: 239mg, 18% yield based on zinc. Anal. calcd. for $\text{4} \cdot 2\text{H}_2\text{O}$, $\text{C}_{48}\text{H}_{28}\text{N}_4\text{O}_{14}\text{Zn}_2$: C, 56.77; H, 2.78; N, 5.52. Found: C, 56.17; H, 2.81; N, 5.58.

Synthesis of **5**: $\text{Zn}(\text{NO}_3)_2 \cdot 6\text{H}_2\text{O}$ (30 mg, 0.1mmol), H_2BPDC (24 mg, 0.1 mmol) and diPyNI (21 mg, 0.05mmol) were mixed with 10 mL DMF in a small vial, which was capped and heated to 80°C in an oil bath for 2 days, and then cooled to room-temperature. Yellow X-ray quality single crystals of **5** were formed and collected by filtration and washed with DMF several times.

Synthesis of **6**: $\text{Zn}(\text{NO}_3)_2 \cdot 6\text{H}_2\text{O}$ (8 mg, 0.03 mmol), H_2BDC (4 mg, 0.02 mmol) and diPyNI (3 mg, 0.007 mmol) were dissolved in 2.5 ml DMF in a small vial, which was capped and placed in an 80°C oil bath for two days. The warm mother liquor was decanted and yellow X-ray quality single crystals were washed with and stored under fresh DMF. A large-scale preparation was developed for bulk characterization. A sample preparation follows: $\text{Zn}(\text{NO}_3)_2 \cdot 6\text{H}_2\text{O}$ (152 mg, 0.51 mmol), H_2BDC (85 mg, 0.51 mmol), diPyNI (53 mg, 0.13 mmol) and 50 ml DMF were added to a 125 ml erlenmeyer flask and sonicated. The solution was divided equally between five 8-dram screw cap vials. The vials were capped and placed in

a 80°C oil bath for 2 days. The vials were removed from the oil bath and the contents were combined and filtered while warm. The yellow crystalline solid was washed with DMF and allowed to dry in air: 119 mg, 53% yield based on Zn.

Synthesis of **7**: $\text{Zn}(\text{NO}_3)_2 \cdot 6\text{H}_2\text{O}$ (15 mg, 0.05 mmol), H_2cca (5 mg, 0.03 mmol), and diPyNI (5 mg, 0.01 mmol) were added to a small vial in 5 ml DMF. The contents were sonicated to dissolve and heated to 80°C for 72 hours, upon which time yellow crystals of **7** were formed. The warm mother liquor was decanted and the crystals were washed with and stored under fresh DMF.

Synthesis of **8**: X-ray quality single crystals of were obtained upon heating $\text{Zn}(\text{NO}_3)_2 \cdot 6\text{H}_2\text{O}$ (15 mg, 0.05 mmol), H_2NDC (10 mg, 0.05 mmol) and diQuNI (6 mg, 0.01 mmol) in 5 ml DEF at 80°C for 48 hours. Bright yellow crystals were picked from the crude mixture with white crystalline powder for single crystal analysis. After purification by density separation techniques,¹⁹ isolated yield 8 mg (30% yield based on Zn). Anal. calcd. for **8**·**5H₂O**, $\text{C}_{56}\text{H}_{33}\text{N}_4\text{O}_{14.5}\text{Zn}_2$: C, 59.80; H, 2.96; N, 4.98. Found: C, 59.41; H, 2.88; N, 5.28.

Synthesis of **9**: X-ray quality single crystals were obtained by heating $\text{Zn}(\text{NO}_3)_2 \cdot 6\text{H}_2\text{O}$ (14 mg, 0.05 mmol), H_2NDC (10 mg, 0.05 mmol) and diPyTz (6 mg, 0.025 mmol) in 5 ml DMF to 100°C in a sealed vial for two days. After two days, the mother liquor was decanted from the crystals, and the remaining solid was washed with and stored under fresh DMF. Large scale preparation of **9** is carried out in an analogous fashion: $\text{Zn}(\text{NO}_3)_2 \cdot 6\text{H}_2\text{O}$ (375 mg, 1.26 mmol), H_2NDC , (273 mg, 1.26 mmol), diPyTz (149 mg, 0.63 mmol) and 125 ml DMF are added together in a 250ml flat-bottom flask, sonicated, and heated to 100°C for two days which yields a bright pink crystalline solid. This solid is isolated via filtration, washed with DMF, and dried

in air. Anal. calcd. for evacuated **9**·1H₂O, C₃₆H₂₀N₆O₉Zn₂: C, 53.16; H, 2.73; N, 10.33. Found: C, 53.05; H, 2.61; N, 10.27.

Synthesis of **10**: Zn(NO₃)₂·6H₂O (15 mg, 0.05 mmol), H₂cca (10 mg, 0.05 mmol) and diPyTz (6 mg, 0.03 mmol) were added to a small vial with 5 ml DMF and heated to 80°C for 72 hours upon which time bright pink crystals of **10** were formed. The warm mother liquor was decanted and the crystals were washed with and stored under fresh DMF.

Synthesis of **11**: X-ray quality single crystals of **11** were obtained upon heating Zn(NO₃)₂·6H₂O (6 mg, 0.02 mmol), H₂NDC (4 mg, 0.02 mmol) and diPyPI-Cl₄ (3 mg, 0.004 mmol) in 5 ml DMF at 100°C for 72 hours upon which dark red crystals were obtained. Large scale preparation for bulk characterization follows a similar procedure: Zn(NO₃)₂·6H₂O (200 mg, 0.67 mmol), H₂NDC (146 mg, 0.67 mmol) and diPyPI-Cl₄ (114 mg, 0.17 mmol), 200 ml DMF were added to a 500 ml flat bottom flask, sonicated to create a fine suspension and placed in an 100°C oil bath for 48 hours. The solid material did not dissolve at room temperature, but upon heating dissolved completely. Dark red crystalline material formed within two days. The crystalline solid was removed from the flask, isolated by filtration, washed with DMF, and allowed to dry in air: 309 mg, 59% yield based on Zn.

Synthesis of **12**: X-ray quality single crystals of **12** were obtained upon heating Zn(NO₃)₂·6H₂O (5 mg, 0.02 mmol), H₂NDC (4 mg, 0.02 mmol) and diPyPI-Br₂ (6 mg, 0.01 mmol) in 10 ml DMF at 80°C for 72 hours upon which dark red crystals were obtained. Large scale preparation for bulk characterization follows a similar procedure: Zn(NO₃)₂·6H₂O (150 mg, 0.50 mmol), H₂NDC (109 mg, 0.50 mmol) and diPyPI-Br₂ (87 mg, 0.12 mmol), 100 ml DMF were added to a 250 ml flat bottom flask, sonicated to dissolve and placed in an 80°C oil bath for 48 hours. Dark red crystalline material formed within two days. The crystalline solid

was removed from the flask, isolated by filtration, washed with DMF, and allowed to dry in air:

94 mg, 24% yield based on Zn. Anal. calcd. for **12**·2H₂O, C₅₈H₃₀Br₂N₄O₁₄Zn₂: C, 53.69; H, 2.33; N, 4.32. Found: C, 53.40; H, 2.47; N, 4.47.

Synthesis of **13**: X-ray quality single crystals of **13** were obtained upon heating Zn(NO₃)₂·6H₂O (16 mg, 0.05 mmol), H₂NDC (11 mg, 0.05 mmol) and m-diPyNI (44 mg, 0.10 mmol) in 5 ml DMF at 100°C for 72 hours upon which yellow-orange crystals were obtained. The warm mother liquor was decanted and the crystals were washed with and stored under fresh DMF.

Synthesis of **14**: X-ray quality single crystals of **14** were obtained upon heating Zn(NO₃)₂·6H₂O (28 mg, 0.10 mmol), H₂NDC (20 mg, 0.10 mmol) and m-diPyTz (6 mg, 0.025 mmol) in 5 ml DMF at 80°C for 48 hours upon which pink crystals were obtained. The mother liquor was decanted and the crystals were washed with fresh DMF several times.

Synthesis of **15**: X-ray quality single crystals of **15** were obtained upon heating Zn(NO₃)₂·6H₂O (15 mg, 0.05 mmol), H₂1,4-NDC (5 mg, 0.02 mmol) and diPyNI (5 mg, 0.01 mmol) in 5 ml DMF at 80°C for 48 hours upon which amber crystals were formed. The warm mother liquor was decanted and the crystals were washed with and stored under fresh DMF. A large scale preparation was developed for bulk characterization, a sample preparation follows: Zn(NO₃)₂·6H₂O (300 mg, 1.01 mmol), H₂1,4-NDC (218 mg, 1.01 mmol), diPyNI (212 mg, 0.50 mmol) and 100 ml DMF were added to a 250 ml erlenmeyer flask. The contents were sonicated to dissolve and the yellow solution was divided equally between 10 8-dram screw cap vials and heated to 80°C for 48 hours. The contents of all the vials were combined, filtered, washed with DMF and allowed to dry in air: **15** recovered: 107 mg, 26% yield based on zinc.

2.2.4 Crystal structure determination

Single crystals of **1** – **5**, **7**, and **9** - **14** were mounted on a BRUKER SMART CCD 1000 diffractometer equipped with a graphite-monochromated MoK α ($\lambda = 0.71073$ Å) radiation source in a cold nitrogen stream. Single crystals of **6**, **8** and **15** were mounted on a BRUKER APEX2 V2.1-0 diffractometer equipped with a graphite-monochromated MoK α ($\lambda = 0.71073$ Å) radiation source in a cold nitrogen stream. All crystallographic data were corrected for Lorentz and polarization effects (SAINT). The structures were solved by direct methods and refined by the full-matrix least-squares method on F^2 with appropriate software implemented in the SHELXTL program package. The guest DMF solvent molecules can be reasonably modeled in **1**. For **2** – **15**, most of the DMF solvent molecules are severely disordered, which hindered satisfactory development of the model; therefore, the SQUEEZE routine in PLATON²⁰ was applied to remove the contributions of electron density from disordered solvent molecules. The outputs from the SQUEEZE calculations are attached to the CIF file. Most of the non-hydrogen atoms were refined anisotropically. In cases of poorly diffracting crystals or poor diffraction data, some of the non-hydrogen atoms were not refined anisotropically. Special details concerning the refinement of each structure are included in the individual CIF files. A summary of the crystallographic data for **1** – **14** is given in Tables 2.4 through 2.9.

Table 2.4 Summary of crystallographic data for **1** – **3**.

compound	1	2	3
empirical formula	C ₁₈ H ₁₆ N ₂ O ₁₀ Zn ₂	C ₂₆ H ₁₆ N ₂ O ₈ Zn ₂	C ₃₄ H ₂₀ N ₂ O ₈ Zn ₂
formula weight	551.07	615.15	715.26
crystal color, habit	colorless, block	colorless, block	colorless, block
crystal dimensions (mm ³)	0.16 x 0.15 x 0.12	0.21 x 0.10 x 0.08	0.12 x 0.08 x 0.08
crystal system	monoclinic	triclinic	triclinic
space group	C2/m	P-1	P-1
<i>a</i> (Å)	13.4458 (17)	10.886 (3)	12.9758 (15)
<i>b</i> (Å)	11.5837 (15)	10.919 (3)	13.1095 (15)
<i>c</i> (Å)	14.0404 (18)	14.091 (3)	13.9258 (16)
α (deg)	90	89.294 (4)	85.310 (2)
β (deg)	105.407 (2)	89.081 (4)	70.710 (2)
γ (deg)	90	79.691 (3)	84.193 (2)
<i>V</i> (Å ³)	2108.2 (5)	1647.6 (7)	2221.5 (4)
<i>Z</i>	4	2	2
ρ (calcd, g/cm ³)	1.736	1.24	1.069
μ (mm ⁻¹)	2.334	1.496	1.118
goodness-of-fit on <i>F</i> ²	1.120	1.004	0.766
<i>R</i>	0.0723	0.0950	0.0488
<i>R_w</i>	0.1717	0.2404	0.0953

Table 2.5 Summary of crystallographic data for **4** and **5**.

compound	4	5
empirical formula	C ₄₈ H ₂₄ N ₄ O ₁₂ Zn ₂	C ₅₂ H ₂₈ N ₄ O ₁₂ Zn ₂
formula weight	979.45	1031.52
crystal color, habit	yellow, block	yellow, block
crystal dimensions (mm ³)	0.132 x 0.113 x 0.078	0.167 x 0.142 x 0.062
crystal system	monoclinic	triclinic
space group	P2(1)	P-1
<i>a</i> (Å)	12.9938 (13)	15.1644 (13)
<i>b</i> (Å)	22.318 (2)	15.1729 (13)
<i>c</i> (Å)	13.0908 (13)	22.273 (2)
α (deg)	90	82.9870 (10)
β (deg)	102.582 (2)	78.4460 (10)
γ (deg)	90	72.7710 (10)
<i>V</i> (Å ³)	3705.1 (6)	4784.9 (7)
<i>Z</i>	2	2
ρ (calcd, g/cm ³)	0.878	0.716
μ (mm ⁻¹)	0.689	0.535
goodness-of-fit on F ²	0.938	0.867
<i>R</i>	0.0492	0.0365
<i>R_w</i>	0.1085	0.0827

Table 2.6 Summary of crystallographic data for **6** – **8**.

compound	6	7	8
empirical formula	C ₄₀ H ₂₀ N ₄ O ₁₂ Zn ₂	C ₄₄ H ₂₀ N ₄ O ₁₂ Zn ₂	C ₅₆ H ₂₈ N ₄ O ₁₂ Zn ₂
formula weight	897.34	927.38	1079.56
crystal color, habit	yellow, block	yellow, columnar	yellow, block
crystal dimensions (mm ³)	n.a.*	0.360 x 0.085 x 0.053	0.179 x 0.147 x 0.135
crystal system	monoclinic	triclinic	monoclinic
space group	C2/c	P-1	P2(1)
<i>a</i> (Å)	46.7805 (8)	13.000 (2)	12.9350 (5)
<i>b</i> (Å)	15.2790 (3)	13.099 (3)	23.2420 (12)
<i>c</i> (Å)	15.5006 (3)	22.379 (3)	12.9350 (5)
α (deg)	90	79.751 (4)	90
β (deg)	107.6180 (10)	83.073 (6)	90
γ (deg)	90	73.205 (6)	90
<i>V</i> (Å ³)	10559.5 (3)	3580.4 (11)	3888.7 (3)
<i>Z</i>	8	2	2
ρ (calcd, g/cm ³)	1.106	0.860	0.922
μ (mm ⁻¹)	1.555	0.71	0.661
goodness-of-fit on <i>F</i> ²	1.070	0.842	0.779
<i>R</i>	0.0479	0.0754	0.0981
<i>R_w</i>	0.1284	0.1485	0.2275

*n.a. = not available. Crystallographic data for **6** was collected at Bruker (Madison, WI). Complete raw data not returned.

Table 2.7 Summary of crystallographic data for **9** and **10**.

compound	9	10
empirical formula	C _{18.5} H ₁₀ N ₄ O ₄ Zn	C ₁₆ H ₈ N ₃ O ₄ Zn
formula weight	417.67	371.62
crystal color, habit	pink, block	red, plate
crystal dimensions (mm ³)	0.057 x 0.050 x 0.028	0.116 x 0.070 x 0.029
crystal system	triclinic	triclinic
space group	P-1	P-1
<i>a</i> (Å)	7.815 (2)	7.7779 (6)
<i>b</i> (Å)	10.746 (3)	10.4643 (8)
<i>c</i> (Å)	13.028 (5)	13.1064 (11)
α (deg)	70.845 (7)	107.0450 (10)
β (deg)	72.778 (4)	105.9350 (10)
γ (deg)	88.703 (5)	91.4850 (10)
<i>V</i> (Å ³)	983.8 (5)	974.10 (13)
<i>Z</i>	2	2
ρ (calcd, g/cm ³)	1.410	1.267
μ (mm ⁻¹)	1.278	1.281
goodness-of-fit on <i>F</i> ²	1.112	0.985
<i>R</i>	0.1351	0.0490
<i>R</i> _w	0.3601	0.1176

Table 2.8 Summary of crystallographic data for **11** and **12**.

compound	11	12
empirical formula	C ₅₈ H ₂₄ Cl ₄ N ₄ O ₁₂ Zn ₂	C ₁₁₆ H ₅₂ Br ₄ N ₈ O ₂₄ Zn ₄
formula weight	1241.35	2522.78
crystal color, habit	orange, columnar	purple, columnar
crystal dimensions (mm ³)	0.210 x 0.058 x 0.050	0.248 x 0.097 x 0.077
crystal system	triclinic	triclinic
space group	P-1	P-1
<i>a</i> (Å)	13.0315 (10)	16.137 (4)
<i>b</i> (Å)	13.0891 (10)	20.233 (5)
<i>c</i> (Å)	26.493 (3)	28.041 (8)
α (deg)	95.436 (2)	107.207 (5)
β (deg)	95.776 (2)	100.971 (5)
γ (deg)	98.050 (9)	90.082 (5)
<i>V</i> (Å ³)	4424.4 (7)	8569 (4)
<i>Z</i>	2	2
ρ (calcd, g/cm ³)	0.932	0.978
μ (mm ⁻¹)	0.704	1.534
goodness-of-fit on F ²	0.834	0.836
<i>R</i>	0.0777	0.0926
<i>R_w</i>	0.1330	0.2478

Table 2.9 Summary of crystallographic data for **13** and **14**.

compound	13	14
empirical formula	C ₂₄ H ₁₂ N ₂ O ₆ Zn	C ₃₆ H ₂₀ N ₆ O ₈ Zn ₂
formula weight	489.73	795.32
crystal color, habit	yellow, plate	pink, columnar
crystal dimensions (mm ³)	0.115 x 0.093 x 0.032	0.217 x 0.101 x 0.076
crystal system	triclinic	triclinic
space group	P-1	P-1
<i>a</i> (Å)	12.0080 (14)	15.267 (7)
<i>b</i> (Å)	12.9860 (15)	16.611 (8)
<i>c</i> (Å)	13.0172 (14)	19.027 (9)
α (deg)	87.740 (2)	93.783 (9)
β (deg)	68.729 (2)	112.122 (8)
γ (deg)	89.764 (2)	113.143 (8)
<i>V</i> (Å ³)	1890.0 (4)	3979 (3)
<i>Z</i>	2	2
ρ (calcd, g/cm ³)	0.861	0.664
μ (mm ⁻¹)	0.675	0.630
goodness-of-fit on F ²	0.945	0.807
<i>R</i>	0.0383	0.1071
<i>R_w</i>	0.0901	0.2489

2.2.5 Adsorption measurements

Adsorption measurements were performed on an Autosorb 1-MP from Quantachrome Instruments. Ultra-high purity grade He, H₂ and N₂ were used for all adsorption measurements. Unless otherwise noted, prior to adsorption analysis each sample was loaded into a sample tube of known mass and heated at 110°C under dynamic vacuum for ~24 hours to remove guest solvent. After evacuation, the sample and tube were re-weighed to obtain the precise mass of the evacuated sample. Nitrogen isotherms were collected at 77K. The BET surface area was determined in the range $0.007 < P/P_0 < 0.05$; the Dubinin-Raduskevich (DR) micropore volume was determined in the range $1 \times 10^{-5} < P/P_0 < 0.01$.

2.2.6 H₂ isosteric heat of adsorption calculation

Hydrogen isotherms were collected at 77K and 87K. Both isotherms were fit to a virial equation of the form given in Equation 2.1.²¹ The isosteric heat of adsorption is then calculated from the fitting parameters using Equation 2.2.

$$\ln p = \ln N + \frac{1}{T} \sum_{i=0}^m a_i N^i + \sum_{i=0}^n b_i N^i \quad (2.1)$$

$$q_{st}(N) = -R \sum_{i=0}^m a_i N^i \quad (2.2)$$

2.3 Results and Discussion

2.3.1 Synthesis

In general, X-ray quality single crystals of structures **1** – **15** were obtained by the static heating of a closed vial containing Zn(NO₃)₂·6H₂O, a dicarboxylic acid ligand and a dipyridyl ligand in DMF or DEF for 2-3 days. All structures were obtained as single crystals for structural determination by X-ray crystallography, but only some were obtained in the bulk as a

pure phase for further characterization. Specific details for each structure are given in subsequent sections.

There are many challenges in preparing bulk samples of a pure MOF phase. For each metal and ligand chosen, there is the possibility of obtaining different structures in the same reaction vessel. For example, the combination of $\text{Zn}(\text{NO}_3)_2 \cdot 4\text{H}_2\text{O}$ and H_2BDC under certain conditions results in MOF-5,²² but under slightly different conditions a two-dimensional square-grid structure is obtained, MOF-2.²³ The synthesis of a pure phase of a mixed-ligand structure however, contains many more variables. In addition to other potential mixed-ligand phases that may grow simultaneously with the desired phase, synthetic conditions that also avoid growth of either single ligand structure must also be realized (in addition to avoiding one- and two-dimensional structures and other amorphous polymeric materials). For some of the mixed ligand structures described here (**5** and **8** in particular) the synthetic conditions that resulted in single crystals suitable for X-ray crystallography also produced a mixture of phases, most likely contaminated with cubic MOFs of the dicarboxylate ligands. Phase purity is verified by comparison of the bulk PXRD to that simulated from the single crystal structure in addition to TGA comparison to the SQUEEZE outputs calculated from the single crystal structure.

2.3.2 Two-fold interpenetrated Zn(II) paddlewheels (1 – 8)

Colorless compounds **1-3** were prepared by heating DMF solutions of $\text{Zn}(\text{NO}_3)_2 \cdot 6\text{H}_2\text{O}$, the corresponding acid and bipy in sealed vials. Single crystal x-ray diffraction measurements confirmed that each is comprised of dimeric zinc units ligated by carboxylate-terminated struts in the *x* and *y* directions and pyridine struts approximately in the *z* direction. Crystallography also established two-fold catenation, Figure 2.1. Although catenation reduces the void volume,

it likely increases the volumetric surface area. Void volumes for **1-3**, as calculated by PLATON from the crystal structures, are 20, 28% and 42%, respectively.

Thermogravimetric analyses (TGA) of compounds **1-3** showed initial mass losses that are consistent with solvent loss as calculated from structural data. Solvent loss starts at ambient temperature and is complete at 140 to 200°C, depending on the compound. Further loss, due to framework decomposition, starts at 380 to 400°C. TGA of the evacuated frameworks show, as expected, only the higher temperature weight loss. Powder x-ray diffraction (PXRD) patterns of the evacuated frameworks point to a high degree of crystallinity and, for all but **3**, give similar but not quite identical patterns to those of freshly synthesized material. Notably, resolution reverses the changes, implying that porosity is retained upon evacuation, but with slight alterations in framework structure. Further evidence of persistent microporosity is provided by N₂ adsorption measurements, shown for **2** in Figure 2.2. Obtained is an approximate Type I Langmuir isotherm with a BET surface area of 663 m²/g. Clearly evident, however, is a slight hysteresis at $P/P_0 \sim 0.1$, possibly reflecting the dynamic structural change in the powder diffraction pattern, Figure 2.2. Similar hysteretic behavior and BET surface area have been reported in a copper analogue of **2**²⁴ as well as in two-dimensional layered framework materials.²⁵ Notably, the most compact of these compounds, **1**, did not take up nitrogen.

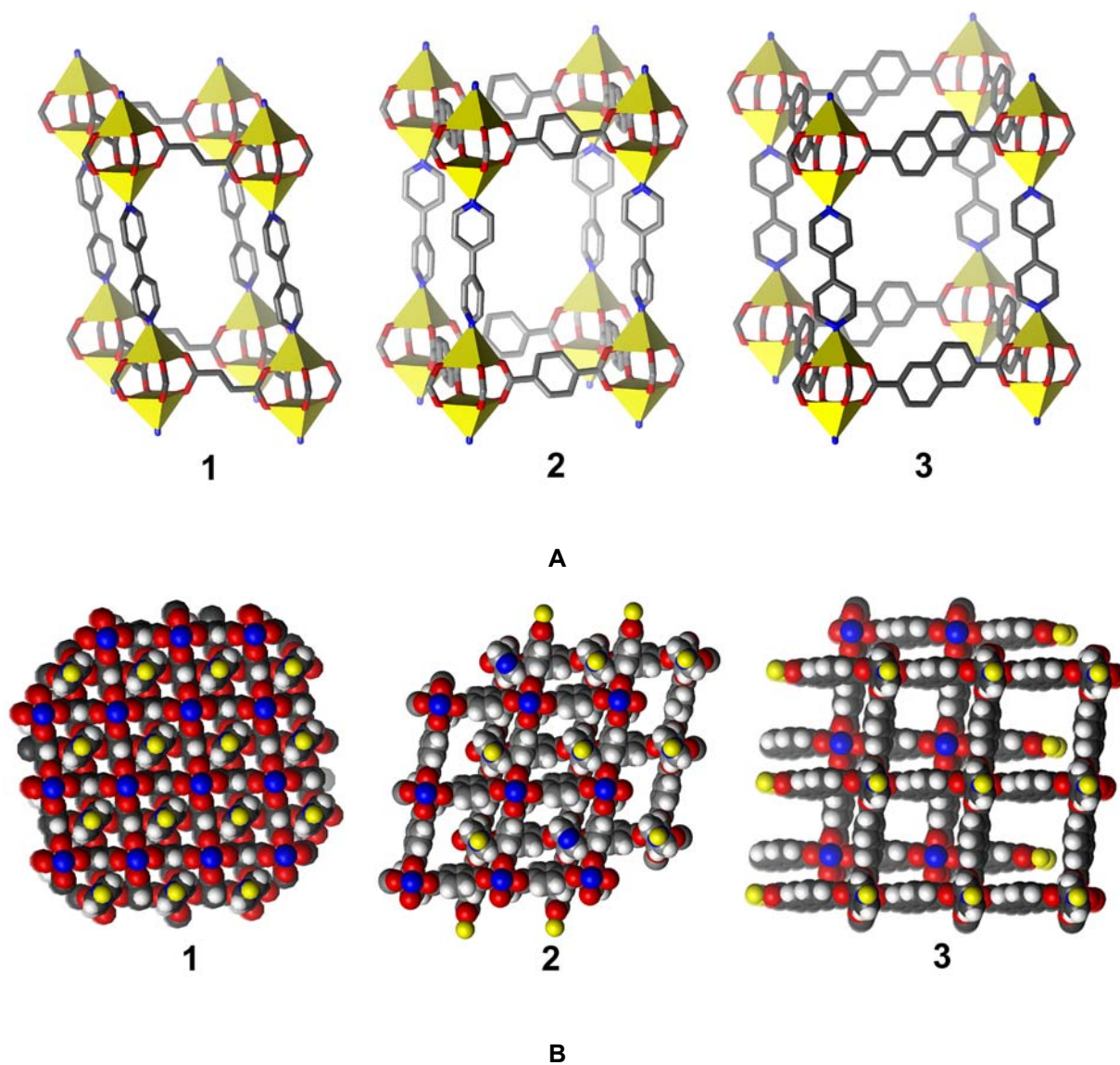


Figure 2.1 A) Crystal structures of **1** – **3**, only one network shown for clarity. The yellow polyhedra represent the zinc ions. Carbon: gray. Oxygen: red. Nitrogen: blue. Hydrogens omitted for clarity. B) Packing diagram for **1** – **3** down bipy axis showing two-fold interpenetration.

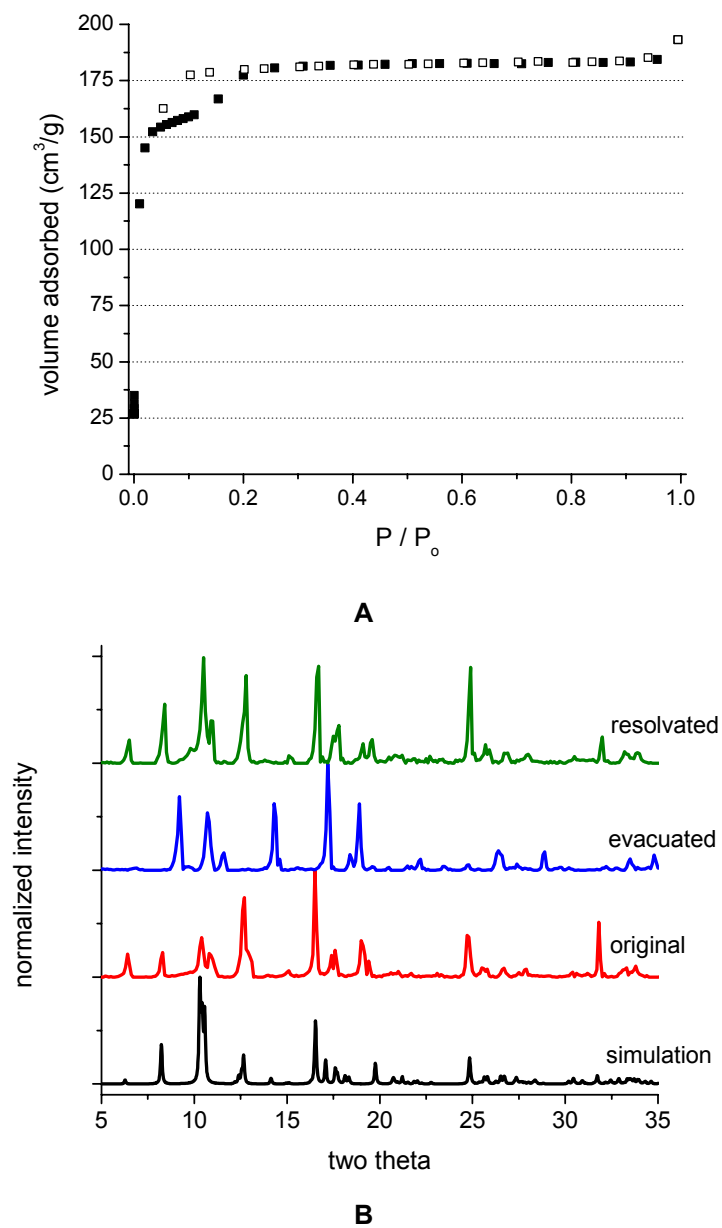


Figure 2.2 A) N₂ adsorption isotherm of **2**. Closed symbols, adsorption; open symbols, desorption. B) PXRD of **2** as synthesized, evacuated, and resolvated; demonstrating dynamic framework behavior.

Compared with cubic MOFs comprising a single ligand type, mixed-ligand MOFs should, in principle, be obtainable in much greater variety. Toward that end, two additional MOFs, both featuring diPyNI in place of bipy, were prepared by a method analogous to that for **1** – **3**. Single-crystal structures of $\text{Zn}_2(\text{NDC})_2(\text{diPyNI}) \cdot n\text{DMF}$ (**4**) and $\text{Zn}_2(\text{bpdc})_2(\text{diPyNI}) \cdot n\text{DMF}$ (**5**) show the compounds to be isorecticular with **1**–**3** (Figure 2.3). The guest-accessible volumes (PLATON) for **4** and **5** are 54% and 64%, respectively. TGA and PXRD show that **4** is stable in evacuated form up to 400°C. N_2 adsorption measurements confirm the permanent microporosity of **4** and give a BET surface area of 802 m^2/g . Low-pressure H_2 adsorption measurements of **4** reveal 0.93 wt% uptake at 77K and 1 atm. Comprehensive doping and adsorption studies with **4** are outlined in Chapters 3 and 4. Unfortunately attempts to grow **5** in a pure phase were unsuccessful and most likely contaminated with cubic MOFs of the bpdc ligand.

Interestingly, compounds **4** and **5** are yellow in spite of the off-white color of free ligand and both are weakly photo luminescent. In light of previous work with discrete supramolecular assemblies,¹⁶ we anticipated that diPyNI-containing MOFs might be redox active. Preliminary studies with **4** established that it is readily reducible by THF solutions of lithium naphthalenide.²⁶ Accompanying the reduction is a change in color to dark green/brown, Figure 2.4. The change is reversed upon exposure to air. PXRD measurements show that the framework structure is retained following reduction and re-oxidation. The anticipated chemical similarity of Zn(II)-bound bipy to the well known organic redox reagent methylviologen ($\text{N,N}'$ -methyl-4,4'-bipyridine) prompted us to examine **2** briefly as well. This compound proved similarly reducible, and reversibly turns violet, Figure 2.4. Framework reduction obviously also offers a mechanism for doping with specific cations.

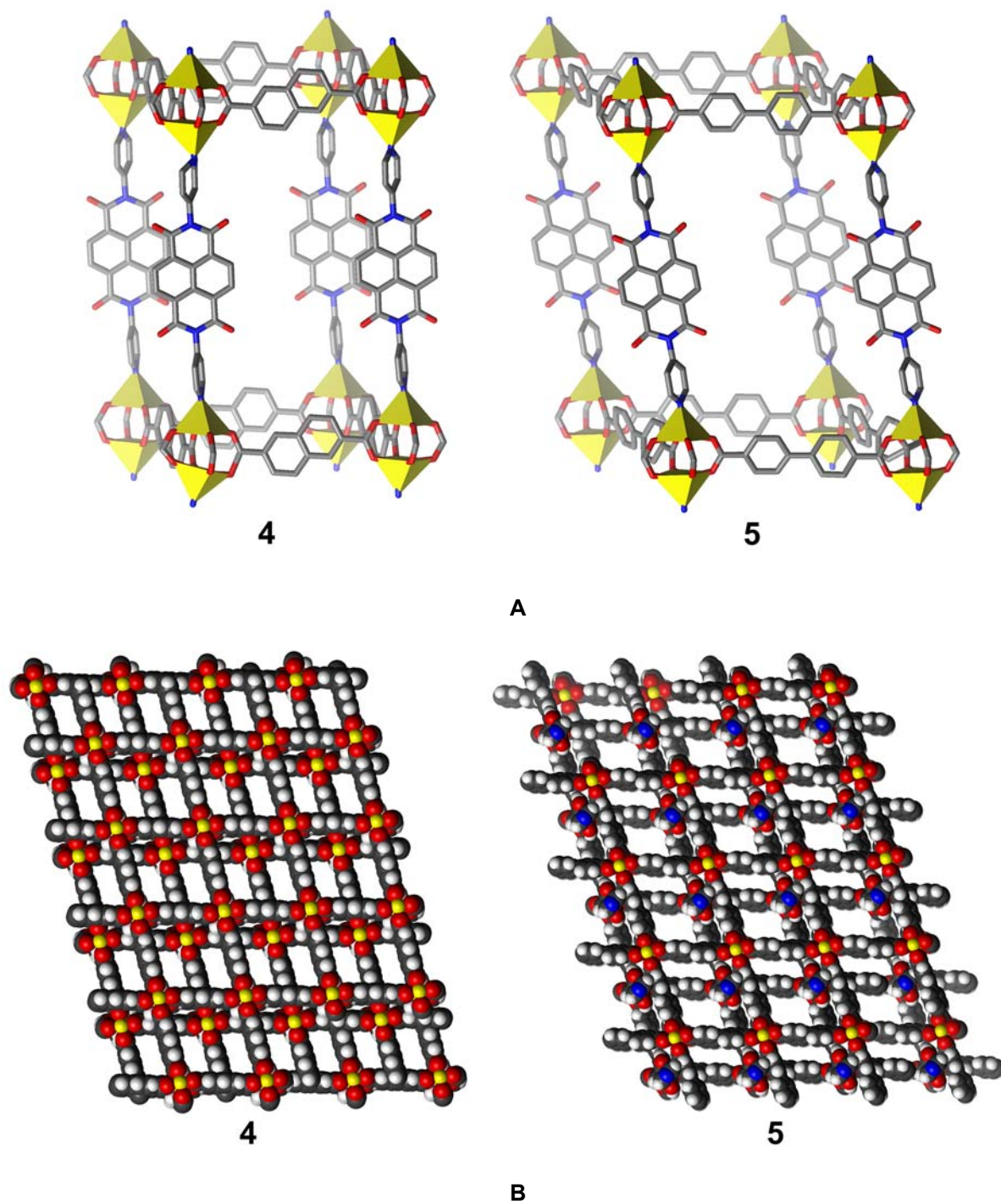


Figure 2.3 A) Crystal structures of **4** and **5**, only one network shown for clarity. B) Packing diagrams of **4** and **5** down dipyrrolyl axis, illustrating two-fold catenation.

**A****B**

Figure 2.4 A) Color change of **4** (left) upon exposure to lithium naphthalenide (right). B) Color change of **2** (left) upon exposure to lithium naphthalenide (right).

Structures **6** – **8** were acquired in attempts to grow mixed-ligand paddlewheel MOFs without catenated networks. For structure **6**, it was presumed that the short length of the BDC ligand (relative to NDC and bpdc in structures **4** and **5**) as compared to the width of the diPyNI ligand would preclude catenation in a framework material. However, crystallographic analysis did in fact reveal two-fold catenation with 43% solvent accessible void volume, Figure 2.5. Structure **6** was obtained as a pure phase in quantities large enough to perform adsorption measurements. N₂ adsorption measurements verify the microporous nature of this material though a Type I isotherm with no hysteresis and a BET surface area of 531 m²/g. Interestingly, the both the H₂ uptake and heat of adsorption are larger than **4**, despite the lower surface area and smaller micropore volume (0.30 cm³/g, **4**; 0.21 cm³/g, **6**), Figure 2.5. As all other factors for these structures are equal (i.e. metal cluster, ligand functionality, pore shape, interpenetration), the small pore size of **6** demonstrably enhances H₂ binding compared to **4**. Additionally, at the isotherm conditions measured, well below the H₂ saturation limit of these two structures, this enhanced binding energy results in about 16% greater uptake.

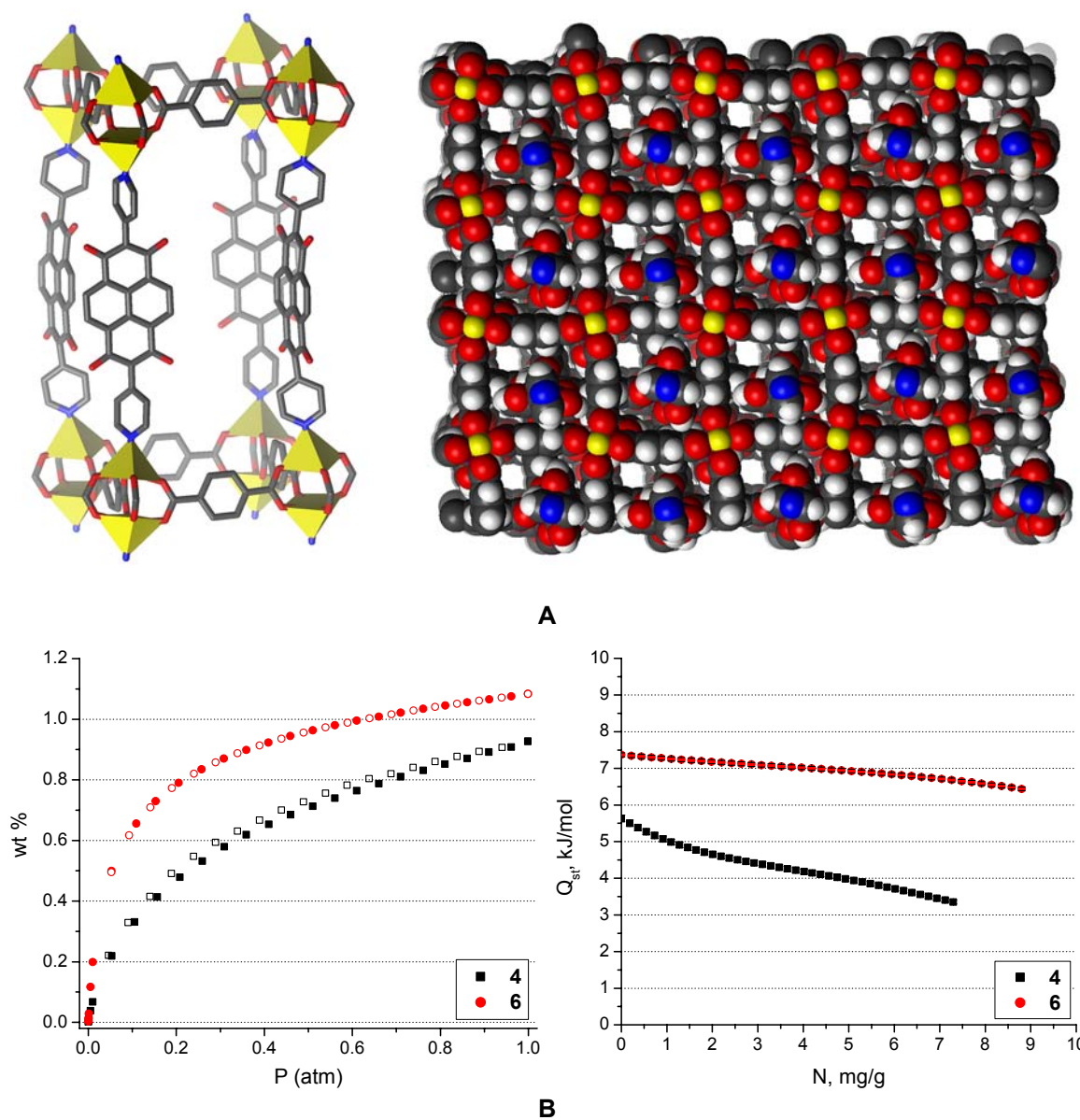


Figure 2.5 A) Crystal structure of **6**, one network (left) and packing diagram (right). B) 77K H₂ uptake (left) and isosteric heat of adsorption (right) of **6** compared with **4**.

Following from structure **4**, another carboxylic acid was employed in structure **7** to probe the effect subtle differences that ligand interactions might have upon interpenetration in this library of materials. The cca ligand used in **7** has two fewer carbons than NDC, but it is still a conjugated system. In this case, the slight changes in carboxylate structure did not greatly effect the catenation within the framework. Like **4**, **7** features two-fold catenation arising from π - π stacking interactions between the carboxylate ligand and diPyNI.

The design strategy used in planning the synthesis of structure **8** was slightly different than that of **6** and **7**. Rather than modifying the dicarboxylate length or shape, the dipyridyl ligand was adapted to possess considerably more steric bulk²⁷ surrounding the Zn paddlewheel with quinoline linkage rather than pyridine linkage. Despite this added steric bulk near the metal cluster, single crystal analysis of **8** revealed yet another catenated structure, Figure 2.6. Notably, under the synthetic conditions that resulted in a single crystal of **8** (yellow blocks), a white microcrystalline powder was also present. The yellow crystalline material was successfully isolated from the mixture in high purity by solvent-based density discrimination between the two phases.¹⁹ PXRD of the as-synthesized mixture and then of the separated material confirms the phase purity of **8**, Figure 2.6.

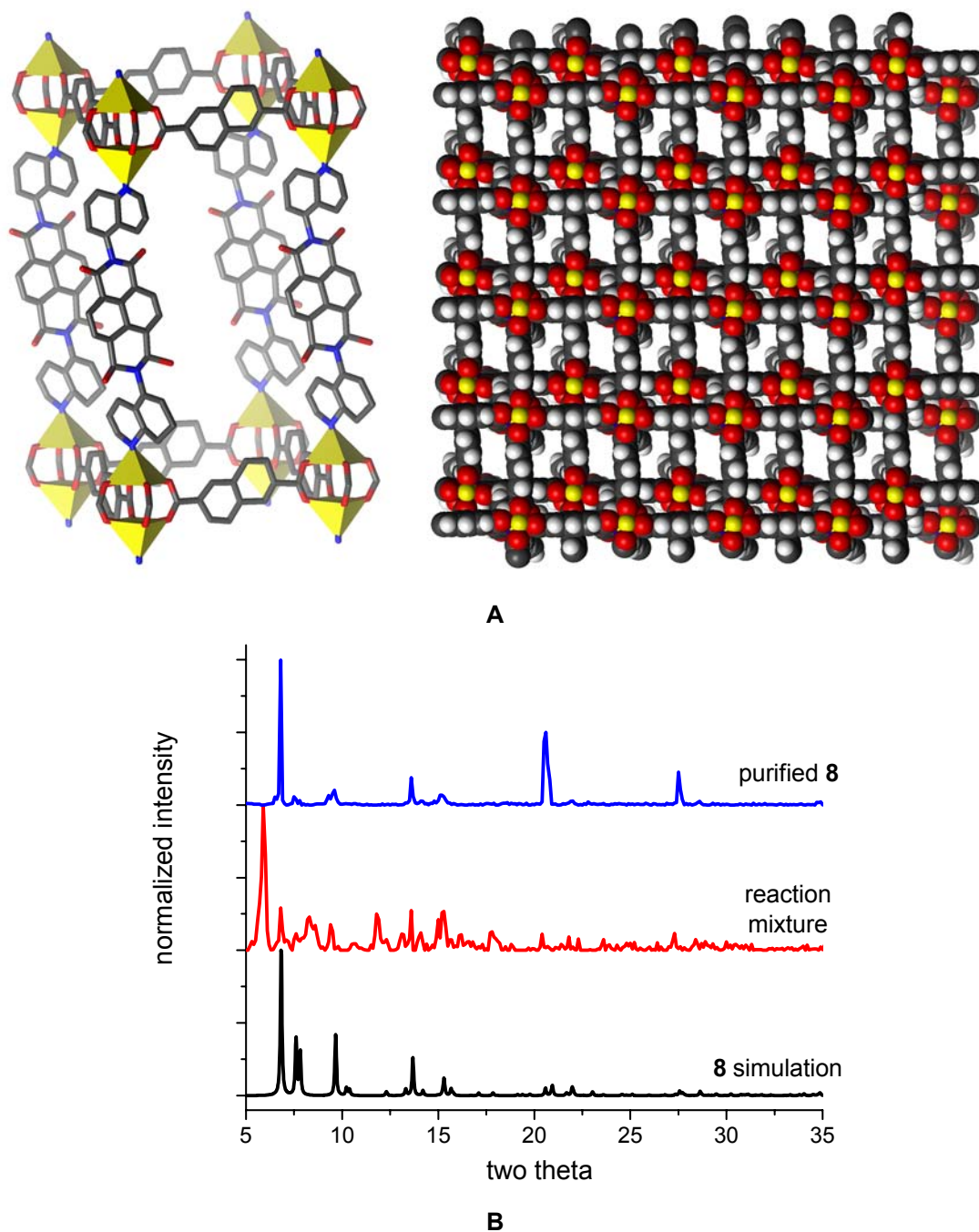


Figure 2.6 A) Crystal structure of **8**, one network and packing diagram. B) PXRD of **8**, reaction mixture and purified.

2.3.3 Three-fold interpenetrated Zn(II) paddlewheels (**9**, **10**)

Structures **9** and **10** contain the diPyTz ligand. Like diPyNI, this ligand was chosen because of its established redox activity; it has two reversible reductions at -1.81 and -2.50 vs. ferrocene⁺⁰. As opposed to structures **1** – **8** which exhibit two-fold catenation, the structures formed with this ligand are three-fold catenated, Figure 2.7. Comprehensive doping and adsorption studies of **9** are presented in Chapter 5. Bulk synthesis of **10** in a pure phase was not pursued.²⁸

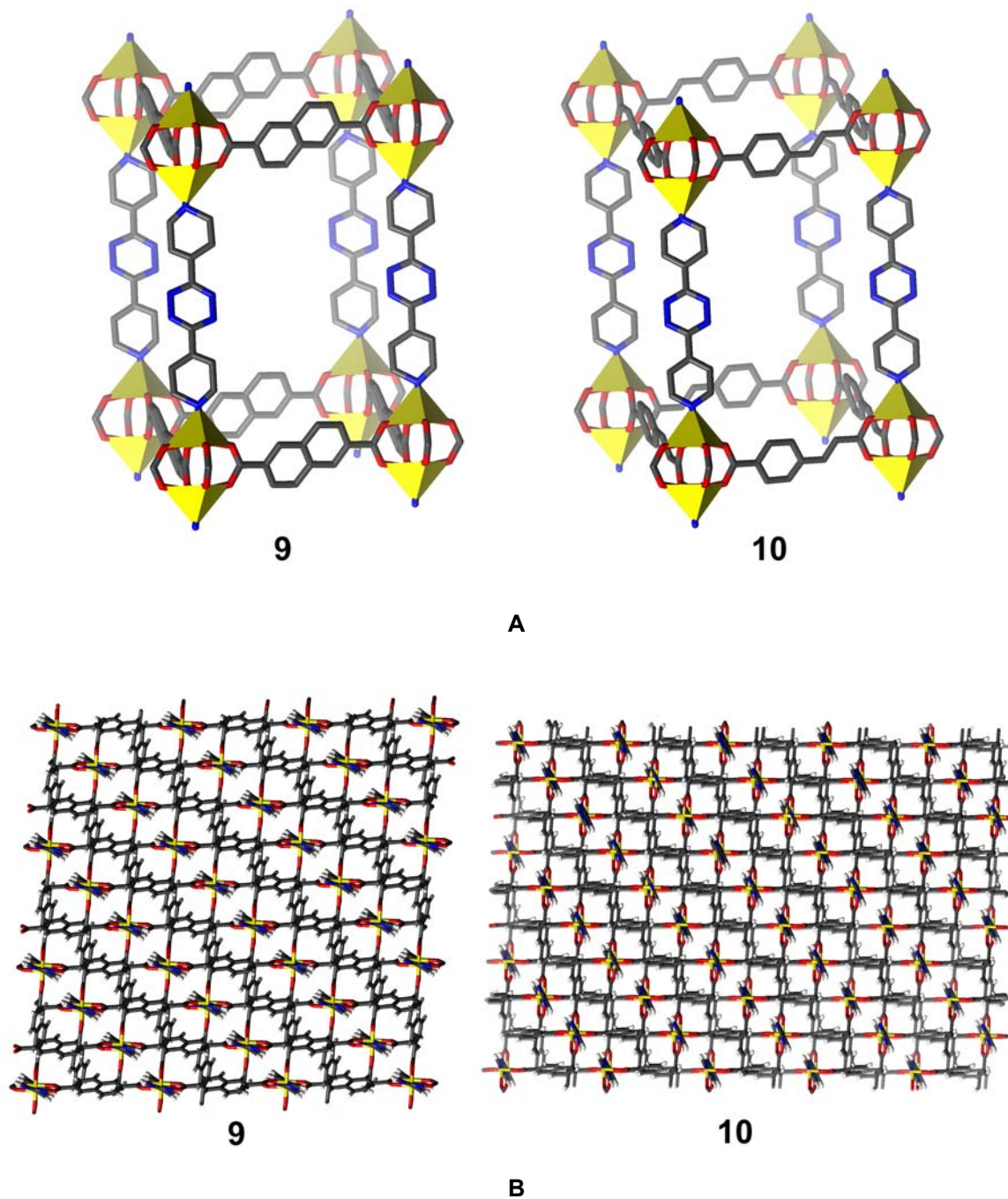


Figure 2.7 A) Crystal structures of **9** and **10**, one network only. B) Packing diagram of **9** and **10**, illustrating three-fold interpenetration.

2.3.4 Perylene-diimide Zn(II) paddlewheels (**11** – **12**)

Perylene-diimide MOF struts were targeted because of the broad range of tunability available with respect to solubility, redox potential, UV-Vis absorbance and fluorescence spectral features.²⁹ By necessity, the imide positions are functionalized with pyridyl groups to facilitate zinc coordination but the perylene bay positions remain open for further functionalization. All four bay positions are functionalized with chlorine atoms in structure **11** and only two positions are functionalized with bromine atoms in structure **12**, Figure 2.8. Crystallographic analysis of **11** and **12** reveals a large deviation from planarity in the perylene core (torsion angles of 39° and 26° respectively), a result of the bulky halogen substituents avoiding steric interaction with one another or neighboring protons. Both structures feature two-fold catenation with substantial solvent accessible void volume remaining, 54% in **11** and 55% in **12** as calculated by the SQUEEZE routine in PLATON. Both of these structures were prepared in large enough quantities to prompt characterization via adsorption measurements. Analysis of the N₂ adsorption isotherms, Figure 2.9, gives BET surface areas of 195 m²/g and 91 m²/g for **11** and **12** respectively. Low-pressure H₂ uptake and heat of adsorption were also measured for **11** and **12**, Figure 2.9. The overall H₂ uptake does not compare well with many other Zn(II) paddlewheel structures; at 1 atm and 77K the uptake for **11** is only 0.56 wt% H₂. However, the large difference in H₂ heat of adsorption between these two nearly isostructural materials is quite remarkable.

While the perylene diimide struts present an immense opportunity to introduce many different functional groups within these and similar framework materials, these preliminary studies suggest that they are “too heavy” to be relevant for H₂ storage applications. Nonetheless, the broad scope of properties offered by perylene diimide ligands could present

potential in anisotropic materials, separations, sensing, and porous, tunably fluorescent solid-state materials.

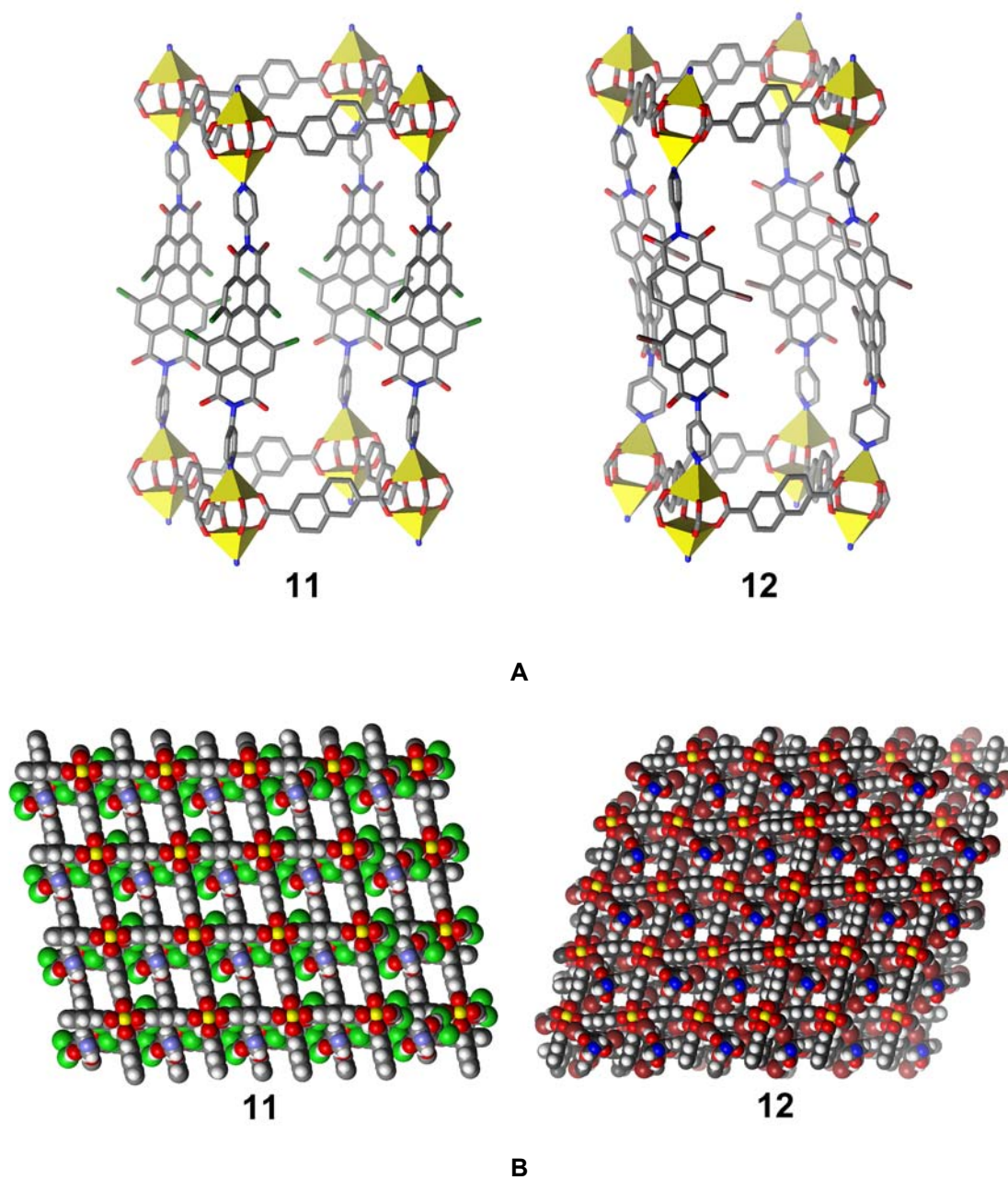
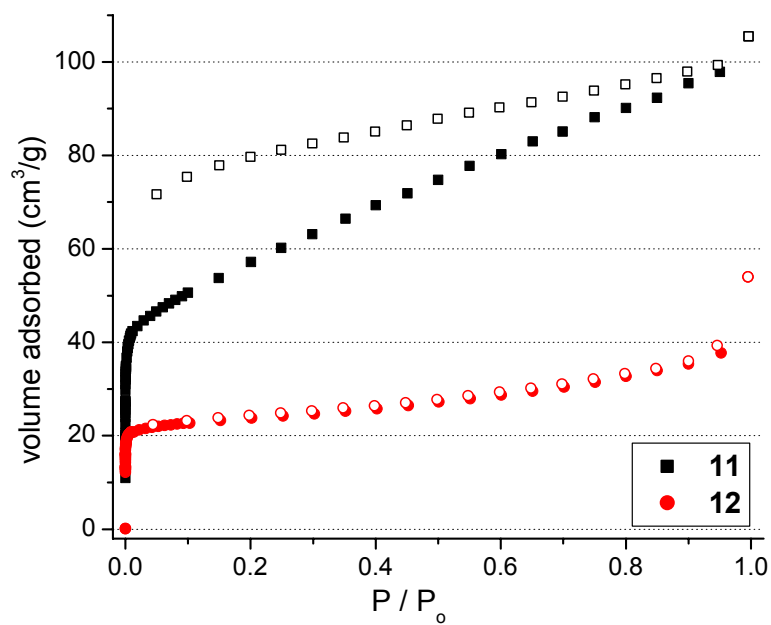
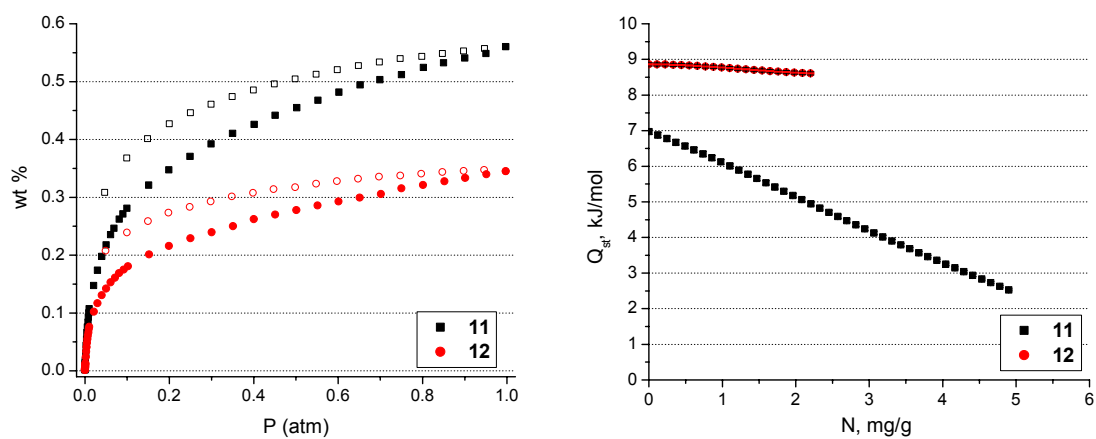


Figure 2.8 A) Crystal structures of **11** and **12**, one network only. B) Packing diagram of **11** and **12**, illustrating two-fold interpenetration.



A



B

Figure 2.9 A) N_2 adsorption isotherms for **11** and **12**. B) 77K H_2 isotherms (left) and H_2 isosteric heat of adsorption (right) plots for **11** and **12**.

2.3.5 Non-interpenetrated Zn(II) paddlewheels (**13** – **15**)

Favorable ligand interactions such as π - π stacking and simple attractive van der Waals forces often preclude formation of large open void spaces within MOF materials. This is well demonstrated in structures **1** – **12**, which all feature some level of catenation, and most of them are interwoven as opposed to interpenetrated, which maximizes favorable ligand-ligand interactions. One approach to avoid catenation is to employ ligands with some steric hindrance around the coordination sites; structure **8** was obtained with this intent.

By simply changing the pyridyl connectivity from para- to meta- with respect to the ligand core, we reasoned at the very least that frameworks containing this connectivity would possess unique or novel pore geometry which may influence sorption properties. Somewhat serendipitously, single crystals of *non*-catenated structures **13** and **14** were obtained. Crystallographic analysis indeed verifies that there is no catenation within these frameworks and for both of the structures, the pyridyl connectivity is in a *trans* fashion, Figure 2.10. A further indicator of the large open pore structure of these frameworks is the calculated solvent accessible void volume: 56% (**13**) and 67% (**14**), both of which are larger than the two- and three-fold catenated analogues (structures **4** and **9**). Despite many attempts to grow structures **13** or **14** in pure quantities large enough for sorption analysis, these materials could not be obtained in a pure phase. PXRD analysis suggests that the major phase formed in attempted syntheses is IRMOF-8, the cubic MOF formed from H₂NDC.

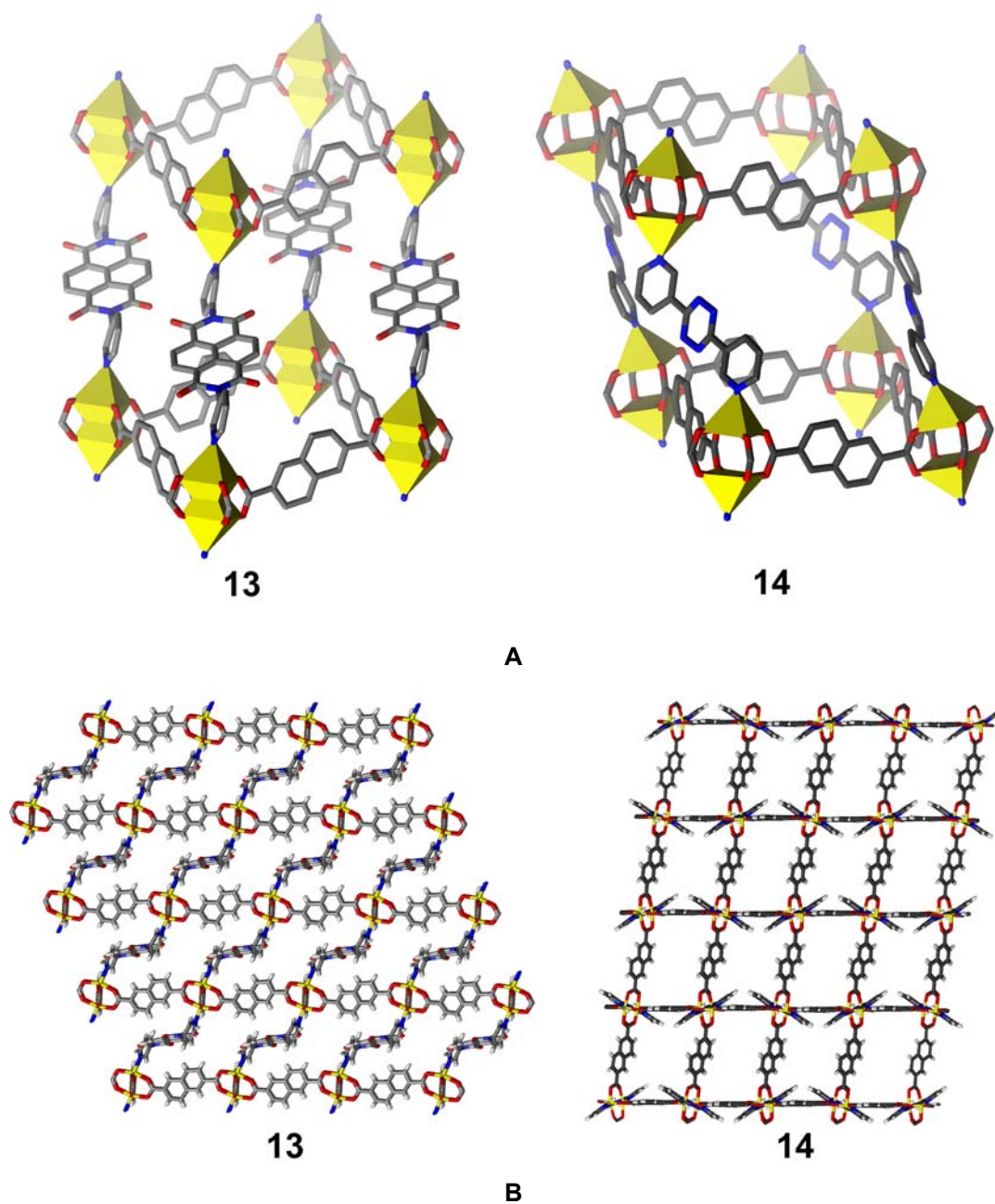
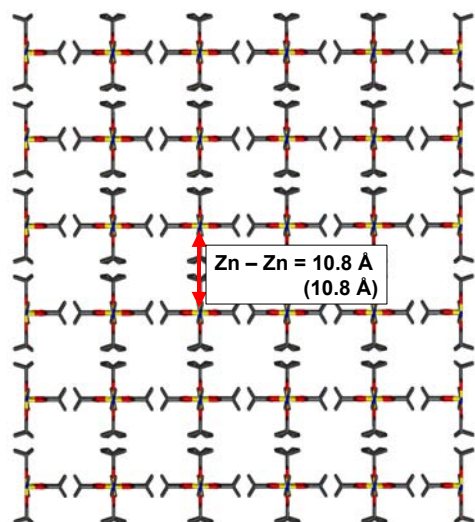
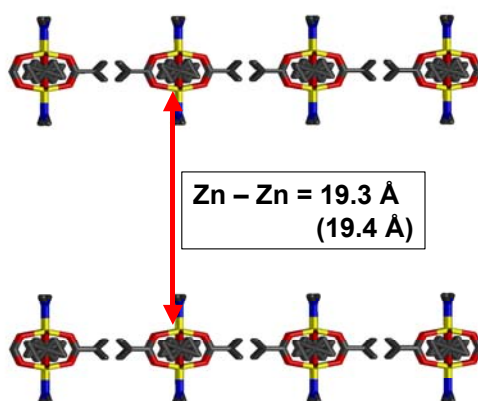


Figure 2.10 A) Crystal structures of **13** (left) and **14** (right). B) Packing diagram of **13** down b-axis (left) and **14** down a-axis (right), illustrating non-catenated frameworks.

Continuing the strategy to obtain non-catenated frameworks by increasing the steric bulk surrounding the coordination site, 1,4-naphthalenedicarboxylic acid was chosen as an analogue to 2,6-naphthalenedicarboxylic acid, which has been prolific in the Zn(II) paddlewheel structures described here, see Table 2.3. As expected, the combination of 1,4-NDC with diPyNI resulted in a paddlewheel framework with no catenation present, structure **15**, Figure 2.11. Although quite large (0.300 mm x 0.197 mm x 0.134 mm for example) amber crystals were grown from these ligands, the diffraction data is very weak. Presumably the large open pores contain many disordered solvent molecules which contribute to poor diffraction; not all of the ligand atoms could be found in the electron density map. However, many of the atoms can be found and the Zn positions can be refined anisotropically. The Zn positions of **15** are the effectively the same as in structure **6**, the catenated BDC analogue. Furthermore, there is no large electron density in the pores which would indicate the Zn paddlewheels of another catenated framework. In this case, the bulk material could be formed in a pure phase, as verified by PXRD and strongly suggested by TGA by the large and rapid solvent loss, Figure 2.12. Contrary to many of the other structures however, activation of this material by removing the guest DMF molecules under vacuum at elevated temperature completely destroyed the structure, evidenced by extremely low N₂ uptake and surface area, Figure 2.12. Exchange of DMF for more volatile guest solvents such as CHCl₃, THF, methanol, and ethanol followed by gentle activation under vacuum at room temperature resulted in a slight increase in surface area (up to 96 m²/g) but not at the levels expected for similar structures. PXRD and TGA of the activated and re-solvated materials indicate partial structure collapse upon activation.



A



B

Figure 2.11 Packing diagrams of crystal structure for **15** (partially solved), illustrating non-catenated framework. Distances shown for Zn-Zn positions; distances in () are those for structure **6**. A) View down c axis, B) view down b axis.

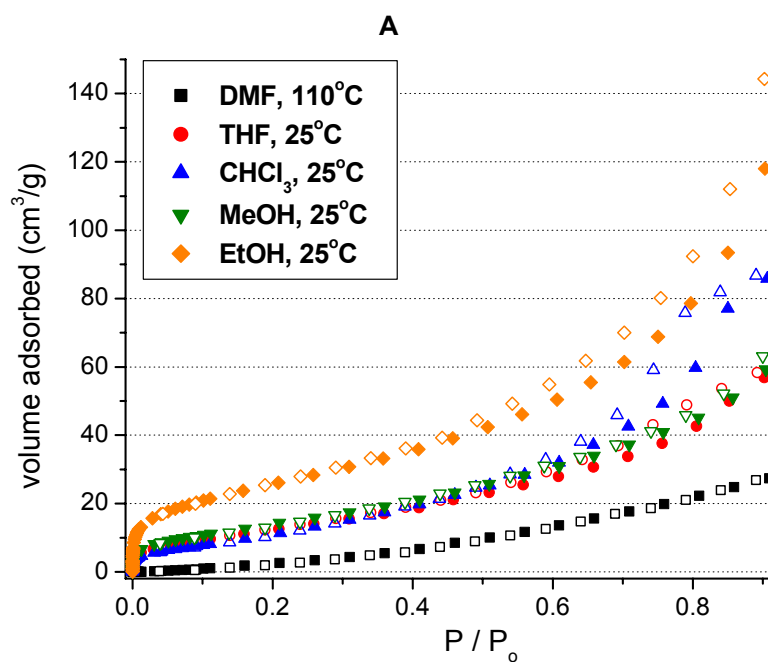
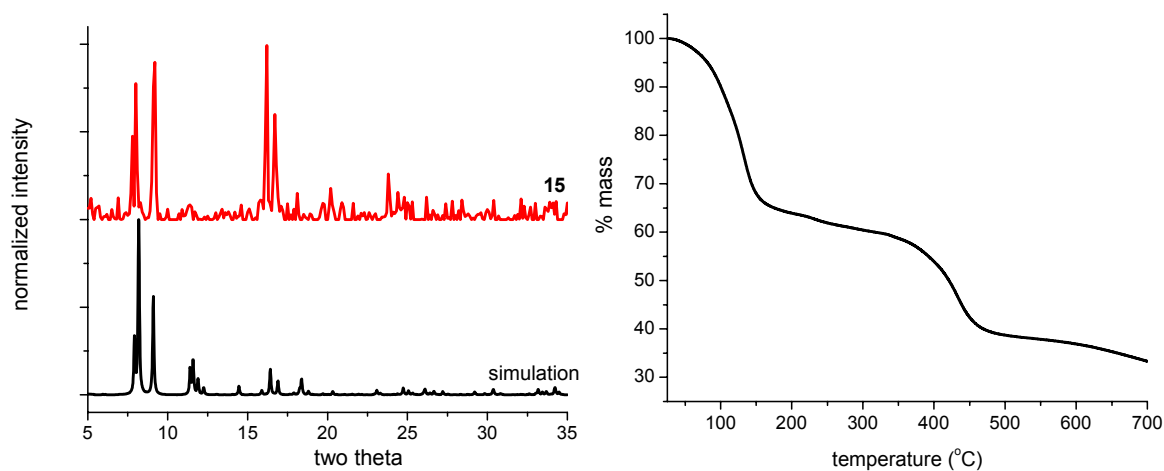


Figure 2.12 A) PXRD and TGA of as synthesized **15**. B) N_2 adsorption isotherms under various activation conditions.

Given the immense versatility in structure and functionality accessible in mixed-ligand Zn(II) paddlewheels, a successful pursuit of non-catenated frameworks would hold immediate promise for gas storage and similar applications. However, many of the targeted “reducible” ligands used in structures **1** – **15** are large, flat, aromatic molecules that tend to aggregate in solution, most likely influencing the solid-state structure. Judicious choice of new ligands and synthetic conditions will be necessary to obtain non-catenated, permanently porous frameworks with redox activity in the solid state.

2.4 Conclusions

In summary, a family of 15 anisotropic open-framework compounds has been obtained based upon paddlewheel-type coordination of Zn(II) pairs in two dimensions and pyridyl ligand pillaring in the third. The mixed-ligand approach has been used to tune channel dimensions, to introduce otherwise unstable metal-pyridine linkages, and to engender framework redox reactivity. Additional structures from our research group not described here,^{9,30} only reinforce the versatility of this approach to introduce any number of functionalities into open framework materials.

Following from the development and realization of these structures, subsequent chapters will explore their potential and utility, specifically towards H₂ storage applications. To begin, Chapter 3 will use structure **4** to introduce the first experimental example of a cation-doped/reduced framework that exhibits substantial H₂ uptake and binding enhancement over the neutral material.

**Chapter 3. Chemical Reduction of Metal-Organic Framework Materials as a Method to
Enhance Gas Uptake and Binding**

(previously published in part in Mulfort, K. L.; Hupp, J. T. *J. Am. Chem. Soc.* **2007**, *129*, 9604-9605.)

3. Chapter Overview

Chapter 1 discussed the potential of using solid-state materials, specifically MOFs, to address hydrogen storage concerns, and chapter 2 introduced a family of mixed-ligand MOFs, many of which exhibit permanent microporosity and, by changing either or both struts, have interchangeable functionality. We have purposely targeted redox-active ligands as struts in a number of these structures to address H₂ storage concerns. By using redox-active struts to create these solid-state materials, we can begin to exploit their inherent redox behavior to post-synthetically manipulate their charge and concomitant charge-balancing moieties within the framework. In this chapter I will describe a method by which to chemically reduce the struts within a mixed-ligand MOF and subsequently dope the framework with alkali metal cations, specifically Li⁺. This reduced and doped material does indeed exhibit enhanced hydrogen gas uptake by almost double the original level. Additionally, the reduced framework displays substantially greater hydrogen heat of adsorption over the entire loading range, indicative of stronger H₂-MOF interactions. However, the increase in H₂ loading is much greater than would be expected for only charge-quadrupole interactions induced by the lithium cations or the newly charged ligands. Further analysis by nitrogen adsorption isotherms reveals unprecedented hysteresis in the reduced material which is not present in the original material. We suspect that structural changes in the reduced material, perhaps induced by cation doping, is largely responsible for the large increase in H₂ uptake.

3.1 Introduction

Permanently porous metal-organic framework (MOF) materials are of tremendous current interest both because of their well-defined, low-density structures and their enormous potential in applications such as gas storage,¹⁻⁴ catalysis,^{5,6} and small molecule sensing.⁷ We are particularly

interested in hydrogen storage. Impressive advances have been made here in a surprisingly small amount of time.^{8,9} Nevertheless, there have been no reports of MOF-based H₂ storage that meet the published DOE target levels at non-cryogenic temperatures.^{10,11} Clearly there is a need for further enhancement. Rather than attempting to effect slight structural changes, such as choice of ligand or metal which may lead to incremental enhancements in H₂ uptake, we have chosen to examine framework reduction as a method to dramatically enhance hydrogen uptake as well as the heat of adsorption. We reasoned that framework reduction might well boost adsorption by: a) increasing the polarizability of organic struts, thereby strengthening adsorbate/framework van der Waals interactions, b) introducing charge-compensating cations capable of binding gas molecules via charge/quadrupole, or more specific interactions, and/or c) coulombically displacing interwoven frameworks, thereby enhancing accessible surface area.

3.2 Experimental

3.2.1 Materials and methods

Commercial reagents were purchased from Sigma-Aldrich (ACS grade) and used as received unless otherwise noted. THF and DMF were purified using a two-column solid-state purification system (Glasscontour System, Jeorg Meyer, Irvine, CA). ICP spectroscopy was conducted on a Varian model ICP spectrometer that is equipped to cover the spectral range from 175 to 785 nm. Samples (3-5 mg) were digested in 1:1 H₂SO₄:H₂O₂ and heated at 120°C until the solution became clear and colorless and no further vapor was produced. An aliquot of this concentrated acid solution was diluted to 5% in DI H₂O and analyzed for Li (610.365 nm) and Zn (202.548 nm) content.

3.2.2 Framework modification

All manipulations were carried out in an argon atmosphere glove box. A small piece of lithium metal (3.2mm wire in mineral oil) was immersed briefly in THF to remove excess mineral oil. *Caution: Lithium metal is extremely reactive with water and potentially reactive with nitrogen! All manipulations with lithium metal were undertaken in an argon atmosphere glove box.* Any dark oxide on the surface of the wire was scraped away to reveal the shiny metal surface. Lithium (0.4mg, 0.057mmol) was added to 5 ml DMF in a round bottom flask. The lithium was allowed to interact with the DMF for one hour, in which time the solution became slightly cloudy, but the lithium was not completely dissolved. A sample of **4** (85mg, 0.065mmol) was then added to the Li-DMF solution. The solution immediately turned from colorless to green and the solid from yellow to brown. The flask was manually agitated for 10 minutes and the solid was isolated on a coarse frit. The solid was washed with DMF (10 x 1 ml) and THF to dry (2 x 1 ml). The reduced sample, $4^{\cdot-}\text{Li}^+$, is air sensitive and will oxidize upon exposure to air, indicated by color change back to yellow. The Li/Zn ratio in $4^{\cdot-}\text{Li}^+$ was measured by ICP. Anal. calcd. for $4^{\cdot-}\text{Li}^+ \cdot 5\text{H}_2\text{O}$, $\text{C}_{48}\text{H}_{24}\text{N}_4\text{O}_{12}\text{Li}_{0.06}\text{Zn}_2$: C, 53.88; H, 3.20; N, 5.24. Found: C, 53.86; H, 2.98; N, 5.21. PXRD and TGA of oxidized $4^{\cdot-}\text{Li}^+$ were used to verify structural integrity through reduction and oxidation.

3.3 Results and discussion

3.3.1 Framework reduction

As a starting point, we chose a material whose synthesis and structure was described in Chapter 2, $\text{Zn}_2(\text{NDC})_2(\text{diPyNI})$ (**4**),¹² Figure 3.1. This compound features two-fold interpenetration yet retains 54% solvent-accessible void volume. Extensive experimental work

has demonstrated that **4** is robust and permanently porous. Most interestingly, **4** contains the redox active ligand diPyNI which is reversibly reducible at -0.79 and -1.30V vs. the ferrocene couple.¹³

Several methods of framework reduction were examined, including employing a redox shuttle and interaction with the solvated electron in liquid ammonia. Surprisingly, the most effective approach turned out to be direct reduction with lithium metal in DMF as solvent, Scheme 3.1. Immediately upon exposure to Li^0 in DMF, **4** changed color from bright yellow to brown. The change mimics the color change observed in solutions of the diPyNI ligand alone. PXRD and TGA confirm the structural integrity of **4** through reduction and subsequent oxidation by exposure to air, Figure 3.2. ICP methods were used to measure the Li^+ loading within the reduced MOF, designated **4** Li^+ . Preliminary results indicate that sub-stoichiometric amounts of lithium, $\sim 5\text{ mol}\%$, are optimal for improving gas adsorption.

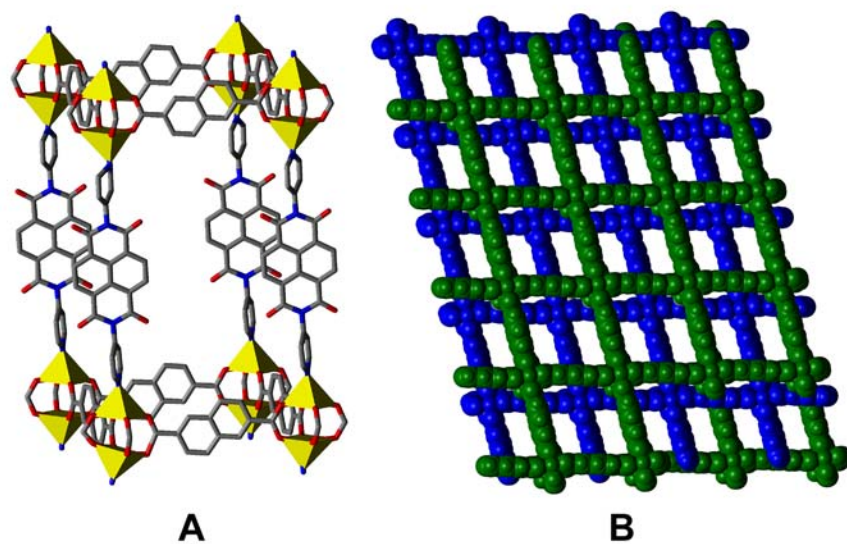
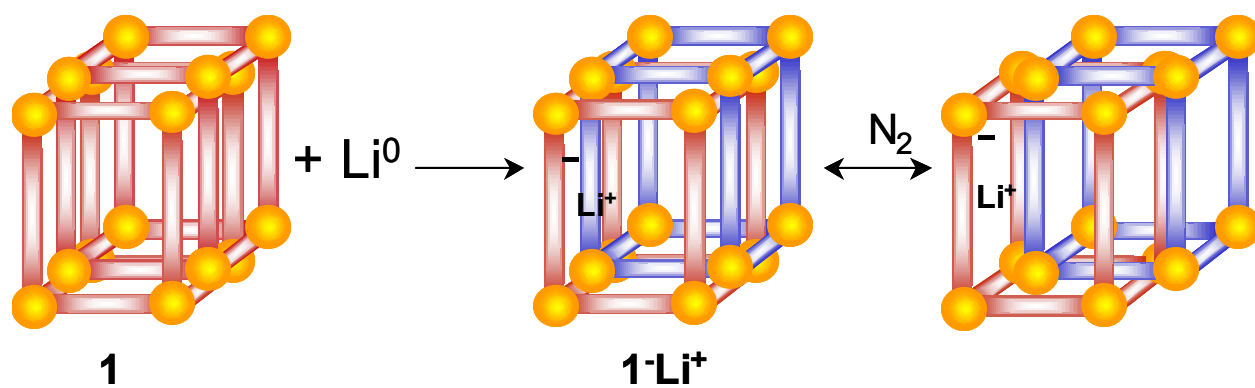


Figure 3.1 A) Crystal structure of **4** omitting interwoven second network. The yellow polyhedra represent the zinc ions. Carbon: gray. Oxygen: red. Nitrogen: blue. B) Packing diagram of **4** down diPyNI axis showing two-fold interpenetration.



Scheme 3.1 Reduction of **4** in DMF to form **4·Li⁺**. N_2 adsorption measurements suggest a reversible structural change, represented speculatively here as framework displacement.

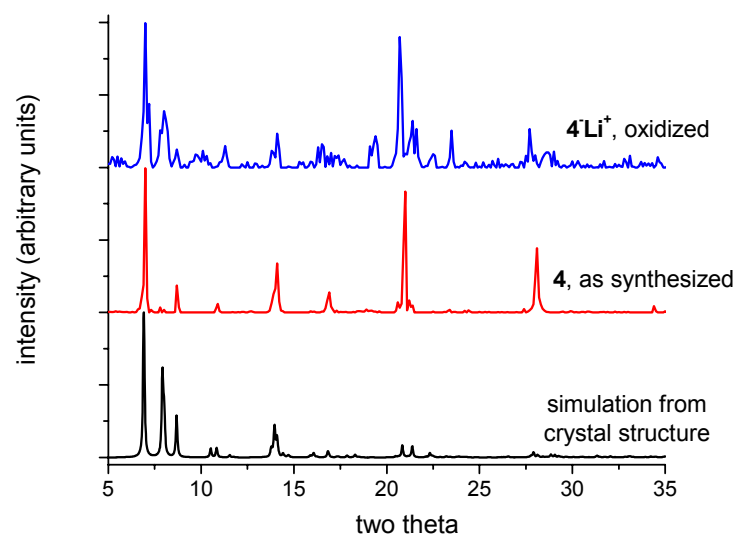
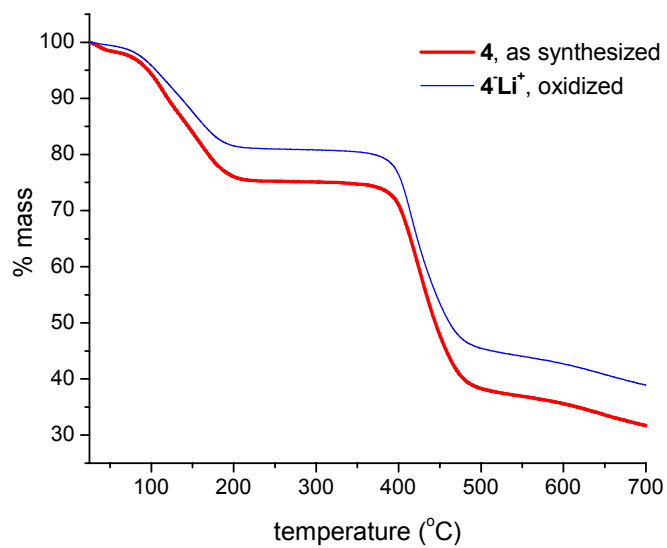
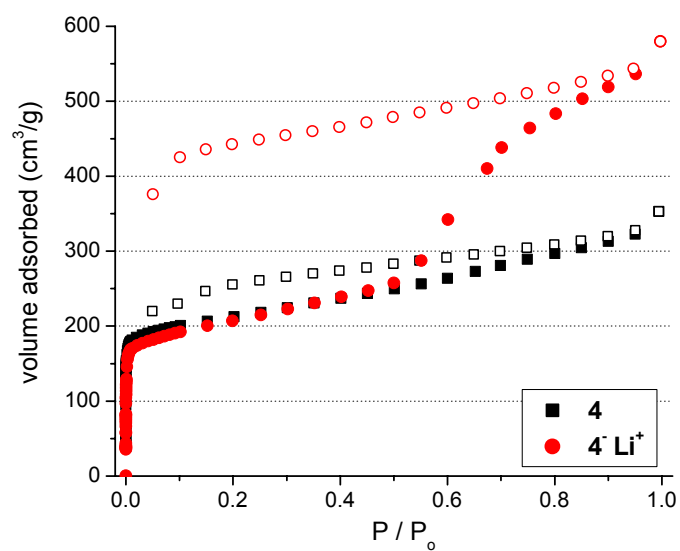
**A****B**

Figure 3.2 A) PXRd and B) TGA of **4** and oxidized **4Li⁺**.

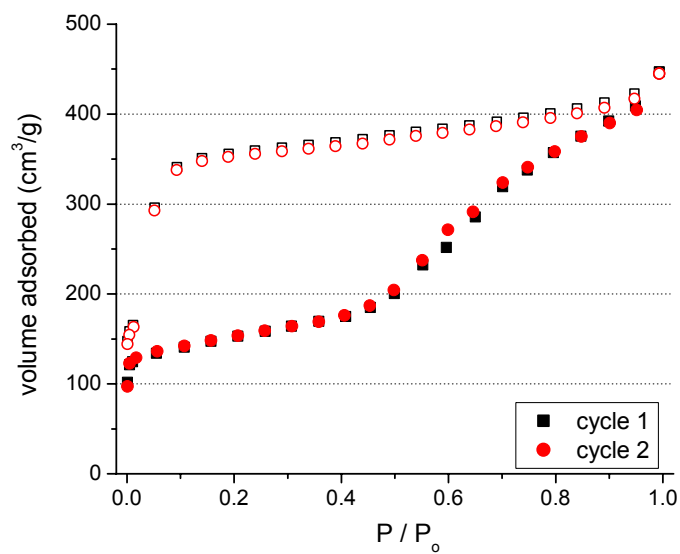
3.3.2 Nitrogen adsorption of **4** and **4**Li⁺

N₂ adsorption isotherms for **4** and **4**Li⁺ are presented in Figure 3.3. The nitrogen-accessible BET surface area and Dubinin-Radushkevich (DR) micropore volumes of the two samples are nearly identical (**4**: 802 m²/g, 0.30 cm³/g; **4**Li⁺: 756 m²/g, 0.34 cm³/g). But, the isotherm of **4**Li⁺ exhibits a large step at P/P₀ ~ 0.5 and the capacity at 1 atm is almost double that of **4**. Notably, the hysteresis behavior is repeatable, Figure 3.3. Moreover, the desorption curve has a distinct hysteresis loop that does not rejoin the adsorption curve until P/P₀ ~ 0.01. This particular type of hysteresis is generally not indicative of mesoporosity, but rather of dynamic framework behavior,^{4,14-17} e.g. shifting of interwoven frameworks with respect to each other. Here the introduction of lithium has apparently rendered the interpenetrated networks mobile in the solid state, particularly at high nitrogen loading, and therefore able to accommodate more guests. PXRD measurements confirm that any structural changes are reversed upon re-oxidation.

The unusual hysteresis observed in the N₂ 77K isotherm peaked interest in the potential of the N₂ heat of adsorption as compared to the neutral material. The calculation of the isosteric heat of adsorption requires the measurement of isotherms at the minimum two different temperatures. However, the N₂ 87K isotherm of **4**Li⁺ did *not* display similar hysteretic behavior and almost completely overlaid the 77K isotherm at low pressures, Figure 3.4. The hysteresis was observed again after the N₂/87K isotherm was performed, suggesting that this behavior is a result of specific N₂-Li⁺ interactions present only at 77K. It has not yet been possible, however, to monitor structural changes as a function of N₂ pressure and temperature which might clarify these interactions.



A



B

Figure 3.3 A) N_2 isotherms of **4** and **4Li⁺**. Closed symbols, adsorption; open symbols, desorption. B) N_2 isotherm cycling of **4Li⁺**.

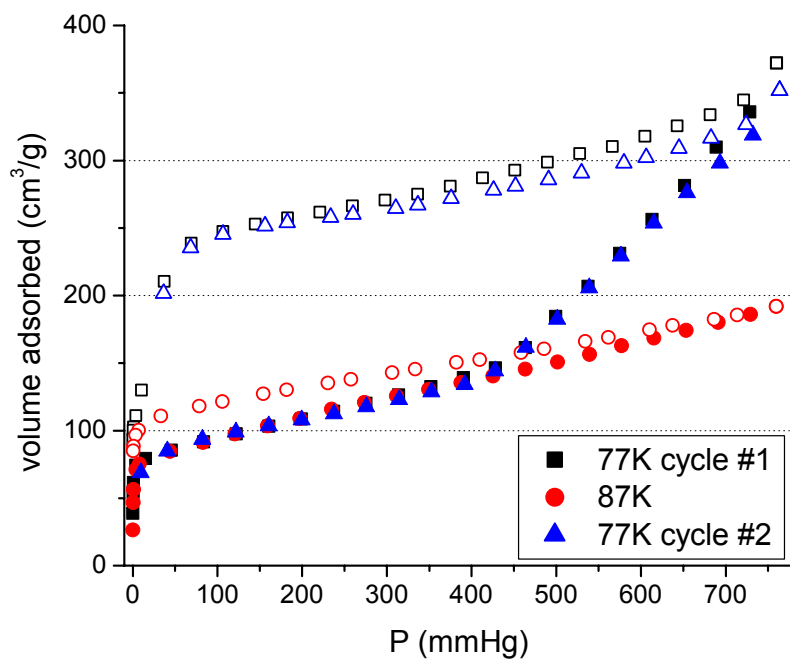
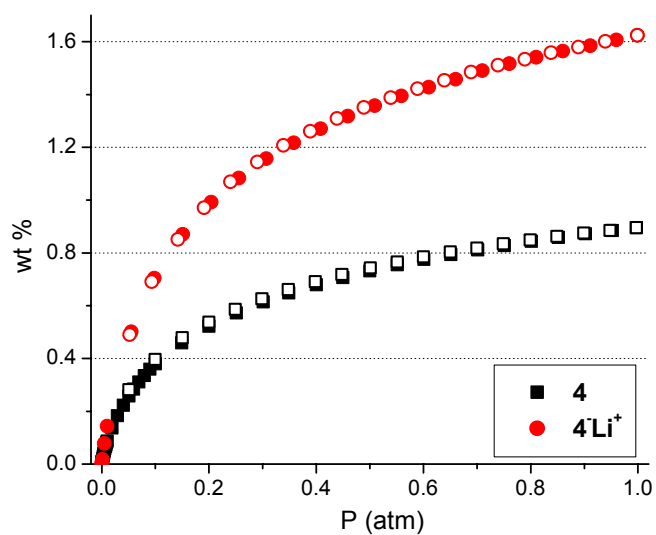


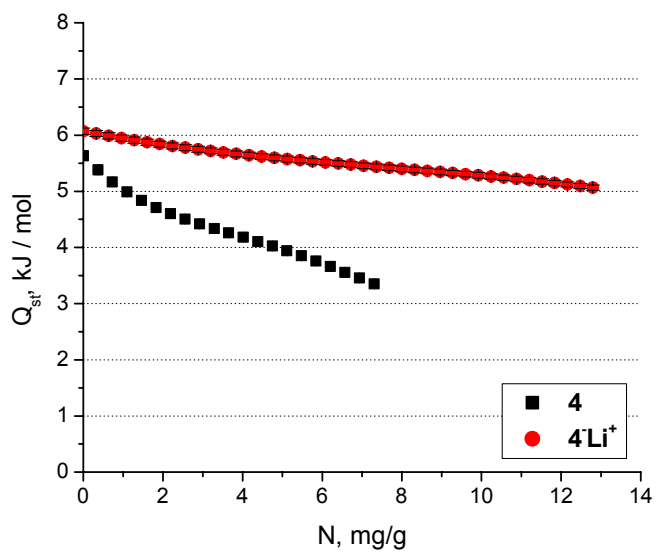
Figure 3.4 N₂ isotherms of 4-Li⁺ at 77K and 87K.

3.3.3 Hydrogen adsorption of **4** and **4Li⁺**

Remarkable enhancements are also seen for H₂ sorption, Figure 3.5. At 77K and 1 atm the H₂ capacity of **4** is 0.93wt%, but for **4Li⁺** it is nearly double, 1.63wt%. Additionally, the isosteric heat of adsorption, a measure of the interaction strength between H₂ and the adsorbent, is substantially greater for **4Li⁺** than **4** over the entire loading range, Figure 3.5. This is notable as the inclusion of unsaturated metal sites in MOFs is recognized as an approach to create stronger H₂ binding.^{18,19} Rather than introducing metal unsaturation through desolvation at the MOF nodes, framework reduction provides such sites in the form of cations that balance negative charge of the reduced ligands. At 1 atm, the enhancement in H₂ uptake is 60 H₂ molecules per added lithium cation. This cannot be explained solely by direct H₂/cation binding and instead points to other factors such as framework displacement (see Scheme 3.1) and/or enhanced strut polarizability.



A



B

Figure 3.5 A) H₂ adsorption isotherms of **4** and **4Li⁺** at 77K. B) Isosteric H₂ heat of adsorption of **4** and **4Li⁺**.

3.4 Conclusions

While comparatively high, the hydrogen uptake levels reported here do not meet the DOE targets or even match those reported for the very best existing MOFs. Nevertheless, chemical reduction represents a unique approach to enhancing sorption but the studies presented in this chapter leave substantial speculation concerning the mechanism of H₂ uptake enhancement. The curious behavior observed in the nitrogen isotherms of the reduced material lead us to hypothesize that H₂ uptake enhancement is not solely a result of specific and favorable cation/framework binding sites. While still speculative, a framework shift from an *interwoven* structure to an *interpenetrated* structure upon doping and adsorption would indeed increase accessible surface area and modify pore size to accommodate more adsorbate molecules, N₂ or H₂. With only one material and one cation (Li⁺) presented here, it is difficult to find a firm explanation. Chapter 4 continues the reduction and doping studies with the same framework material, but examines the other alkali metal cations (Na⁺, K⁺) at various doping levels to elucidate further the mechanisms by which framework reduction enhances gas uptake.

**Chapter 4. Alkali Metal Cation Effects in Hydrogen Uptake and Binding in Metal-Organic
Frameworks**

(previously published in Mulfort, K. L., Hupp, J. T., *Inorg. Chem.*, **2008**, *47*, 7936-7938.)

4. Chapter Overview

In Chapter 3 I introduced the framework reduction of a redox-active MOF using direct exposure to lithium metal. The reduced material, now doped with charge-balancing lithium cations, exhibited not only enhanced H₂ uptake but also much stronger binding than the original material. This is a noteworthy development, but the mechanism of enhanced H₂ binding in the reduced framework is somewhat ambiguous. Structural characterization by nitrogen adsorption suggests framework dynamicism, most likely occurring as the catenated frameworks shift with respect to each other upon doping and guest adsorbate loading. In this two-fold interwoven framework, it is difficult to distinguish between two factors that can impact H₂ uptake: 1) newly formed charge(cation/reduced strut) -quadrupole(H₂) interactions in the reduced material, and 2) changes in surface area and pore size that can accommodate more H₂ guest molecules.

Chapter 4 expands upon the studies introduced in Chapter 3 to vary the cation size (from Li⁺ to Na⁺ and K⁺) as well as the doping level to probe the H₂ uptake mechanism. The same MOF structure is employed here since this structure is robust, permanently porous, and its redox activity has been well established. Nitrogen adsorption measurements will be used to monitor structural features after doping and correlate H₂ uptake with surface area and pore size. The parallel structure-function measurements will allow us to begin to understand how H₂ interacts with a very complex framework material.

4.1 Introduction

The deployment of hydrogen as a carbon-free fuel source is dependent on its safe and efficient production, transport, and storage.¹ Molecular physisorption of hydrogen is a potentially attractive approach to storage as uptake and discharge are likely to be much faster than in

materials that dissociatively store hydrogen. Permanently microporous metal-organic frameworks (MOFs) are being explored as H₂ storage materials, in part because pore size & shape as well as pore-wall chemical composition are readily tuned by choice of organic strut.² Additionally, the high surface areas, high micropore volumes, and low densities of MOFs suggest that molecular hydrogen should be storable at high density; notably, 7.5wt% H₂ uptake was recently demonstrated in MOF-177 – albeit at 77K.^{3,4} Extending the performance to ambient temperature will require substantial improvement in the H₂ heat of adsorption.⁵ The predicted average H₂ heat of adsorption necessary for effective ambient temperature storage and release, circa 15 kJ/mol,^{6,7} is still well beyond the highest reported values.

Much of our effort to understand and enhance H₂ uptake in MOFs has been aimed at amplification of heats of adsorption through framework reduction and concomitant cation doping, see Chapter 3.⁸ Here we describe the dopant-cation dependence of H₂ uptake and binding in a two-fold interwoven MOF, Zn₂(NDC)₂(diPyNI), designated **4** (see Chapters 2 and 3).⁹ From previous work with this material, we hypothesized that variation of the extra-framework cation could differentially affect H₂ uptake by two complementary mechanisms: the introduction of strong H₂ binding sites (sites for charge(cation)-quadrupole(H₂) interaction^{10,11}) and cation-induced shifts in the interwoven networks.

4.2 Experimental

4.2.1 Methods

All commercial reagents were of ACS grade and purchased from Sigma-Aldrich unless otherwise noted. Tetrahydrofuran (THF) was purified using a two-column solid-state purification system (Glasscontour System, Jeorg Meyer, Irvine, CA). Stir bars used for

preparation of the reductant solution were coated in pyrex glass. ICP was used to analyze for **M** (Li at 610.365 nm, Na at 589.592 nm, K at 766.491 nm) and Zn (202.548 nm) content as compared to standardized solutions. ^1H NMR (500 MHz) was performed on **4·M** samples after adsorption measurements (completely evacuated) dissolved in a 9:1 mixture of D_2SO_4 (96-98 wt% in D_2O , 99.5 atom% D) to DMSO-d_6 (99.9 atom% D).

4.2.2 Framework reduction

Reductant solutions of the three metal-naphthalenides (M(NAP)) were prepared by adding an equimolar amount of alkali metal (Li^0 , Na^0 , K^0) to a 0.1M solution of naphthalene in tetrahydrofuran (THF) following literature precedent.¹² **CAUTION:** *alkali metals are extremely reactive with water and potentially reactive with nitrogen! All manipulations with alkali metals were carried out in an argon atmosphere glove box. Alkali metals are stored in mineral oil in a glove box.* All reduced materials were prepared in the same manner; a general procedure follows. Immediately prior to use, small pieces of the metal are briefly immersed in THF to remove excess mineral oil. The pieces are dried and any dark oxide on the surface is removed to reveal the shiny metallic surface. Immediately upon addition of the cleaned metal pieces to the naphthalene solution, a green color appears in solution. After stirring for several hours, the metal chunks are completely dissolved and the solution is uniformly dark green. A precise quantity of 0.1M M(NAP) is then transferred to a known amount of MOF sample with a volumetric syringe and manually agitated for several minutes. The solution immediately turns clear colorless which is accompanied by a color change in the solid. The solid MOF is then isolated on a coarse glass frit and washed with 1 ml aliquots of THF to remove any weakly adsorbed naphthalene. Structure **4** reduced with M(NAP) is designated **4·M** where $\text{M} = \text{Li}, \text{Na}$ or K . These reduced MOFs are air-sensitive and oxidation can be observed as the solid changes back to the original

color upon exposure to air. Therefore, all manipulations with the reduced material are carried out under inert atmosphere. Metal content is determined by ICP analysis and EA. **4·Li_{0.06}**

(4·Li): Anal. calcd. for **4·Li**, C₄₈H₂₄N₄O₁₂Zn₂Li_{0.06}·2H₂O: C, 56.75; H, 2.78; N, 5.51. Found:

C, 56.80; H, 2.67; N, 5.64. **4·Na_{0.10} (4·Na):** Anal. calcd. for **4·Na**, C₄₈H₂₄N₄O₁₂Zn₂Na_{0.10}·3H₂O:

C, 55.66; H, 2.92; N, 5.41. Found: C, 55.53; H, 3.15; N, 5.48. **4·K_{0.06}(4·K):** Anal. calcd. for

4·K, C₄₈H₂₄N₄O₁₂Zn₂K_{0.06}·3H₂O: C, 55.56; H, 2.92; N, 5.41. Found: C, 55.79; H, 2.60; N,

5.52. **4·K_{0.26} (4·K'):** Anal. calcd. for **4·K'**, C₄₈H₂₄N₄O₁₂Zn₂K_{0.24}·3H₂O: C, 55.28; H, 2.90; N,

5.27. Found: C, 55.08; H, 2.84; N, 5.27. **4·K_{0.84} (4·K''):** Anal. calcd. for **4·K''**,

C₄₈H₂₄N₄O₁₂Zn₂K_{0.84}·4H₂O: C, 53.16; H, 2.97; N, 5.17. Found: C, 52.84; H, 2.64; N, 5.38.

4.2.3 Adsorption measurements

See Sections 2.2.5 and 2.2.6 for details. Samples of **4·M** are air sensitive and were loaded into sample tubes under inert atmosphere. N₂ adsorption isotherms were measured at 77K and H₂ adsorption isotherms were measured at both 77K and 87K in order to calculate the isosteric heat of adsorption.

4.3 Results and discussion

4.3.1 Framework reduction

Previously we have engendered framework reduction through direct contact of the MOF with solid lithium metal.⁸ Since here we are interested in changing the cation and monitoring structure and adsorption performance, we chose to use the well-understood metal-naphthalenide reductants, M(NAP), where M = Li, Na, or K.¹² Conveniently, the naphthalenide anion is intensely green in solution. When added to **4**, the solution turns colorless, while **4** itself changes from yellow to deep green/brown, consistent with electron transfer from the naphthalenide

radical anion to the diPyNI struts of **4**. Framework reduction is reversible: upon exposure to oxygen (air), the reduced solid returns to its original color. The reduced and doped frameworks are designated **4·M**, where **M** is Li^+ , Na^+ , or K^+ .

4.3.2 Hydrogen adsorption of **4** and **4·M**

The H_2 uptake and binding as well as structural features of the framework materials were probed by low-pressure H_2 and N_2 adsorption measurements. As we anticipated, there is a considerable increase in H_2 uptake by the reduced materials in comparison to the neutral MOF, Table 4.1. Low-pressure H_2 isotherms for all three **4·M** are shown in Figure 4.1. At 77K and 1 atm, H_2 uptake increases with dopant cation size, reaching 1.54 wt% for **4·K** – a remarkable 65% (relative) increase over uptake by pure **4**.

To gain insight into the mechanism of H_2 uptake enhancement, we measured isosteric heats of H_2 adsorption, Q_{st} .¹³ As shown in Figure 4.2, upon reduction and doping of **4** we observed significant increases in Q_{st} over the entire H_2 loading range. Furthermore, for all three **4·M** materials the fall-off of Q_{st} with H_2 loading is shallower than that for **4**.

The ordering of average Q_{st} values, **4·Li** > **4·Na** > **4·K** > **4**, follows the cation charge-to-radius ratio, suggesting that the observed dopant-induced enhancements in heats of adsorption emanate from charge(cation)-quadrupole(H_2) interactions. Two observations, however, argue against this explanation. First, the number of extra hydrogen molecules adsorbed (at 1 atm) per dopant cation, greatly exceed the number capable of interacting directly with even a fully isolated cation (Table 4.1). Secondly, the enhancements in Q_{st} for **4·M** are much smaller than those obtained computationally for cation-doping of solely carbon-based materials^{14,15} or, more recently, MOFs.¹⁶⁻¹⁹

Additionally arguing against a dominant role for dopants as special sorption sites are the results of experiments in which the extent of doping was varied. Remarkably, as shown in Figure 4.3 and Table 4.1, increasing the amount of dopant *decreases* hydrogen uptake, ultimately to less than that for undoped **4**. Heats of adsorption, on the other hand, are nearly identical for differentially doped samples. Table 4.1 further summarizes results for **4** doped with varying amounts of K^+ (6, 26, and 84%; **4•K**, **4•K'**, and **4•K''**, respectively; other cations were not investigated).

Table 4.1 Summary of N₂ and H₂ low-pressure and temperature measurements of **4** and **4·M**.

	M / diPyNI	BET surface area (m ² /g) ^[a]	DR micropore volume (cm ³ /g) ^[b]	H ₂ wt% (1 atm, 77K)	Q _{st} range (kJ/mol)	average Q _{st} (kJ/mol)	additional H ₂ /M ⁺ at P(H ₂) = 1 atm
4	0.00	802	0.30	0.93	5.6 - 3.4	4.31 ± 0.61	n.a.
4·Li	0.06	676	0.34	1.23	6.3 - 5.6	5.96 ± 0.18	24
4·Na	0.10	837	0.33	1.45	5.6 - 4.5	4.99 ± 0.31	25
4·K	0.06	988	0.39	1.54	6.0 - 3.3	4.51 ± 0.72	49
4·K'	0.26	813	0.32	1.42	5.6 - 3.7	4.46 ± 0.47	9
4·K''	0.84	382	0.15	0.75	5.1 - 4.0	4.45 ± 0.32	(1)

[a] BET surface area determined from N₂ adsorption isotherm in between $0.007 < P / P_0 < 0.05$. [b] DR micropore volume calculated at $P / P_0 < 0.01$.

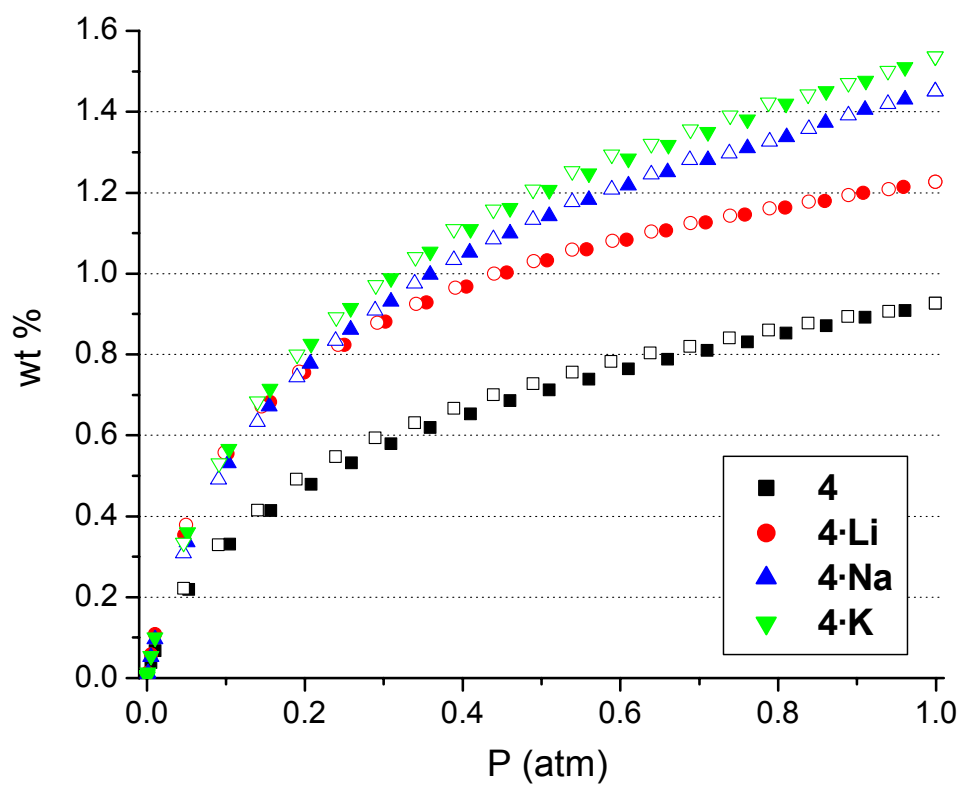


Figure 4.1 77K H₂ isotherms for **4** and **4-M**. Closed symbols, adsorption; open symbols, desorption.

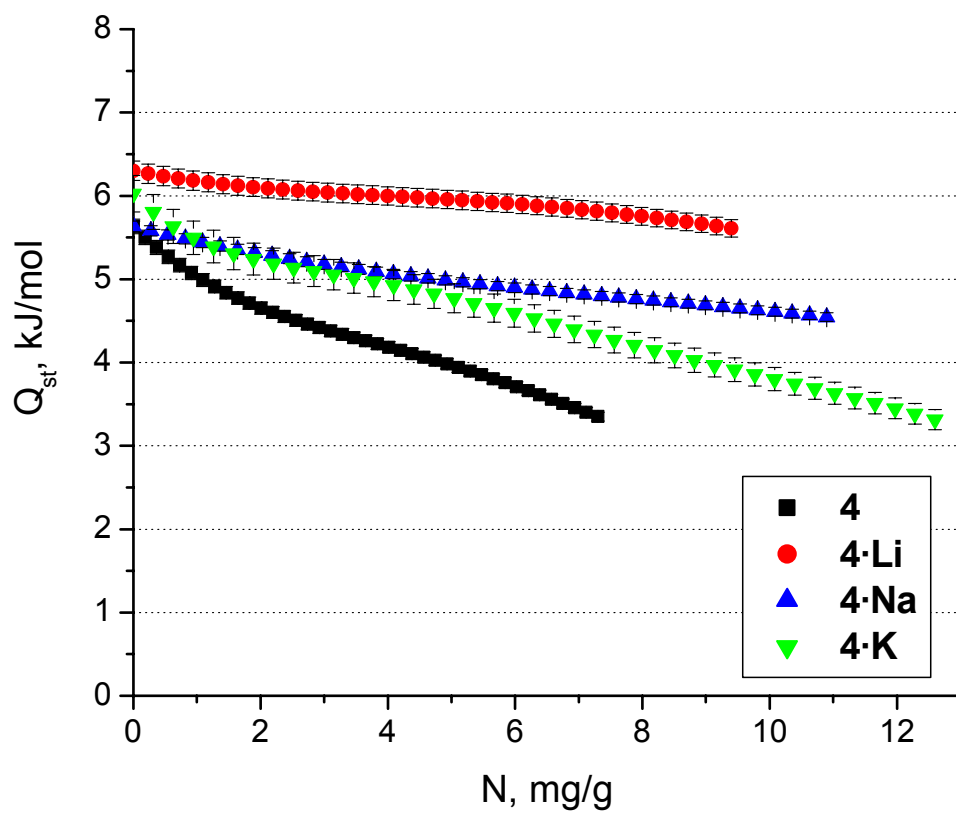


Figure 4.2 Isosteric H_2 heat of adsorption for **4** and **4·M**.

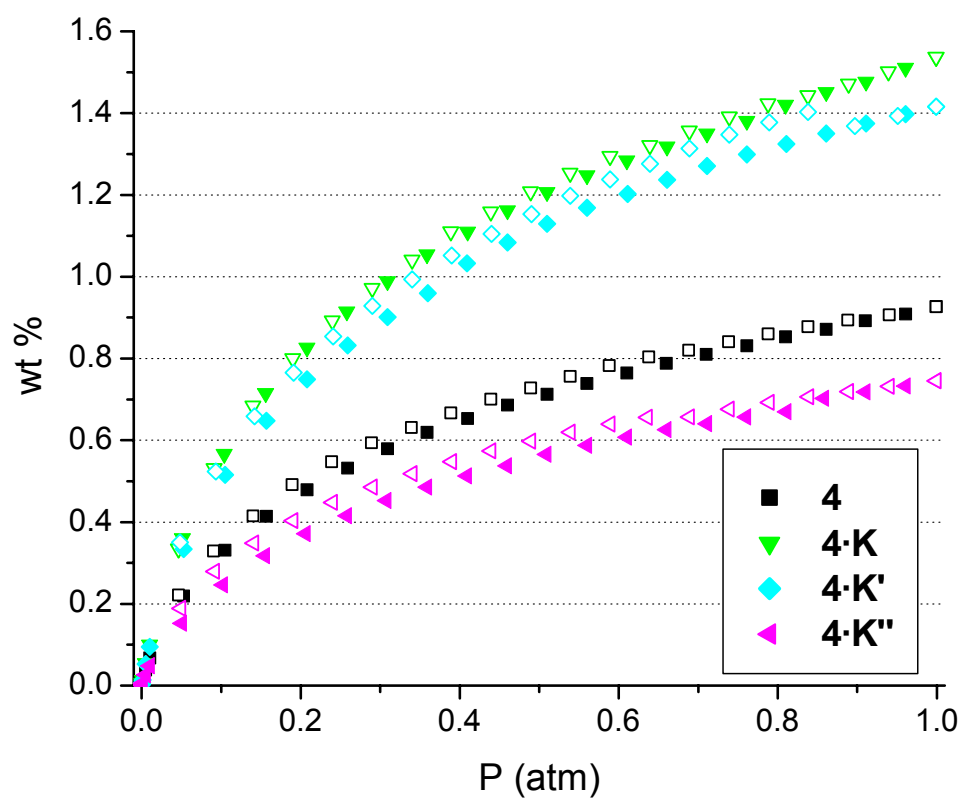


Figure 4.3 77K H₂ isotherms for 4·K materials.

4.3.3 Nitrogen adsorption of **4** and **4·M**

Nitrogen adsorption isotherms were performed to monitor structural changes upon framework reduction and doping. All isotherms (Figure 4.4) display very strong uptake at low pressures, and Type I behavior, indicative of microporosity. At higher pressures, however, the **4·M** isotherms exhibit stepwise adsorption and hysteresis. Furthermore, the hysteresis is repeated on subsequent adsorption/desorption cycles. We hypothesize that this unusual behavior arises from adsorbate-driven displacement of interwoven networks^{8,20,21} (and increase of surface area), facilitated by framework reduction and metal ion doping.

The nitrogen accessible BET (Brunauer, Emmett, Teller) surface area is observed to vary substantially as a function of both dopant identity and dopant loading, Table 4.1. Figure 4.5 shows that **4·M** surface areas correlate strongly with H₂ wt% uptake at 1 atm. Additionally there exists a fair correlation between wt% uptake and micropore volume. In their computational studies, Frost and Snurr²² have emphasized that at intermediate loading, H₂ uptake should correlate well with surface area, while at higher loading (not achieved here) uptake should correlate with micropore volume.

We suggest that the surface area variations, at low dopant levels, are largely a consequence of framework/framework displacements (recall that **4** and **4·M** are catenated materials). The striking decreases in surface area at higher doping levels suggest that the dopant itself (K⁺) may ultimately block pores and prevent access to portions of the MOF, especially if the dopant ions retain solvent molecules. In addition to pore blocking, we also considered the possibility that cation solvation is responsible for the decrease in H₂ uptake with higher loading levels. To estimate the solvent content remaining in the reduced structure after evacuation, we used ¹H NMR to calculate the relative solvent content of the dissolved **4·K** materials. Samples were

dissolved in 9:1 D₂SO₄:DMSO-d₆ and the relative concentration of ligands to solvent molecules was calculated by integrating their respective peak intensities. As a starting point, as-synthesized **4** was dissolved in D₂SO₄ and the DMF proton peaks were compared with the ligand peaks. The solvent content in as-synthesized **4** measured by NMR gave very good agreement with the crystal structure: 6.2 DMF per Zn(II) dimer by NMR, 6.5 DMF per Zn(II) dimer by crystallography (Figure 4.6, Table 4.2). The concentration of DMF and THF in each K(NAP)-THF reduced sample (**4**·K, **4**·K', **4**·K'') was much less than the actual loading amount. Therefore, we can rule out cation solvation by DMF or THF as a major contributor to the adsorption performance of the reduced materials. Additionally, DMSO-d₆ was used as a co-solvent in order to detect any residual naphthalene remaining in the pores; none was detected in any of the materials.

Returning to Figure 4.5, differences in surface area appear to account well for the differences in H₂ uptake by the various **4**·M species, but not for the differences between **4** and **4**·M; the data point for uptake for pure **4** falls considerably below the best-fit line. Table 4.1 indicates that differences in heats of adsorption are insufficient to explain the disparity. We suggest, following our earlier report⁸ (and the discussion above of hysteretic N₂ isotherms), that an additional consequence of framework doping and reduction is molecular-adsorbate-driven displacement of interwoven networks. In other words, gas adsorption itself brings about further framework displacement and increases in surface area. For N₂, the increase appears to occur only at P/P₀ values above ~0.2 to 0.5 (depending on identity of the dopant cation). Notably, these pressures are well above those used for BET fits – meaning that the BET analysis is blind to the putative “extra” surface area. In any case, the extra area may account for the additional H₂ uptake by **4**·M materials at 1 atm. In principle, variable pressure, cryogenic PXRD or single-crystal x-ray

structural measurements could shed light on this explanation. Unfortunately, we lack this experimental capability at present.

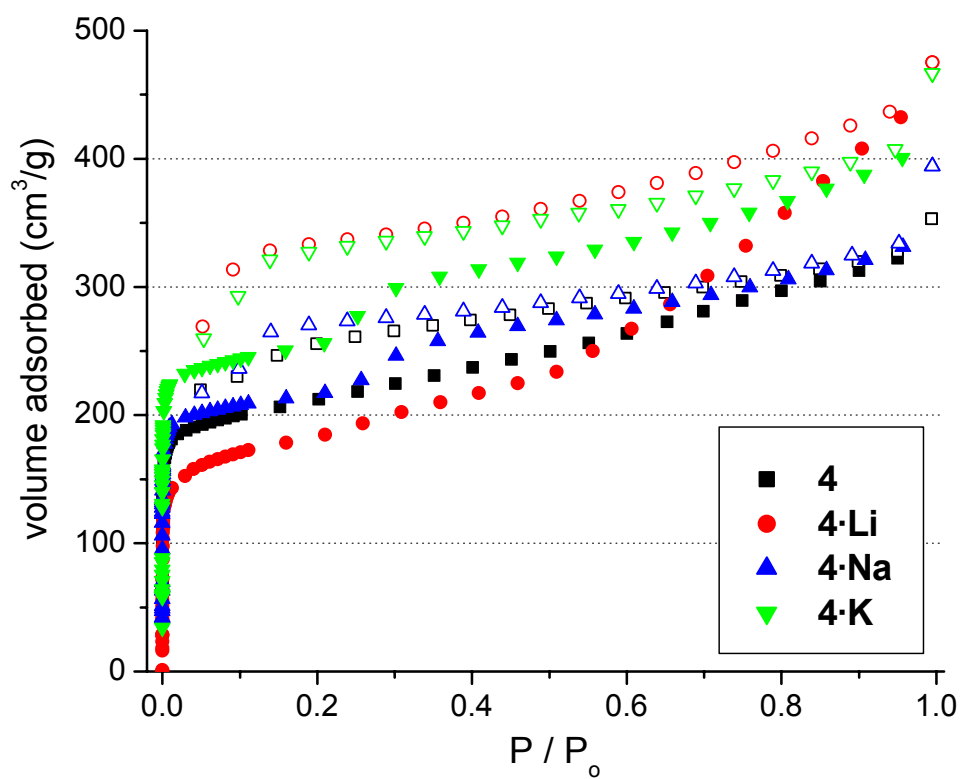


Figure 4.4 N_2 isotherms for **4** and **4-M**. Closed symbols, adsorption; open symbols, desorption.

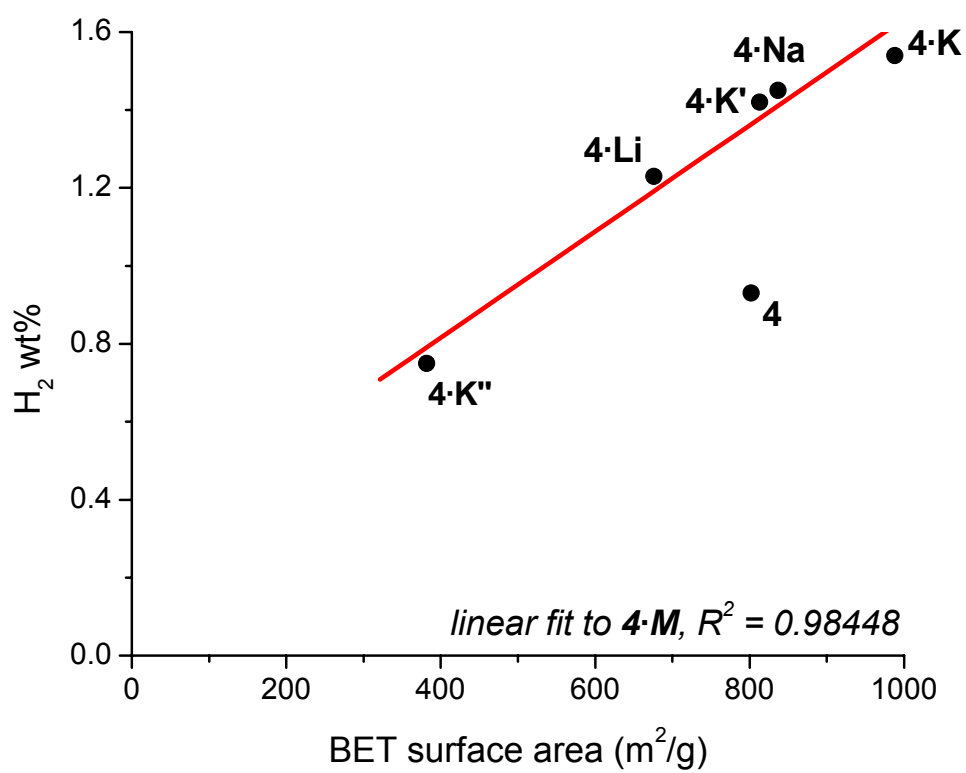


Figure 4.5 H₂ uptake at 1atm plotted against BET surface area. Data for **4** is omitted in linear fit.

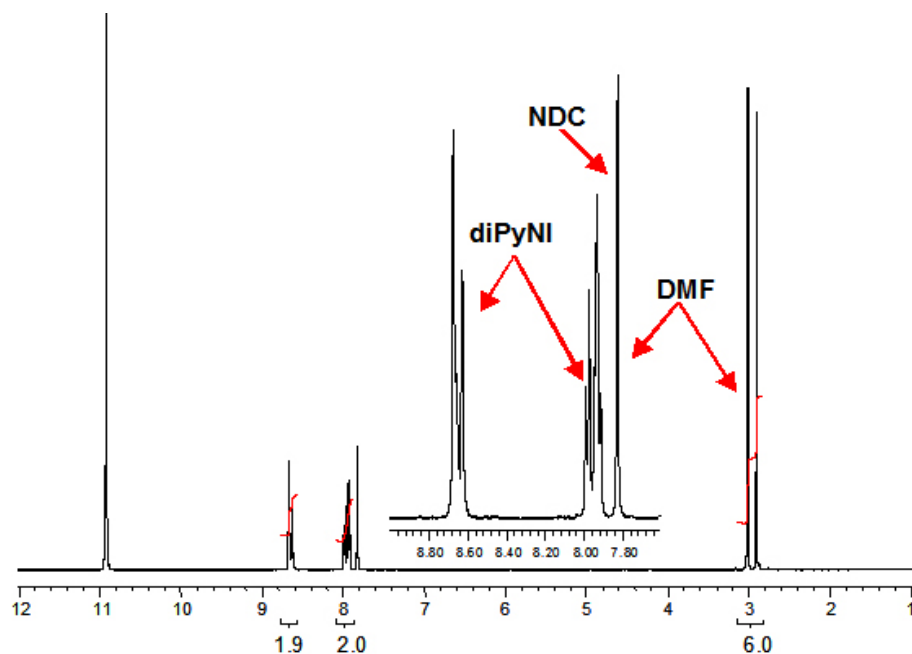


Figure 4.6 500 MHz ^1H NMR of dissolved **4** in D_2SO_4 .

Table 4.2 Quantification of residual solvent in **4·K** materials by ^1H NMR.

Material	M / Zn (II) dimer ^[a]	DMF / Zn(II) dimer ^[b]	mass loss (%)	DMF / M^+
4	0.00	6.2	46	n.a.
4·K	0.06	0.01	0.11	0.25
4·K'	0.26	0.002	0.012	0.01
4·K''	0.84	0.24	1.8	0.28

[a] Measured by ICP analysis. [b] Calculated by integration of NMR peaks, ratio of DMF protons to ligand protons.

4.4 Conclusions

To summarize, framework reduction and alkali metal cation doping significantly enhance hydrogen uptake, while modestly enhancing binding. For **4·M**, the mechanism appears not to be the creation of special metal-based adsorption sites, as demonstrated previously at MOF corner sites,²³⁻²⁶ but instead entails favorable displacement of interwoven frameworks. The absence of large special-site effects, especially with Li^+ as dopant, suggests that ions may be positioned *between* frameworks¹⁸ and thus, not readily accessible to H_2 .

The strong special-site H_2 binding effects we expected in these experiments, but did not observe, should be apparent in two cases: 1) framework reduction and doping in non-catenated structures, and 2) framework reduction and doping with divalent cations. In non-catenated frameworks, dopant cations cannot be shielded by pairs of frameworks which inhibits direct cation- H_2 interactions. Additionally, non-catenated frameworks are less likely to exhibit dramatic structural changes upon reduction and cation doping. Framework doping with divalent cations such as Mg^{2+} and Ca^{2+} would impart much stronger interactions with H_2 , attributable to their greater charge-to-mass ratio than their alkali-metal counterparts. In site-specific binding measurements, Mg^{2+} - H_2 binding energies of ~ 17 kJ/mol have been directly observed.²⁷ Binding sites of this magnitude would be immediately apparent.

Framework reduction and cation doping by the alkali metals is generalized in Chapter 5 by employing another, *triply*-interwoven MOF structure. The structural effects of doping will be compared to the binding energies and overall hydrogen uptake. These studies provide further motivation for the goals of pursuing non-catenated frameworks and the divalent cation dopants.

Chapter 5. Framework Reduction and Alkali-Metal Doping of a Triply Catenating Metal-Organic Framework Enhances and then Diminishes H₂ Uptake

(submitted in part for publication to *Langmuir*)

5. Chapter Overview

Chapters 3 and 4 outlined the framework reduction and subsequent H₂ adsorption properties of a redox-active, two-fold interwoven Zn(II) paddlewheel MOF. These studies have demonstrated the plausibility of framework reduction and doping as a method to enhance H₂ uptake, but the primary mechanism of enhancement does not appear to be additional dopant-H₂ binding. Instead, structural changes accompanying framework reduction and doping most likely have the greatest impact on H₂ uptake. In this Chapter I will describe the framework reduction and doping of another catenated paddlewheel structure with the alkali-metal cations. Unlike the material examined in previous chapters, this structure is three-fold interwoven. In these studies, N₂ adsorption measurements are used to quantify the structural characteristics of the reduced materials. Also, solid-state EPR spectroscopy was used for the first time to observe radical formation in the doped materials. In this reduced structure, we do also observe H₂ uptake enhancement. However, there is very little, if any, increase in the H₂ binding energy as compared to the neutral material. In this case, the three interweaving frameworks are almost certainly shielding the cations to completely prevent direct dopant-cation interactions. The concurrent N₂ adsorption measurements suggest that structural changes upon doping, most likely in the form of shifting frameworks, are indeed the largest factor in H₂ uptake enhancement.

5.1 Introduction

Permanently microporous, crystalline, metal-organic framework materials (MOFs) are being considered for a wide range of chemical applications that can capitalize on their high internal surface areas, uniform pore sizes, and enormous potential diversity in composition and structure.¹⁻³ Among the most intriguing is hydrogen gas storage.⁴⁻⁶ MOFs have the capacity to

revolutionize gas storage methods and materials because of their ultra-low densities, and their crystalline micropore and/or ultra-micropore structures; in principle, these structures can promote ordered and therefore exceptionally high density guest packing. There have been several recent reports of large H₂ uptake in MOFs at 77K and high pressure,^{7,8} but none yet satisfy proposed capacity benchmarks for commercially viable and safe hydrogen storage at non-cryogenic temperatures. While there is an immediate need to improve H₂ sorption, equally important for long-term success is the need to understand fully the factors that affect H₂ uptake and binding such that the essentially limitless potential variety of MOF materials can be taken to full advantage.

Improving MOF H₂ adsorption capacity through structural means has been pursued by two general strategies. The first is to manipulate the MOF structure to increase H₂-framework dispersion interactions and decrease unused pore space, either by adjusting ligand length and shape^{9,10} or through framework catenation.¹¹ Because H₂ contains only two electrons, these dispersion interactions are relatively weak. Furthermore, they diminish with $1/r^6$ where r is the distance between H₂ and the framework. Under the storage temperatures and pressures envisioned for vehicular applications, H₂ is well above its critical point. Significant sorption excesses, therefore, can be achieved only by framework adsorption – and not by pore condensation. Thus, there is no incentive to create huge pores, i.e. pores that can accommodate more than a monolayer of H₂ molecules. The second approach attempts to create exceptionally attractive surface sites within the MOF via formation of unsaturated metal centers – typically through removal of coordinated solvent molecules at nodes (metal ions or clusters comprising framework structural sites).¹²⁻¹⁵ Neutron scattering experiments have verified that H₂ binds at these sites first, most likely through Kubas-type interactions. While this approach has been

shown to impact H₂ uptake within MOFs appreciably, it is sometimes difficult to synthesize frameworks that can resist collapse upon complete desolvation of metal sites. A further challenge is to introduce enough such sites to make a practical difference under high-loading conditions.

Chapters 3¹⁶ and 4¹⁷ describe the results for a distinct, but related, third approach: chemical reduction of framework struts. For a representative doubly-interpenetrating MOF, we observed a 75% increase in H₂ uptake at 77K and 1 atm (0.93 wt% → 1.63 wt. %) as well as significant increases in loading-dependent heats of adsorption, following partial reduction with lithium metal.¹⁶ We suggested that framework reduction could potentially enhance the uptake of H₂ by MOFs by at least three mechanisms: i) greatly enhanced strut polarizability, potentially resulting in stronger induced-dipole/induced-dipole interactions between the strut and H₂ (i.e. $1/r^6$ interactions); ii) the introduction of essentially completely unsaturated metal centers in the form of charge-compensating cations (potential sites for charge/quadrupole interactions with dihydrogen, or Kubas interactions if transition-metal ions are used); and/or iii) displacement of interwoven networks to create pores and channels of more optimal size for H₂ sorption. Based on several lines of evidence, including an unusual and highly hysteretic N₂ isotherm, we concluded that (at least) mechanism *iii* was important for the particular system examined. We were unable to draw conclusions about the significance of mechanism *ii*, in part because of ambiguity about the degree of residual solvation of the dopant metal ions and, in part, because only a single dopant (Li⁺) was examined. In a follow-up study pursued in parallel with the present study (described in Chapter 4¹⁷) we concluded that mechanism *ii* was likely not operative for the doubly-interpenetrating system. The follow-up work entailed extension of the investigation to Na⁺ and K⁺ as dopants.

Here we elaborate further on the idea of chemical reduction of organic struts as a strategy for enhancing H₂ uptake by metal-organic framework compounds. As in Chapters 3 and 4, we employ a mixed-strut material featuring a pillared-paddlewheel structure. MOFs of this kind consist of metal pairs (generally Zn(II) or Cu(II)) bridged by linear dicarboxylates which create paddlewheel sheets in two dimensions. The sheets are pillared in a third direction by linear dipyridyls to give the overall formula M₂(dicarboxylate)₂(dipyridyl).¹⁸ We have found the motif particularly useful for creating anisotropic channel structures and for introducing catalytic¹⁹ and/or redox-active ligands. Furthermore, in contrast to many MOF materials based solely on dipyridyl struts, pillared-paddlewheels typically retain crystallinity and microporosity upon removal of solvent.

In our experience, most pillared-paddlewheel materials, including the MOF previously subjected to framework reduction, are comprised of doubly-interwoven structures. Here we report the behavior of the solvent-evacuated form of a triply-interwoven compound: Zn₂(NDC)₂(diPyTz)·nDMF (**9·nDMF**) (NDC = 2,6-naphthalenedicarboxylate, diPyTz = di-3,6-(4-pyridyl)-1,2,4,5-tetrazine) (Figure 5.1). We have subjected the material to reduction and doping with three alkali-metal cations Li⁺, Na⁺, and K⁺. We reasoned that charge/quadrupole interactions, for example, could be systematically modulated as these depend on ion size. We find that reduction and doping, even at low levels, increases the low pressure (1 atm), cryogenic (77K) uptake of H₂ by (solvent-evacuated) **9** by as much as 43%.

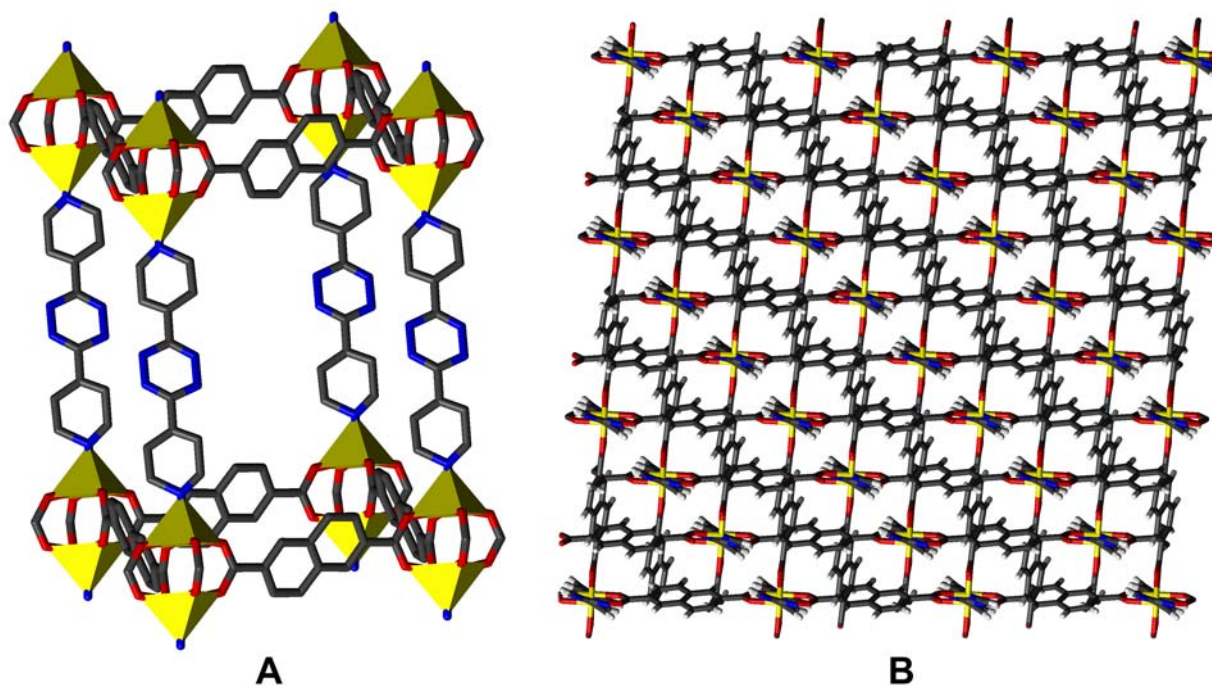


Figure 5.1 A) Single crystal structure of **9**. For clarity, disordered solvent molecules, hydrogens, and two levels of interpenetration are omitted. The yellow polyhedra represent the zinc ions; C, gray; N, blue; O, red. B) Packing diagram of **9**.

5.2 Experimental

5.2.1 General methods

General methods and materials can be found in Chapter 4.2.1.

5.2.2 Framework reduction

Framework reduction by M(NAP)-THF procedures can be found in Chapter 4.2.2. Structure **9** reduced with M(NAP) is designated **9·M** where M = Li, Na or K. These reduced MOFs are air-sensitive and oxidation can be observed as the solid changes back to the original color upon exposure to air. Therefore, all manipulations with the reduced material are carried out under inert atmosphere. Metal content is determined by ICP analysis and EA. The structure of **9** is maintained through reduction and oxidation by air as verified by PXRD and TGA. **9·Li_{0.10}** (**9·Li**): Anal. calcd. for **9·Li**, C₃₆H₂₂N₆O₉Zn₂Li_{0.10}: C, 53.11; H, 2.72; N, 10.32. Found: C, 53.38; H, 2.64; N, 10.06. **9·Na_{0.24}** (**9·Na**): Anal. calcd. for **9·Na**, C₃₆H₂₄N₆O₁₀Zn₂Na_{0.24}: C, 51.66; H, 2.89; N, 10.04. Found: C, 51.84; H, 2.63; N, 9.79. **9·K_{0.14}** (**9·K**): Anal. calcd. for **9·K**, C₃₆H₂₄N₆O₁₀Zn₂K_{0.14}: C, 51.67; H, 2.89; N, 10.26. Found: C, 50.39; H, 2.34; N, 9.55.

5.2.3 Adsorption measurements

Adsorption procedures can be found in Chapter 4.2.3. Samples of **9·M** are air sensitive and were loaded into sample tubes under inert atmosphere. N₂ adsorption isotherms were measured at 77K and H₂ adsorption isotherms were measured at both 77K and 87K in order to calculate the isosteric heat of adsorption.

5.2.4 EPR measurements

EPR measurements and analyses were performed by Thea M. Wilson. Samples were prepared in an argon atmosphere glovebox by loading the crystalline powder into quartz capillary tubes (0.84 mm OD, 0.6 mm ID) which were then inserted into larger quartz tubes for

easier handling and sealing. The tubes were sealed with a plug of vacuum grease and wrapped tightly with parafilm. Continuous wave (CW) EPR measurements were made using a Bruker Elexsys E580 X-Band EPR spectrometer outfitted with a variable Q dielectric resonator (ER-4118X-MD5-W1). All measurements were made at room temperature (~ 295 K) with a microwave power of 2 mW and a frequency modulation depth of 100 KHz.

5.3 Results and discussion

5.3.1 Structure of **9**

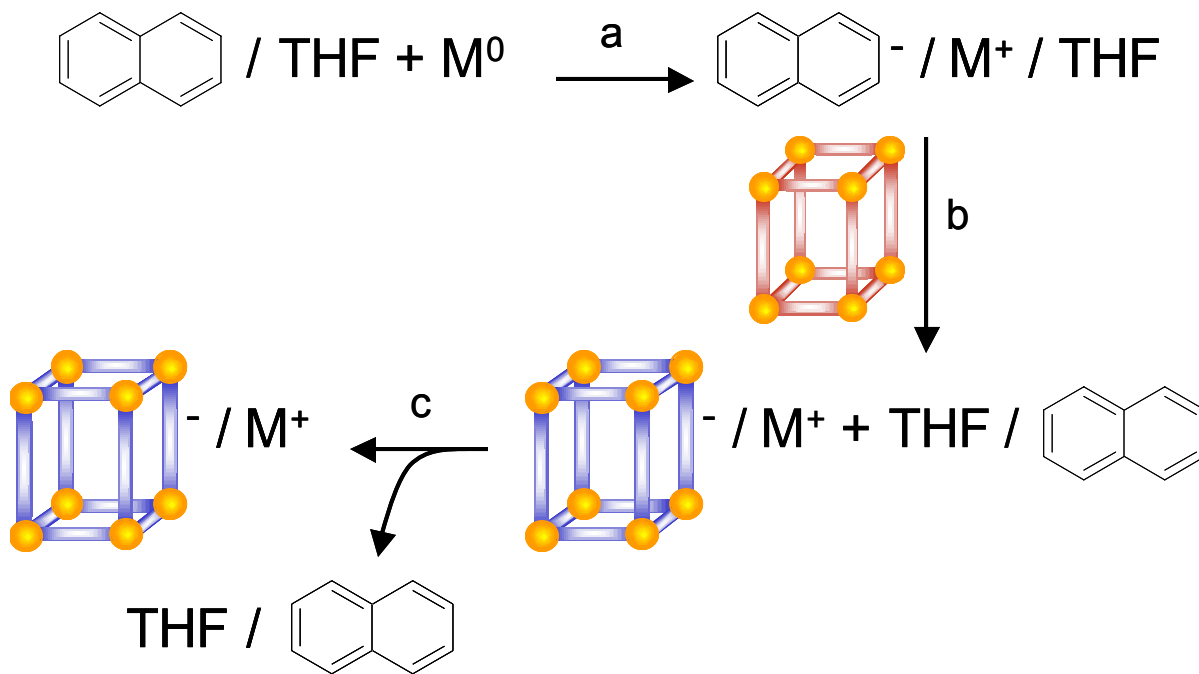
Macroscopic crystals of **9**•nDMF, obtained from static heating of the individual components in DMF (see section 2.2.3 and Table 2.1), were structurally characterized by single-crystal X-ray diffraction. The connectivity of one network of **9** is shown in Figure 5.1. Like other paddlewheel MOFs, it exhibits pillared square-grid network topology. The structure features three-fold interpenetration (Figure 5.1), but still displays 27% solvent-accessible void volume.²⁰

5.3.2 Framework reduction

The ligand, diPyTz, was chosen as a framework strut because of its well-defined redox activity.²¹ In related discrete coordination compounds, the ligand exhibits reversible one-electron reductions at -1.81 V and -2.50 V vs. ferrocene^{+/0}. Framework permeating, metal-naphthalenide species (M(NAP)) were employed for doping and reduction. M(NAP) species are powerful reductants ($E^{\circ} = -3.10$ V vs. Fc/Fc⁺ in THF) but otherwise are chemically innocent.²² The naphthalenide anion containing solution is intensely green. When added to the solid MOF, the solution turns clear/colorless as the naphthalenide radical anion transfers an electron to the dipyridyl ligand within the MOF, see Scheme 5.1 and Figure 5.2. The resulting cation-doped MOF (designated **9**•**M**, where **M** is Li⁺, Na⁺, or K⁺) is easily separated from the reductant

solution via filtration. PXRD revealed that the framework retains crystallinity upon reduction, Figure 5.3. While small changes to the PXRD pattern are evident following reduction and doping, we are unable to translate these into specific structural changes.

The degree of reduction, and concurrent metal loading, is controlled by the amount of reductant solution added to the solid MOF. We find that improved adsorption performance for these materials is obtained at doping levels that are much lower than 1 cation per dipyriddy ligand; the greatest enhancements are found for $M/Zn \sim 0.10$ (Table 5.1). The dipyriddy strut of **9** is thermodynamically much easier to reduce than the dicarboxylate strut (NDC). Since sub-stoichiometric amounts of reductant are used, we assume that only the diPyTz strut is reduced. Solid-state room temperature CW-EPR measurements on **9·Li** indicated the presence of radical species within the framework, but the fine structure could not be resolved sufficiently to characterize further the nature of the reduction site, see Figure 5.3. There have been three recent reports on cation(metal)-exchange within MOF materials and the roles various metal centers play in H_2 uptake and binding,²³⁻²⁵ but, as far as we are aware, experimental studies of ligand-centered redox behavior/doping within a MOF material are limited to the current investigation and our recent studies of a doubly-interwoven system (see Chapter 4).



Scheme 5.1 Chemical reduction of MOF using metal naphthalenide (M(NAP)) in THF: A) addition of metal to naphthalene in THF, B) introduce M(NAP)-THF solution to solid MOF, C) isolate reduced MOF by filtration. M is Li, Na, or K.

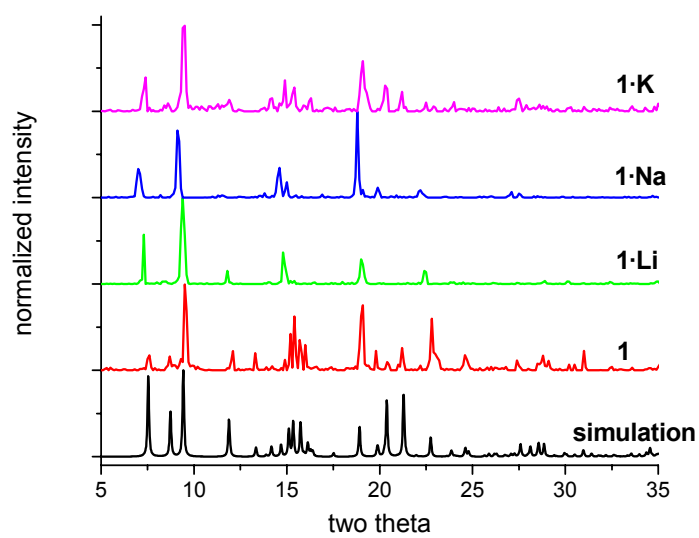
**A****B**

Figure 5.2 A) Color change of **9** upon exposure to lithium naphthalenide. B) PXRD of **9** and **9·M**.

Table 5.1 Summary of N₂ and H₂ adsorption measurements of **9** and **9·M**..

	M / Zn ^[a]	M / diPyTz	Surface area (m ² /g) ^[b]	NLDFT micropore volume (cm ³ /g) ^[c]	H ₂ wt% ^[d]	Q _{st} range (kJ/mol)
9	0.00	0.00	400 / 314	0.16	1.12	8.5 – 6.5
9·Li	0.05	0.10	526 / 365	0.19	1.46	8.3 – 6.1
9·Na	0.12	0.24	558 / 419	0.21	1.60	8.7 – 4.0
9·K	0.07	0.14	509 / 378	0.20	1.51	8.9 – 4.4
9·Li	0.35	0.70	163 / 134	0.07	0.54	9.0 – 5.0

[a] Determined by ICP analysis. [b] First value in each column is calculated by BET analysis of N₂ isotherm in 0.05 < P/P₀ < 0.30; second value is obtained from a t-plot analysis of N₂ isotherm and includes only the surface area attributable to micropores. [c] Calculated from t-plot analysis of N₂ isotherm. [d] 77K, 1 atm.

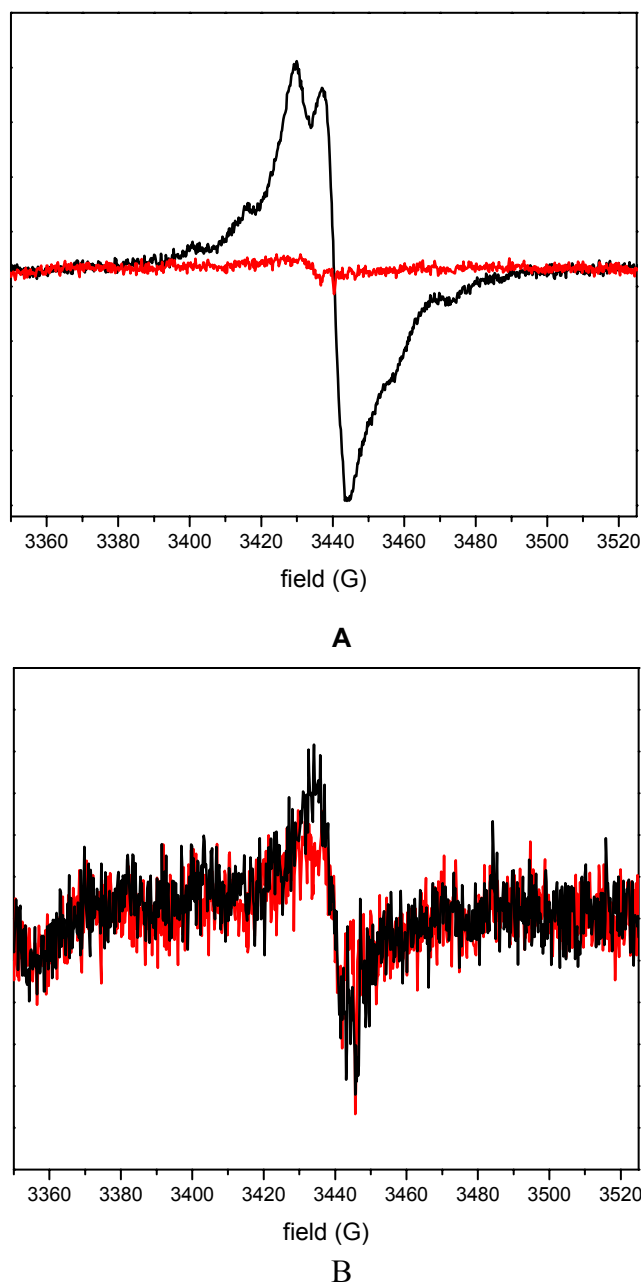


Figure 5.3 A) Solid-state room temperature CW-EPR spectra of **9** (red) and **9-Li** (black). Microwave power was 2 mW with a frequency modulation depth of 100 KHz. The small EPR signal present in the neutral sample **9** is attributed to light sensitivity of the material, as it has been demonstrated that the intensity of this signal increases upon photoirradiation (Figure 5.4B). Samples **9-Na** and **9-K** exhibited similar EPR signals. B) Solid-state room temperature CW-EPR spectra of **9** (red) and **9** after ~20 minutes of irradiation with a 100 W hand lamp (black). Microwave power was 2 mW with a frequency modulation depth of 100 KHz.

5.3.3 Hydrogen adsorption of **9** and **9·M**

Low-pressure H₂ and N₂ CO₂ isotherms were measured for **9** and all **9·M** to examine the effects that framework reduction and alkali metal doping have on H₂ uptake and on structural characteristics of the frameworks. As shown in Figure 5.4, H₂ uptake by the three reduced materials, **9·M**, considerably exceeds that for the neutral MOF. Interestingly, the greatest gravimetric uptake is observed with **9·Na**, despite the greater contribution of Na⁺ (in comparison to Li⁺) to the overall mass of the framework. Attempts to enhance uptake even further by increasing the doping level (see, for example, material **9·Li*** in Table 5.1 and Figure 5.4) actually resulted in diminished H₂ uptake in comparison to the original material.

To gain some insight into the differences in affinity for hydrogen, isosteric heats of adsorption, Q_{st} , were determined. The isosteric heat is a measure of the strength of H₂ interaction with the host material (i.e. framework, dopant, or both).^{26,27} Values were obtained by fitting a virial-type equation to the 77K and 87K H₂ adsorption isotherms.²⁸ Figure 5.5 and Table 5.1 summarize the results. In all four cases, Q_{st} decreases with increasing loading. Behavior of this kind generally is indicative of adsorption-site heterogeneity. The sites with the highest binding energy are filled first, and as the pressure is increased, incoming molecules fill other surface sites. There is a general consensus that the most favored binding sites for H₂ in conventional MOFs are metal corners^{29,30} and several groups have been successful in creating unsaturated metal centers at the corners to engender extremely favorable H₂ binding within these materials.⁸

It is tempting to ascribe the behavior encountered here, especially at low hydrogen loading, to preferential interaction of H₂ with dopant metals and/or highly polarizable, reduced struts. By chemically reducing the frameworks, we are effectively introducing additional metal centers

interspersed throughout the material. Furthermore, the added metal ions should be essentially *completely* coordinatively unsaturated – so should engender very high initial heats of adsorption. Comparison of Q_{st} values for doped and undoped versions of the MOF, however, does not provide support for the notion of strong adsorption at dopant metal sites. While minor differences can be seen, the more striking observation (Figure 5.5) is just how closely isosteric heats agree for **9**, **9•Li**, **9•Na**, and **9•K** over the entire range of H_2 pressures examined.

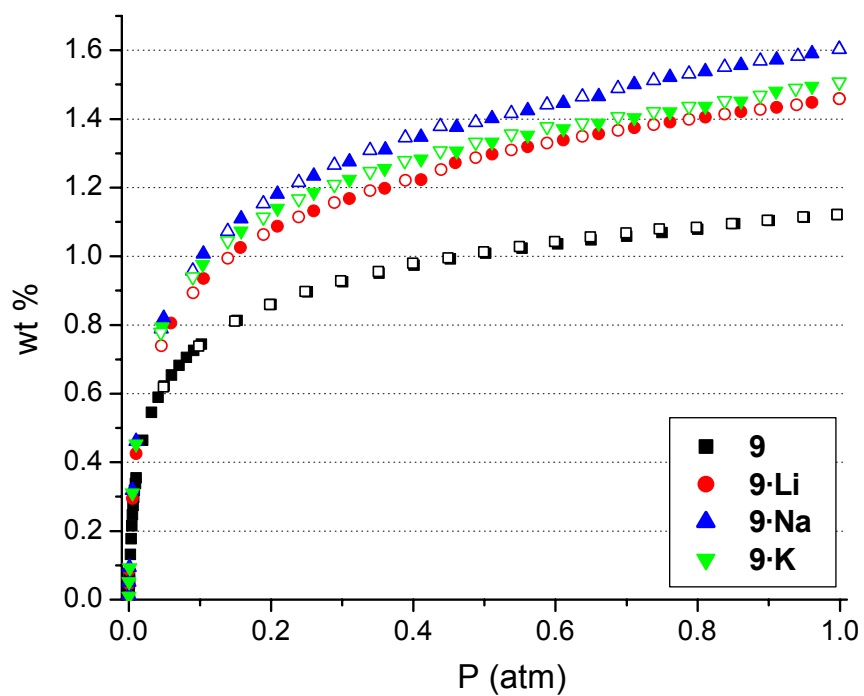


Figure 5.4 77K H₂ adsorption isotherms of **9** and **9·M**. Open symbols, adsorption; closed symbols, desorption.

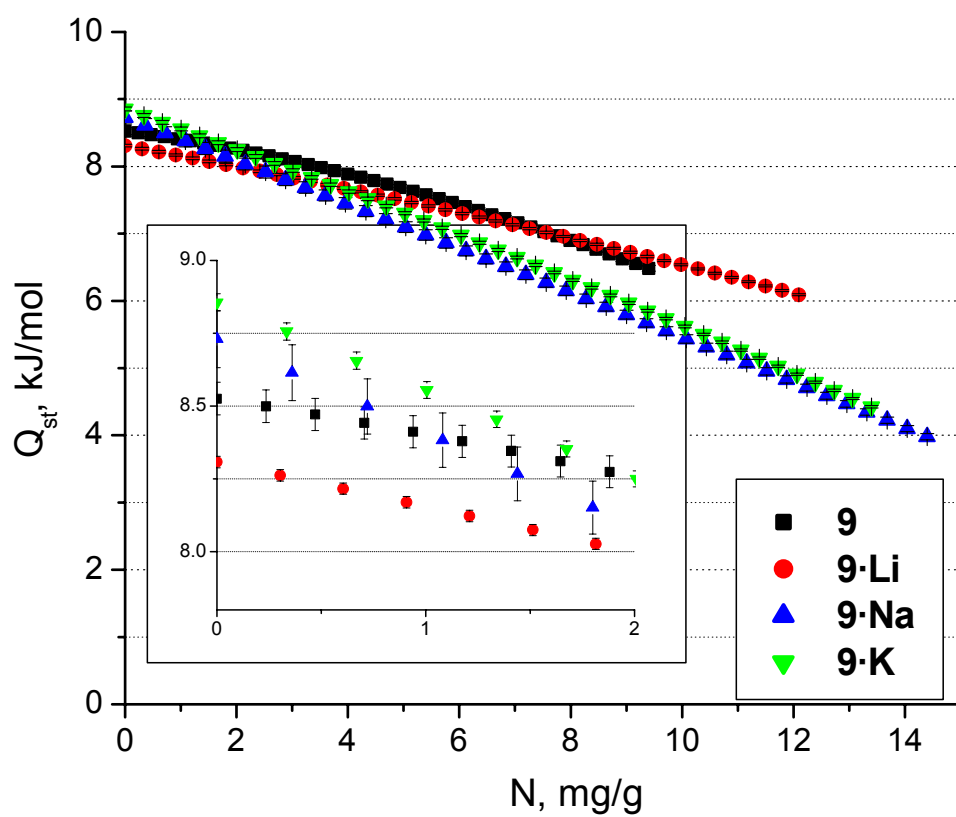


Figure 5.5 Isosteric H₂ heat of adsorption of **9·M**. Detail of behavior at low loading is depicted in inset.

5.3.4 ^1H NMR analysis of **9** and **9·M**

We conclude from the above that direct hydrogen/dopant-cation interactions are *not* responsible for the enhanced H_2 uptake illustrated in Figure 5.4. As this stands in contrast to our initial expectations, as well as expectations from recent computational studies of reduced MOFs,^{31,32} and earlier computational³³⁻³⁵ studies of carbon-based materials, we infer that the added metal ions are simply inaccessible to hydrogen. Two scenarios can be envisioned: 1) dopant cations are localized near negatively-charged carboxylates and then effectively shielded from gas exposure on account of framework interpenetration, or 2) dopant cations are strongly solvated (by DMF or THF molecules). To test the second idea, we determined the post-evacuation solvent content of the **9·M** materials via ^1H NMR. Samples were dissolved in 97% aq. D_2SO_4 and ratios of solvent molecules to struts were calculated by integrating the respective peak intensities. As a starting point, as-synthesized (non-evacuated) **9·nDMF** was dissolved in D_2SO_4 and the DMF proton peaks were compared with the peaks from the framework components. The NMR-measured solvent content of **9·nDMF** was found to be in reasonably good agreement with that from the crystal structure: 1.4 DMF per Zn(II) dimer by NMR, 1.9 DMF per Zn(II) dimer by crystallography. As shown in Table 5.2, the DMF content of **9·Na** and **9·K** is very low and is probably best interpreted as incomplete framework evacuation rather than residual cation solvation. (At most, the data are consistent with solvation of one in four dopant ions by a single DMF molecule.) For **9·Li**, however, the significance of the initially obtained results ($\sim 1.8 \text{ DMF/Li}^+$) was less clear. Consequently, the experiments were repeated with more heavily doped samples (**9·Li'** and **9·Li''**). We find the residual solvent content is independent of lithium cation loading, indicating that incomplete framework evacuation rather than solvation of dopant ions accounts for the small amount of solvent found. We can therefore rule out cation

solvation as a factor in the adsorption performance (e.g. surprisingly small Q_{st} values) of the reduced materials.

Separate measurements revealed that no detectable naphthalene (from M(NAP); see Scheme 5.1) is retained in framework-reduced materials. The proton peaks for naphthalene are sufficiently upfield from those of NDC to permit easy observation. Solubility of any naphthalene potentially remaining was ensured by dissolving the frameworks in 1:9 DMF / D_2SO_4 rather than D_2SO_4 alone.

Table 5.2 Summary of ^1H NMR quantification of solvent content in **9** and **9·M**.

	M / Zn (II) dimer	DMF / Zn(II) dimer ^[b]	mass loss (%)	DMF / M ^{+[c]}
9·nDMF	0.00	1.43	13.1	n / a
9	0.00	0.18	1.6	n / a
9·Li	0.10	0.18	1.7	1.8
9·Na	0.24	0.07	0.6	0.28
9·K	0.14	0.04	0.3	0.26
9·Li'	0.18	0.16	1.5	0.89
9·Li''	0.23	0.15	1.4	0.67

[a] 20H / Zn(II) dimer calculated from crystal structure of **9** [c] **M** loading content in Table 5.1.

5.3.5 Nitrogen adsorption of **9** and **9·M**

Quantitative comparisons at 1 atm and 77K show that low-level doping with Li^+ , Na^+ , and K^+ , respectively, increases H_2 uptake by 13, 8, and 11 molecules per alkali metal ion. (Interestingly, these numbers are greater than the maximum numbers of hydrogen molecules capable of directly interacting even with completely free cations.) The experiments above allow us to rule out both direct interactions with dopant ions and enhanced interactions with reduced struts as causes for the enhanced uptake. A third possible explanation is displacement of interwoven frameworks, by dopant ions, such that the internal surface area increases. Compelling evidence for such behavior was found in our earlier study of hydrogen uptake by a doubly-interwoven material.¹⁶

Microporous surface areas are in principle obtainable via analysis of N_2 isotherms. Inspection of the low temperature (77K) isotherms in Figure 5.6 reveals: a) very strong adsorption by all four materials, b) Type I curve shapes (indicating microporosity), and c) significantly greater uptake of nitrogen by the various **9·M**, relative to undoped **9**, in the Type I region (plateau region). While it is tempting to interpret the differences in the plateau region in terms of differences in surface area, such a conclusion is not justified for a microporous material as value in the plateau region is largely governed by pore filling, which is only indirectly related to surface area.

Recent computational work by Walton and Snurr³⁶ has shown, somewhat surprisingly, that BET (Brunauer, Emmett and Teller)³⁷ surface areas for microporous MOFs correspond closely to true surface areas, at least for N_2 as a probe molecule. As shown in Table 5.1, the BET surface areas for the various **9·M** materials significantly exceed those for the undoped parent material. Furthermore, the hydrogen adsorption follows a linear relationship with the ordering of surface

areas, $9\cdot\text{Li}^* < 9 < 9\cdot\text{K} < 9\cdot\text{Li} < 9\cdot\text{Na}$, Figure 5.7. Isotherms were also subjected to t-plot analyses,³⁸ see Table 5.3. This analysis is more appropriate in cases where low-pressure data are difficult to obtain. Here we find that the micropore volume follows a slightly different order ($9\cdot\text{Li}^* < 9 < 9\cdot\text{Li} < 9\cdot\text{K} < 9\cdot\text{Na}$) but the H_2 uptake still obeys a linear correlation to micropore volume, Figure 5.7.

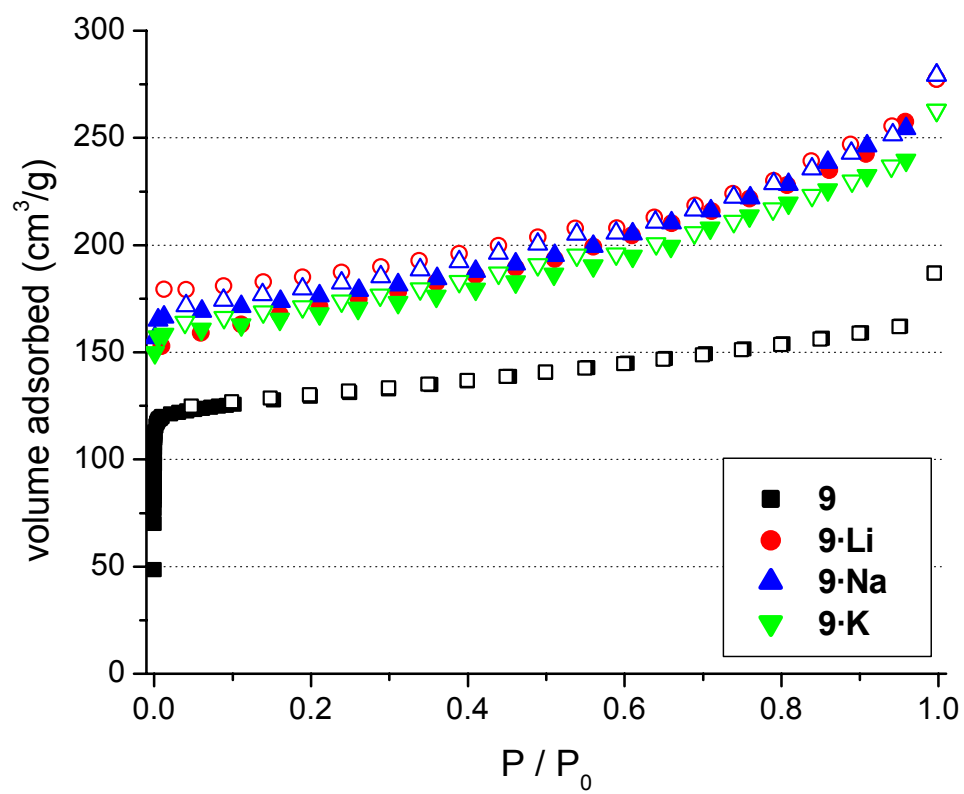


Figure 5.6 N₂ adsorption isotherms of **9** and **9·M**.

Table 5.3 Full t-plot analysis of **9** and **9-M** materials.

material	BET surface area (m ² /g) ^[a]	t-plot analysis			
		micropore volume (cm ³ /g)	micropore surface area (m ² /g)	external surface area (m ² /g)	correlation coefficient
9	400	0.16	314	86	0.999558
9·Li	526	0.19	365	161	0.998656
9·Na	558	0.21	419	140	0.997822
9·K	509	0.20	378	131	0.998852
9·Li*	164	0.07	134	30	0.996353

[a] BET surface area calculated at $0.05 < P/P_0 < 0.30$.

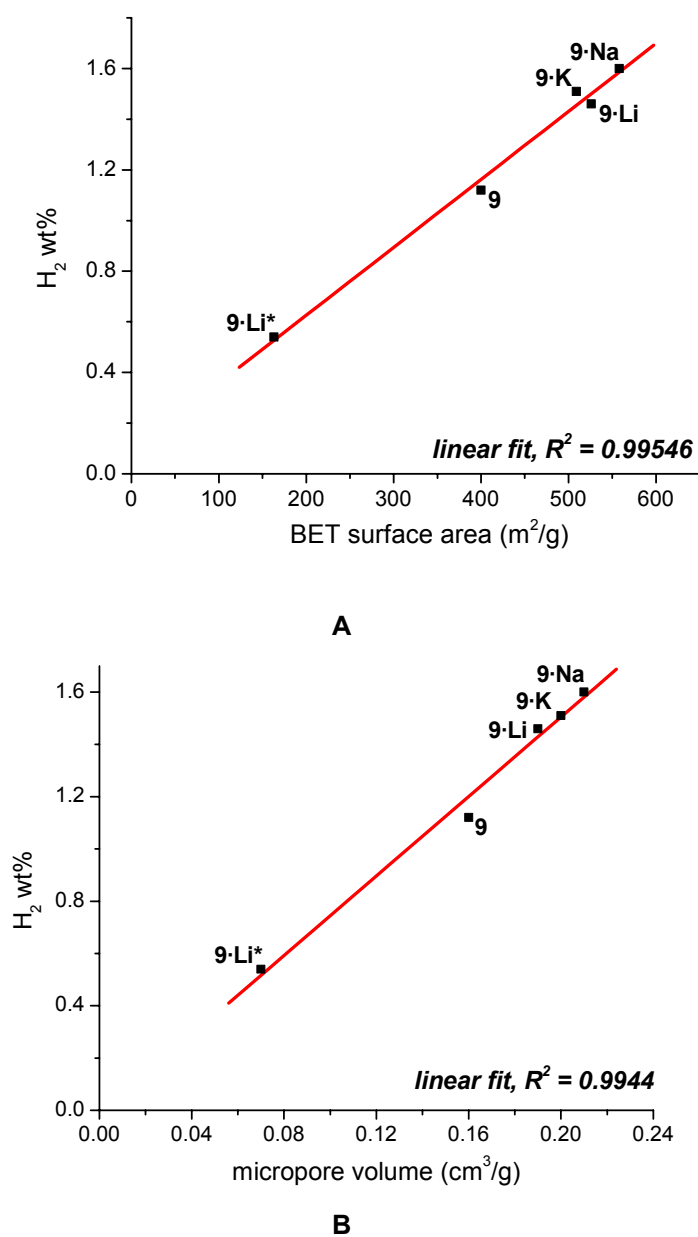


Figure 5.7 Correlation of H_2 uptake at 1 atm and 77K with (A) BET surface area and (B) micropore volume derived from t-plot analysis.

5.4 Conclusions

Partial framework reduction and doping of a triply interwoven MOF with lithium, sodium, or potassium cations enhances cryogenic uptake of H_2 by between 30 and 43% at 1 atm. The increases correspond to uptake of as many as 13 hydrogen molecules per added cation. Remarkably, the enhancements are obtained without significant changes in heats of adsorption – implying that H_2 molecules do not interact directly with dopant metal ions. NMR measurements rule out cation solvation as an explanation for the lack of direct binding of H_2 by dopant ions. We conclude instead that the added cations are shielded by the interwoven frameworks themselves from direct interaction with adsorbents. N_2 isotherms suggest that the key role of dopant cations and/or partial framework reduction in improving hydrogen uptake instead is to enhance the microporous surface area – presumably by facilitating displacement of interwoven networks.

Recent computational studies suggest that MOF binding of H_2 can be increased by as much as 500% at ambient temperature and high pressure, and that heats of adsorption can be increased by several kJ/mol,^{31,32} provided that direct interaction of dopant ions with hydrogen can be achieved. In efforts toward direct dopant- H_2 interaction, Chapter 6 is focused on cation doping and H_2 uptake within permanently microporous MOF materials comprising single, rather than multiple (i.e. catenated) networks.

Chapter 6. Hydrogen Binding in Alkoxide Functionalized Metal-Organic Frameworks

6. Chapter Overview

Chapters 3 – 5 described a method using the inherent redox activity of the organic struts within two MOF structures to chemically reduce the framework and, at the same time, introduce charge-balancing cations. The intent here was to enhance framework-H₂ binding by creating many extremely favorable binding sites for H₂ interspersed throughout the framework and ultimately enhance total uptake. And indeed, the reduced/doped materials did exhibit enhanced H₂ uptake, but most likely not by the mechanisms we had originally proposed. We expected to observe dramatic increases in the isosteric heat of adsorption, particularly at zero loading, stemming from enhanced charge-quadrupole or induced dipole-induced dipole interactions between the framework and H₂. However, in all cases, the heat of adsorption did not show significant differences from the pristine materials, and the total H₂ uptake peaks at very low doping levels, generally 5 – 10%, and then decreases significantly with higher doping levels. Detailed studies indicated that rather than the premeditated charge(framework)-quadrupole(H₂) interactions we hoped to produce within these materials, uptake enhancement was actually largely a result of structural changes induced by the cation doping. While these studies did not demonstrate the original goal or directly address the central hypothesis, they represent the first experimental studies of cation doping within MOF materials and should prove valuable in developing next generation materials.

The structures used previously were composed of interwoven frameworks, which have been shown to have the ability to shift with respect to each other. To mitigate the structural effects on H₂ binding and uptake and create direct H₂-cation interactions, we sought 1) a completely non-catenated framework, and 2) a doping method with more precise cation placement. A non-catenated structure will preclude cation “shielding” between frameworks. Greater control over

cation placement within the pores will result in more complete knowledge of the structure-function relationship in these extremely complex materials. In this Chapter, I will describe preliminary work aimed at greatly enhancing H₂ binding energy by forming alkoxide functional groups within the pores of two new MOF structures. This strategy is applicable to a wide range of cations, and here we start with lithium and magnesium.

6.1 Introduction

Metal-organic frameworks (MOFs) have received considerable attention for their potential as solid-state H₂ storage materials as a result of their crystalline, permanently porous structures, extremely low density, and immense structural and chemical tailorability.¹⁻³ One of the chief attractions in pursuing MOF materials is their well-resolved crystalline nature, not found in other porous materials such as zeolites or activated carbons. Ideally, the location of every atom within the solid framework is known exactly, thus providing an ideal scaffold for post-synthetic functionalization. The ability to modify the pore's chemical environment and therefore tune host-guest interactions with a high degree of precision renders MOF materials ideal candidates in which to investigate gas storage, separations, chemical sensing and selective catalysis.

The efficient storage of hydrogen, in addition to its sustainable production and effective transport, is key to the implementation of hydrogen as a viable fuel source.⁴ Still though, high-capacity and efficient solid-state storage materials have not yet emerged, largely due to inherently weak H₂-solid binding. Indeed, hydrogen can be chemically stored in high capacity in metal hydrides for example, but regeneration of these materials is slow and costly and they often suffer from sluggish H₂ release only at high temperatures. By contrast, materials such as MOFs that have been proposed to store molecular hydrogen by a physisorptive mechanism have very

fast kinetic release of hydrogen at relevant temperatures and pressures. However, the storage levels necessary for widespread implementation as defined by the U.S. Department of Energy (6.0 wt%, -20° – 50°C by 2010) have not been reached. Moreover, the highest H₂ heat of adsorption reported in MOF materials, 11.6 kJ/mol,⁵ is still far below that deemed necessary for relevant storage and release.⁶ The ability to alter specific sites in MOF materials and probe H₂ binding in response will provide a powerful advantage in the discovery of new and better physisorptive storage materials.

Variation and introduction of metal cations in MOF materials has been identified as a method by which to modulate and enhance H₂ heat of adsorption. Dinca and Long have demonstrated cation-dependent H₂ binding for a wide range of transition metal cations substituted in both an extraframework fashion and replacing the metal cations at the framework corners of a Mn²⁺-based structure.⁷ Likewise, Kaye and Long carried out similar cation-exchange experiments in Prussian blue analogues and monitored H₂ binding energy.⁸ Our group has focused instead on how to use the organic framework struts to introduce extraframework cations and thereby increase H₂ heat of adsorption. In this vein, we have demonstrated that lithium cation doping of MOFs via framework reduction can enhance H₂ uptake by up to 75% at low temperature and pressure.⁹ Further studies with the alkali metals Li⁺, Na⁺, and K⁺ as dopants revealed H₂ isosteric heat of adsorptions of the reduced/doped materials that did not meet our expectations based on previous H₂-alkali metal binding studies as well as computational reports.¹⁰ From these studies, we conclude that H₂ uptake was enhanced mainly from structural changes within the catenated frameworks induced by doping rather than specific H₂-cation interactions themselves.

Here we will introduce strong H₂-cation binding sites in MOF materials through post-synthetic alkoxide formation rather than framework reduction. To facilitate alkoxide formation

in the framework, we have synthesized two new mixed-ligand MOFs, both which contain meso-1,2-bis(4-pyridyl)glycol (DPG) as a pillaring strut. Unlike our previous contributions, both of these structures are non-interpenetrated and do not demonstrate dynamic framework behavior upon removal of guest solvents and subsequent gas adsorption. This is critical: here we do not wish to probe the effect pore size and shape has upon H₂ uptake and binding, which has been demonstrated elsewhere, but singly address the effect cation identity has upon H₂ entering the framework. These new structures deliver the ideal environment in which to monitor H₂-cation interactions.

We have achieved near quantitative lithium alkoxide formation in both structures even with a large discrepancy in pore sizes. For both structures, we employed solution-based ion exchange to extract the hydroxyl proton and replace it with a Li⁺ cation. Additionally, one of the alkaline earths, Mg²⁺, was also successfully pursued with the intent to induce even greater H₂ binding via charge-quadrupole interactions. To evade strong cation solvation of the presumed O-Mg-O moieties within the framework, we turned to atomic layer deposition (ALD) to deposit Mg²⁺ cations exclusively at the hydroxyl groups within the structure. By using ALD, as opposed to other thin film deposition techniques (i.e. metal sputtering, CVD, etc.), we ensure that cation deposition occurs selectively at the hydroxyl sites within the framework and not throughout. Once again, this guarantees our site-specific functionalization to probe H₂ binding and overall uptake.

6.2 Experimental

6.2.1 Materials and methods

General methods are described in Chapter 2.2.1. The syntheses of 4,4',4'',4'''-benzene-1,2,4,5-tetrayl-tetrabenzoic acid (**L1**) has previously been reported.¹¹ DPG (meso-1,2-bis(4-pyridyl)glycol) was obtained from TCI America and used as received. THF and CH₃CN were purified using a two-column solid-state purification system (Glasscontour System, Jeorg Meyer, Irvine, CA). All other commercial reagents were obtained from Sigma-Aldrich and used without further purification. ICP spectroscopy was conducted on a Varian model ICP spectrometer that is equipped to cover the spectral range from 175 to 785 nm. Samples (3-5 mg) were digested in 1:1 H₂SO₄:H₂O₂ and heated at 120°C until the solution became clear and colorless and no further vapor was produced. An aliquot of this concentrated acid solution was diluted to 5% in DI H₂O and analyzed for Li (610.365 nm), Mg (279.800 nm) and Zn (206.200 nm) content.

6.2.2 Synthesis of **16**

Single crystals of **16** were obtained by heating Zn(NO₃)₂·6H₂O (15 mg, 0.05 mmol), H₂BDC (4 mg, 0.02 mmol), DPG (5 mg, 0.02 mmol), and 5 ml DMF in a 4 dram screw cap vial at 80°C for two days. The warm mother liquor was decanted and the clear colorless crystals were washed with fresh DMF. Bulk preparation is carried out in an analogous manner:

Zn(NO₃)₂·6H₂O (225 mg, 0.76 mmol), H₂BDC (64 mg, 0.39 mmol), and DPG (82 mg, 0.38 mmol) was dissolved in 75 ml DMF, and divided between fifteen 4 dram screw cap vials. The vials were heated at 80°C for two days, upon which time clear colorless crystals formed. The crystalline solid (**16**) is isolated via filtration, washed with DMF and allowed to dry in air. Bulk purity is verified by PXRD and TGA.

6.2.3 Synthesis of **17**

Dr. Omar K. Farha developed the synthetic conditions to produce **17**. Single crystals of **17** were obtained upon heating $\text{Zn}(\text{NO}_3)_2 \cdot 6\text{H}_2\text{O}$ (50 mg, 0.17 mmol), 4,4',4'',4'''-benzene-1,2,4,5-tetrayl-tetrabenzoic acid (**L1**), (100 mg, 0.18 mmol), and DPG (25 mg, 0.12 mmol) in 25 ml DMF plus one drop of concentrated HCl. This solution was divided equally between five 4 dram screw cap vials and heated to 80°C for 3 days at which time clear colorless block crystals had formed. Bulk purity was verified by PXRD and TGA.

6.2.4 Crystallographic analysis of **16** and **17**

Single crystals of **16** and **17** were mounted on a BRUKER APEX2 V2.1-0 diffractometer equipped with a graphite-monochromated MoK α ($\lambda = 0.71073 \text{ \AA}$) radiation source in a cold nitrogen stream. All crystallographic data were corrected for Lorentz and polarization effects (SAINT). The structures were solved by direct methods and refined by the full-matrix least-squares method on F^2 with appropriate software implemented in the SHELXTL program package. Most of the guest DMF solvent molecules within the pores are severely disordered, which hindered satisfactory development of the model; therefore, the SQUEEZE routine in PLATON was applied to remove the contributions of electron density from disordered solvent molecules. The outputs from the SQUEEZE calculations are attached to the CIF file. All of the non-hydrogen atoms were refined anisotropically. The FLAT and DFIX restraints were used on the DPG ligand to stabilize the solution of **16**. See the CIF file for further details. A summary of the crystallographic data is given in Table 6.1.

Table 6.1. Summary of crystallographic data for **16** and **17**.

compound	16	17
empirical formula ^a	C ₃₆ H ₂₄ N ₂ O ₁₄ Zn ₃	C ₂₃ H ₁₃ NO ₅ Zn
formula weight	904.68	448.71
crystal color, habit	colorless, plate	colorless, block
crystal dimensions (mm ³)	0.117 x 0.115 x 0.028	0.217 x 0.109 x 0.034
crystal system	monoclinic	monoclinic
space group	P2(1)/c	P2
<i>a</i> (Å)	19.699(17)	15.7553(13)
<i>b</i> (Å)	20.490(19)	11.3014(11)
<i>c</i> (Å)	17.84(2)	15.7553(13)
<i>a</i> (deg)	90	90
<i>b</i> (deg)	110.500(18)	90.45
<i>g</i> (deg)	90	90
<i>V</i> (Å ³)	6745(11)	2805.3(4)
<i>Z</i>	4	2
ρ (calcd, g/cm ³)	0.891	0.516
μ (mm ⁻¹)	1.097	0.450
goodness-of-fit on <i>F</i> ²	0.513	0.990
<i>R</i> ^b	0.0929	0.0944
<i>R</i> _w ^c	0.2546	0.2423

^aThe SQUEEZE routine in PLATON was employed to mask diffuse electron density in the cavities due to disordered solvent (DMF) molecules. ^b $R(F) = (\Sigma F_o - F_c)/\Sigma F_o$. ^c $R_w(F_o^2) = [\Sigma [w(F_o^2 - F_c^2)^2]/\Sigma wF_o^4]^{1/2}$.

6.2.5 Alkoxide formation

In general, to perform the proton exchange and create the alkoxide frameworks, crystalline samples of **16** or **17** were submerged in THF for 1-2 days to replace the pore-filling DMF. The THF-exchanged samples were then stirred vigorously in dry THF/CH₃CN with a metal source overnight. The solid was then isolated by filtration, washed with copious amounts of THF to remove any weakly physisorbed ions, dried briefly in air, and quickly transferred to an adsorption sample tube.

Stoichiometric loading is defined here as the amount of alkoxide formation per DPG strut. The crystal structure of **16** gives 1 DPG strut per Zn₃ cluster; stoichiometric loading is then 2 Li(I) per 3 Zn(II). The crystal structure of **17** gives 1 DPG strut per Zn₂ cluster, stoichiometric loading here is 2 Li(I) per 2 Zn(II). Specific preparation procedures follow:

Synthesis of 16-Li: **16** (80 mg dry, 0.13 mmol) was added to a 100 ml round bottom flask equipped with a magnetic stir bar and covered with 30 ml CH₃CN. Lithium-*tert*-butoxide (28 mg, 0.35 mmol) was added to the flask with 10 ml THF. The flask was closed and stirred vigorously at room temperature overnight. The crystalline solid was isolated via filtration, washed with THF and CH₃CN, and transferred to an adsorption analysis tube. ICP analysis for Li/Zn returned 1.80 ± 0.03 Li / Zn₃ cluster.

Synthesis of 17-Li_{2.62}: **17** (13 mg) was added to a 100 ml flask, covered with 20 ml THF, and stirred vigorously. Lithium-*tert*-butoxide (4 mg, 0.05 mmol) was added to the flask and stirred at room temperature overnight. ICP analysis for Li/Zn returned 2.62 ± 0.05 Li / Zn₂ cluster.

Synthesis of 17-Li_{0.20}: **17** (~10 mg) was added to a small scintillation vial, covered with 3 ml CH₃CN, and stirred gently with 2 ml LiOtBu solution (1.0M THF solution) overnight. The solid

was washed with THF several times and isolated via filtration. ICP analysis for Li/Zn returned 0.20 ± 0.01 Li / Zn₂ cluster.

Synthesis of **17-Mg**: **17** (~30 mg) was added to a small conical vial, covered with 3 ml THF and stirred vigorously to create a strong dispersion. Mg(OMe)₂ (60 μ l, 6-10% solution in MeOH) was added to the vial, which was then capped and allowed to stir overnight. ICP analysis for Mg/Zn returned 0.86 ± 0.02 Mg / Zn₂ cluster.

6.2.6 Low-pressure adsorption measurements

Adsorption measurement details are found in Chapter 2.2.5. Samples of **16** and **16-Li** were outgassed at 150°C, samples of **17**, **17-Li**, and **17-Mg** were outgassed at 200°C prior to analysis.

6.2.7 Atomic layer deposition

Atomic layer deposition (ALD) was performed by Dr. Alex B. F. Martinson at Argonne National Laboratory. Prior to ALD, samples of **17** were completely activated by THF exchange and outgassing at 200°C. Samples of pristine **17** were placed in a powder holder in the ALD reactor. Two reactor temperatures were attempted to monitor differences in loading: **17-Mg**₁₀₀ (100°C reactor) and **17-Mg**₂₀₀ (200°C reactor). Only one ALD cycle was performed consisting of one ten minute pulse of bis(cyclopentadienyl)magnesium(II) (MgCp₂) and one five minute pulse of water.

6.3 Results and Discussion

6.3.1 Structure of 16

The mixed-ligand MOF approach that we, and others, have established has proven extremely beneficial for obtaining solid-state structures that contain a variety of chemical functionalities.¹² Therefore, we chose to use this same methodology to incorporate the hydroxyl-containing ligand

DPG into a framework material. Prototypical synthesis conditions of heating a mixture of $\text{Zn}(\text{NO}_3)_2 \cdot 6\text{H}_2\text{O}$, terephthalic acid, and DPG in DMF at 80°C for 2 days resulted in clear colorless plate-like single crystals. Single crystal X-ray diffraction did not reveal Zn(II)-paddlewheel geometry however, but here we have obtained a related pillared network structure containing both ligands, Figure 6.1. Overall, the structure features Zn_3 clusters separating a hexagonal arrangement of BDC ligands in two-dimensional sheets which are pillared in the third direction by DPG to give the framework formula $\text{Zn}_3(\text{BDC})_3(\text{DPG})$, **16**. Notably, the structure of **16** is non-interpenetrated and the hydroxyl groups of DPG are clearly accessible to the cavity voids, and application of the SQUEEZE¹³ routine in PLATON estimates a remarkable 58% solvent accessible void volume in the crystal structure.

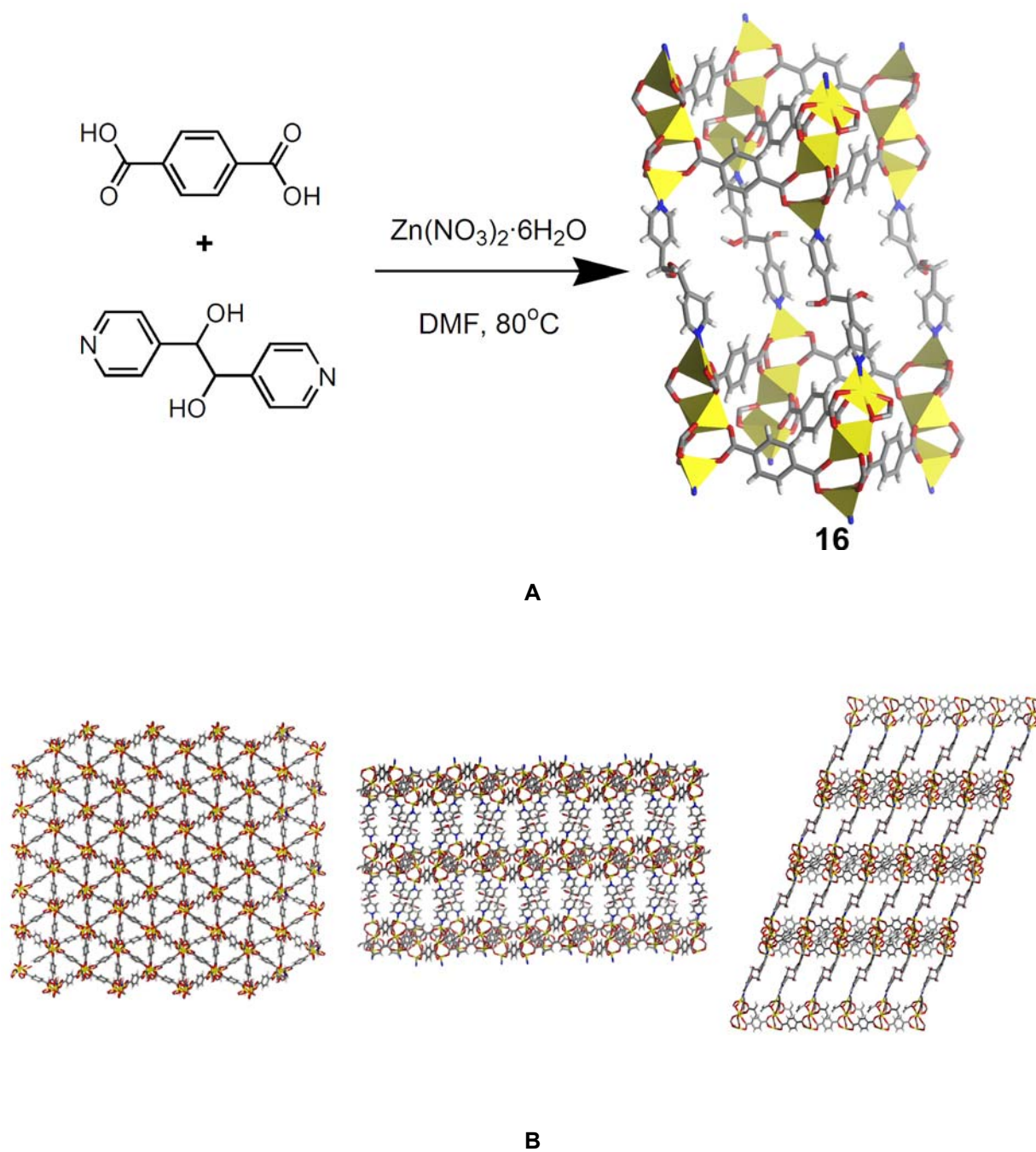


Figure 6.1. A) Reaction scheme and crystal structure of **16**. Yellow polyhedra represent zinc ions; gray, carbon; blue, nitrogen; red, oxygen. B) Packing diagrams of **16**.

6.3.2 Formation and characterization of **16-Li**

The presence of hydroxyl ligands in this new structure and their direct protrusion into the open cavities renders them immediately accessible for exchange with alkali metal cations, alkaline earths, or even bulkier cations such as NH_4 . These cation-exchanged variants will then be used to systematically probe H_2 -framework interactions. Lithium was chosen as the first cation to attempt exchange for three reasons: 1) $\text{H}_2\text{-Li}^+$ binding energy is calculated to be ~ 20 kJ/mol in the gas phase,¹⁴ 2) exchange of a proton for a lithium cation will not add substantial additional mass to the framework, which would depreciate total gravimetric uptake, and 3) very recent computational reports of lithium doping (both via framework reduction¹⁵⁻¹⁷ and alkoxide formation¹⁸) suggest that the addition of lithium to MOF materials can greatly enhance total uptake at ambient temperatures.

Following preliminary experiments with harsh lithiation reagents such as n-butyllithium and methyllithium, we chose to use a milder lithium-exchange reagent to preserve structural integrity.¹⁹ Quantitative exchange of the hydroxyl protons was achieved simply by stirring the MOF material in an excess of lithium t-butoxide in $\text{CH}_3\text{CN/THF}$ to give **16-Li**; this procedure was sufficient to produce the lithium alkoxide of the DPG strut alone, Figure 6.2. In the solid framework, the Li:Zn stoichiometry was verified by ICP analysis of **16** and **16-Li** and structural integrity of **16-Li** was verified by PXRD and TGA.

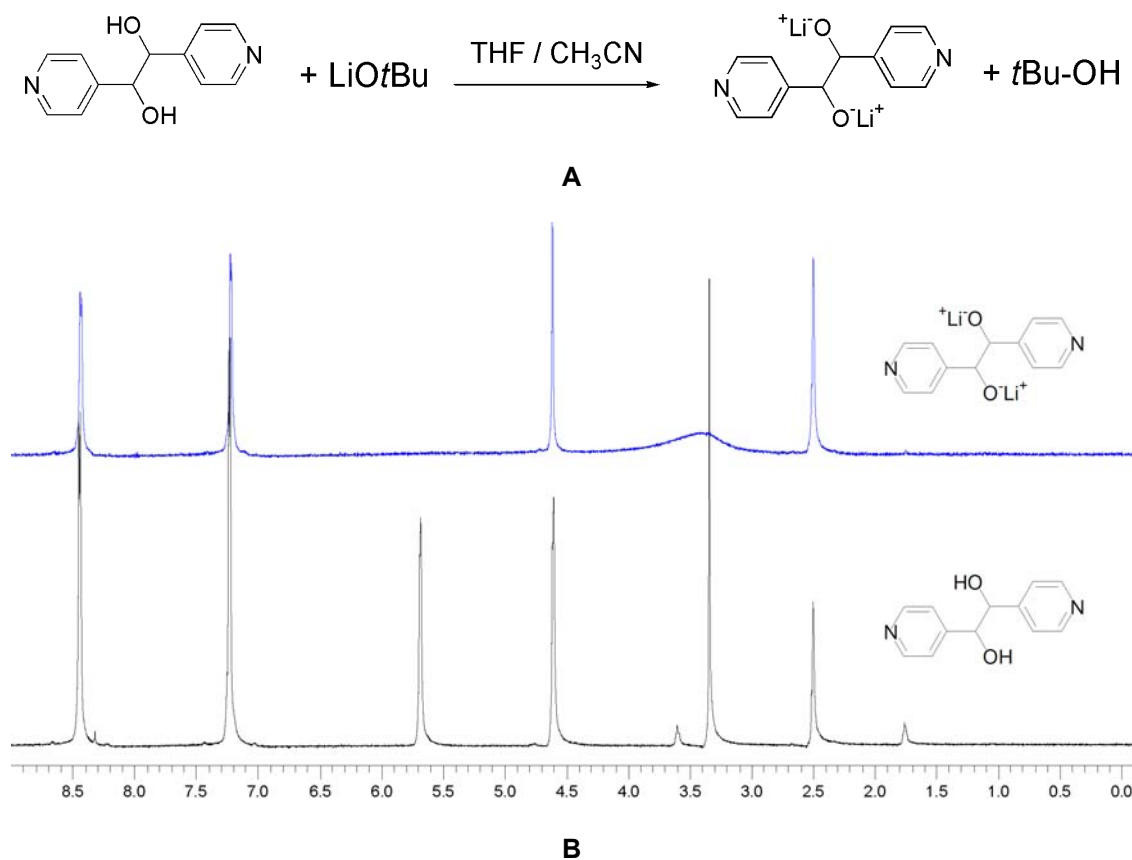
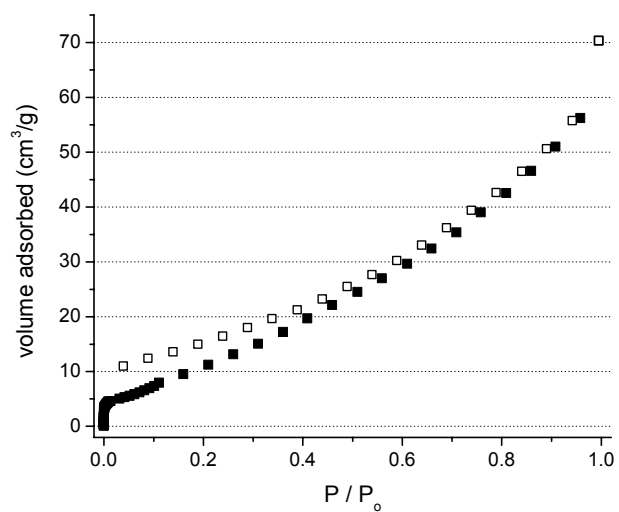


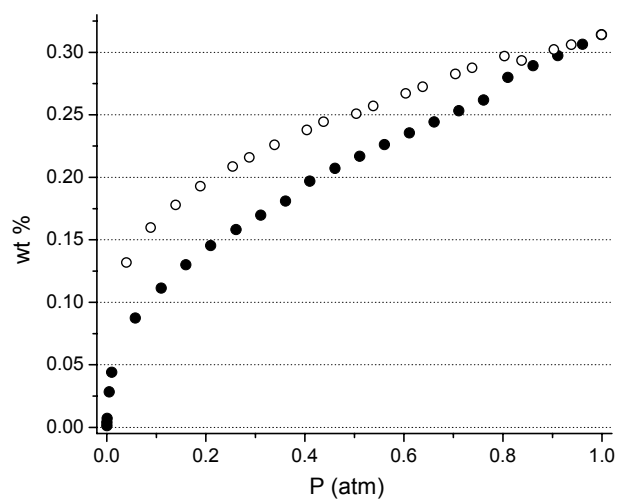
Figure 6.2. A) Proton-lithium exchange scheme. B) 400 MHz ^1H NMR of DPG (bottom) and DPG- 2Li^+ (top) in DMSO-d_6 . Note hydroxyl proton peak at 5.7 ppm is not present in lithium alkoxide spectra.

6.3.3 Nitrogen and hydrogen adsorption of **16**

Low-pressure adsorption measurements (N_2 , H_2) were performed on **16** and **16-Li** to probe the effect of lithiation on the interior pore environment. Despite the apparently open channels present in the crystal structure, this was not reflected in the adsorption isotherms, Figure 6.3. The N_2 isotherm is roughly Type II resulting in a BET surface area of only $52 \text{ m}^2/\text{g}$. The low-pressure H_2 isotherms of **16** were similarly disappointing, topping out at only 0.31 wt% at 77K and 1 atm. Likewise, the adsorption isotherms of **16-Li** also resulted in very low uptake, with a BET surface area of $51 \text{ m}^2/\text{g}$ from the N_2 isotherm and 0.25 wt% H_2 at 77K and 1 atm.



A

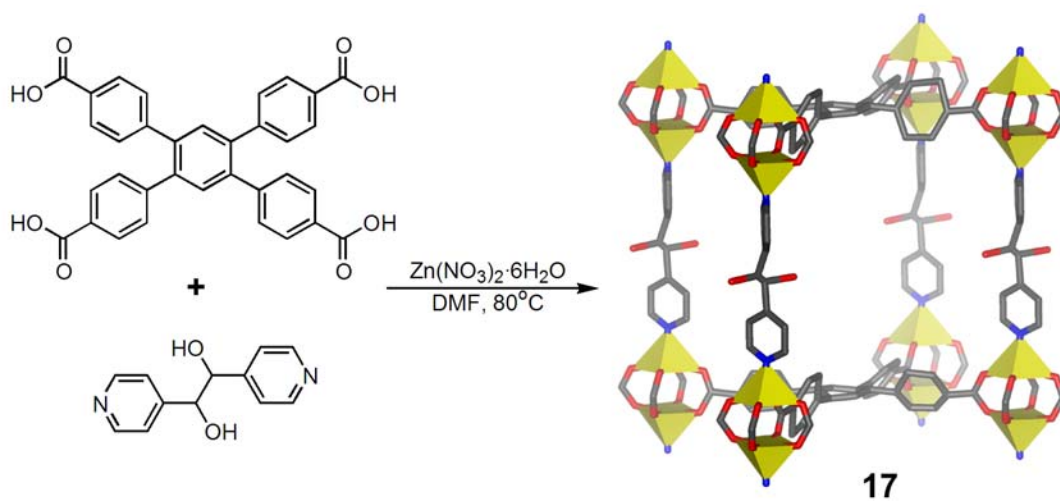


B

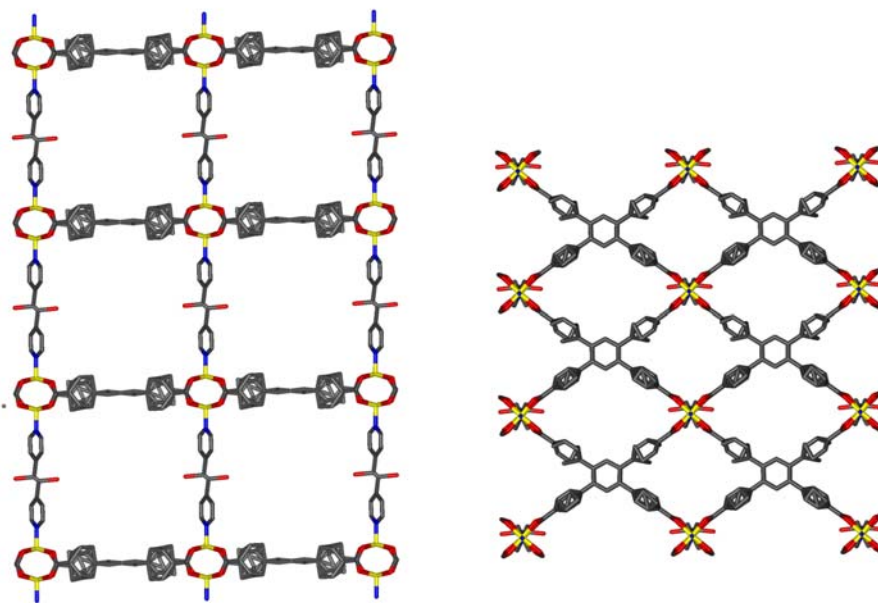
Figure 6.3. A) N₂ adsorption isotherm of **16**, BET surface area 52 m²/g. Closed symbols, adsorption; open symbols, desorption. B) 77K H₂ isotherm of **16**.

6.3.4 Structure of **17**

Despite the inferior adsorption performance by **16** and **16-Li**, we were nonetheless encouraged by the extent of lithiation achieved within the pores as a step toward applying this technique in MOF materials with well behaved adsorption characteristics. To that end, we pursued a second mixed-ligand framework containing the DPG strut, this time using a tetratopic carboxylate ligand recently developed in our group, 4,4',4'',4'''-benzene-1,2,4,5-tetrayl-tetrabenzoic acid (L1), Figure 6.4.¹¹ Empirically, we have observed that this ligand results in very thermally stable structures that completely withstand pore evacuation, most likely a direct result of the four-point binding possible with this ligand. Heating a mixture of $\text{Zn}(\text{NO}_3)_2 \cdot 6\text{H}_2\text{O}$, L1, and DPG in DMF at 80°C for two days resulted in clear colorless block crystals suitable for single crystal X-ray diffraction. Analysis of the data indeed reveals a mixed-ligand Zn(II) paddlewheel framework as we anticipated, to give a framework formula of $\text{Zn}_2(\text{L1})(\text{DPG})$, **17**, Figure 6.4. The Zn dimers are coordinated by the tetracarboxylate L1 ligands that form two-dimensional sheets, and these sheets are pillared by the DPG struts. The structure is completely non-interpenetrated, resulting in an incredible 76% solvent accessible void volume. Moreover, as in structure **16**, the hydroxyl functionalities are completely accessible to these large cavities, which also renders **17** amenable to post-synthetic proton exchange. TGA characterization of **17** (Figure 6.5) reveals an almost instantaneous mass loss (suggesting very large pores) of 55%. The initial solvent loss ends at 150°C and is followed by a stable plateau region until ~300°C at which point structural degradation begins. The distinct mass loss and relatively wide plateau region indicates a high degree of structural stability, which is encouraging considering the substantial pores and slightly flexible nature of the DPG ligand.



A



B

Figure 6.4. A) Reaction scheme and crystal structure of **17**. Yellow polyhedra represent zinc ions; gray, carbon; blue, nitrogen; red, oxygen, hydrogens omitted for clarity B) Packing diagrams of **17**.

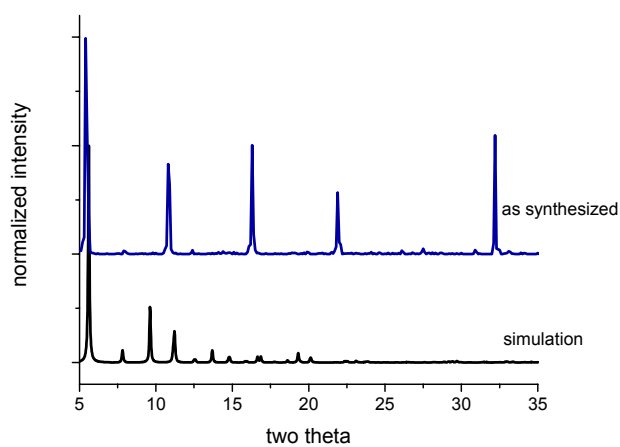
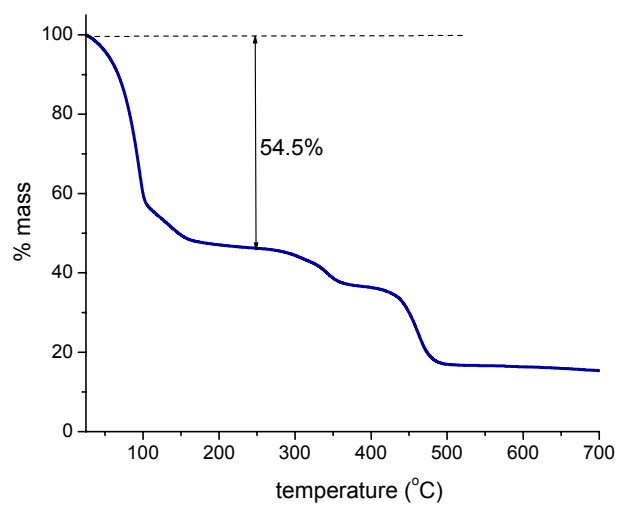
**A****B**

Figure 6.5. Bulk characterization of **17** by PXRD (A) and TGA (B).

6.3.5 Nitrogen and hydrogen adsorption of **17**

The N₂ adsorption isotherm of **17** is shown in Figure 6.6 and the associated structural data is found in Table 6.2. The very high initial uptake and subsequent level adsorption are representative of a standard Type I isotherm, indicative of a microporous material, with a BET surface area of 813 m²/g. The low pressure H₂ adsorption isotherm of **17** (Figure 6.7) is completely reversible and demonstrates an uptake of 1.23 wt% at 1 atm. The H₂ uptake was also measured at 87K and both isotherms were fit to a virial equation to calculate the isosteric heat of adsorption,²⁰ Figure 6.8. The adsorption results are fairly typical for a structure of this nature, here most importantly demonstrative of the permanent porosity of **17**.

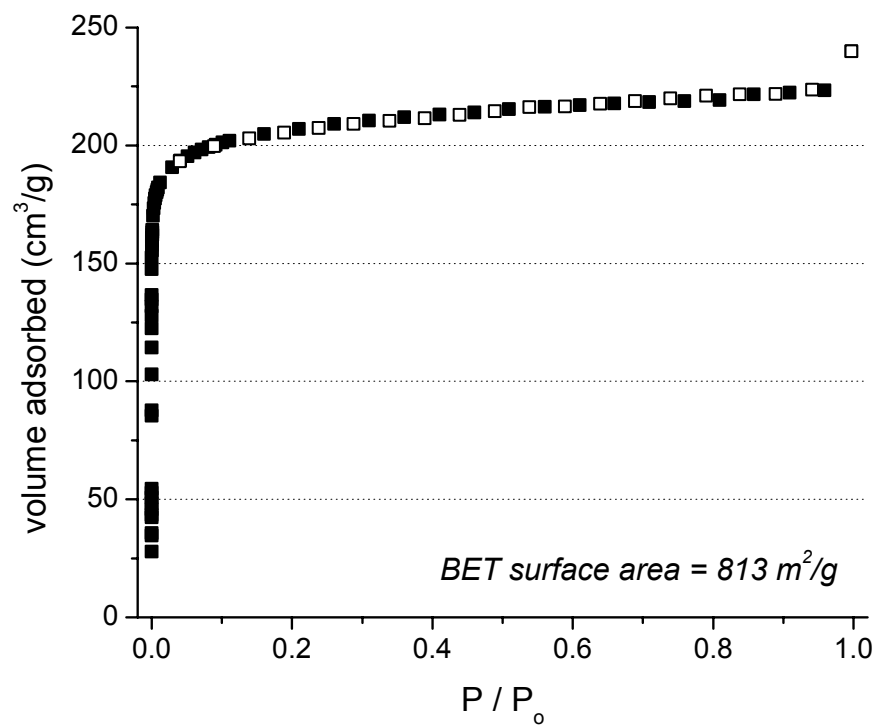


Figure 6.6. N₂ adsorption isotherm of **17**. Closed symbols, adsorption; open symbols, desorption.

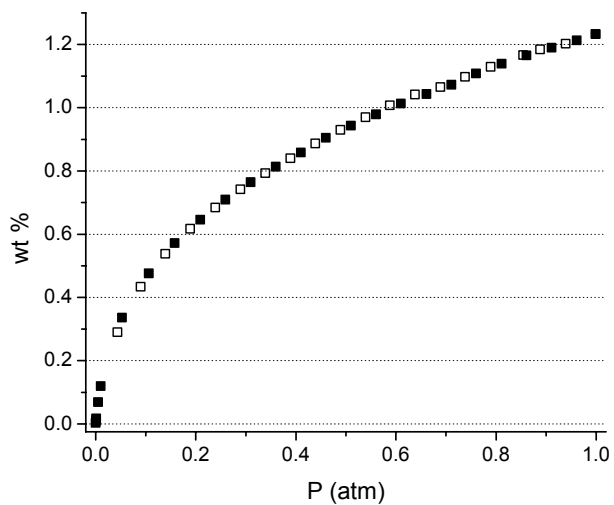
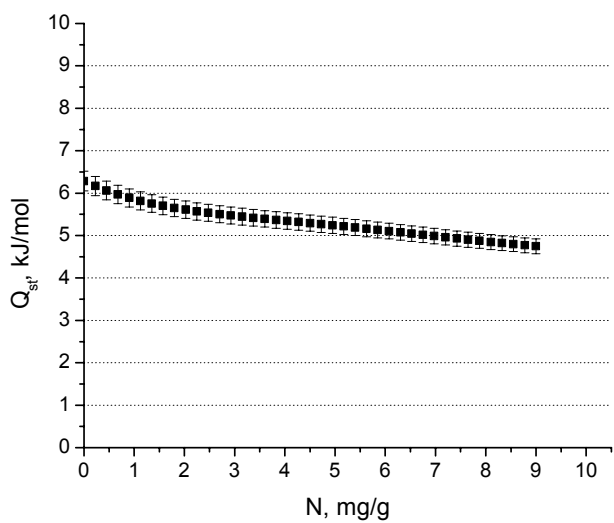
**A****B**

Figure 6.7. A) 77K H₂ adsorption of **17**, and B) H₂ isosteric heat of adsorption of **17**.

Table 6.2. Summary of N₂, H₂ adsorption of **17**.

material	M / DPG ^[a]	BET surface area (m ² /g) ^[b]	pore volume (cm ³ /g)	H ₂ wt% (1 atm, 77K)	Q _{st} , kJ/mol
17	0	813	0.35	1.23	6.3 – 4.7
17-Li_{2.62}	2.62 ± 0.05	270	0.20	0.77	5.6 – 0.5
17-Li_{0.20}	0.20 ± 0.01	835	0.46	1.32	6.6 – 6.3
17-Mg	0.86 ± 0.02	818	0.40	1.16	6.8 – 6.2
17-Mg₁₀₀	0.03	707	0.47	1.71	7.2 – 1.0
17-Mg₂₀₀	0.06	603	0.42	1.30	6.6 – 4.9

[a] Determined by ICP analysis. [b] Calculated in range $0.007 < P/P_0 < 0.05$. [c] total pore volume at $P/P_0 = 0.95$.

6.3.6 Formation and characterization of **17-Li**

Confident in the structural stability of **17**, we performed proton-lithium exchange procedures, again using an excess of LiOt-Bu in CH₃CN/THF to create **17-Li**. Once again, lithium substitution was verified by ICP analysis of **17-Li** as compared to **17**. Here we examined two different levels of alkoxide functionalization, ~2.6 Li / DPG strut (**17-Li_{2.62}**) and ~0.2 Li / DPG strut (**17-Li_{0.20}**), see Table 6.2. The significant difference between the preparation of **17-Li_{2.62}** and **17-Li_{0.20}** is the stirring mechanism—the material with higher loading (**17-Li_{2.62}**) was stirred much more vigorously overnight and resulted in a fine powder. The material with lower loading (**17-Li_{0.20}**) was agitated gently and the well formed block crystals largely retained their shape and integrity. The degree of proton substitution is most likely heavily reliant on the ability for the lithium cation (and solvation shell or anion) to diffuse through the pores to *every* site, even deep within the crystals.

The N₂ isotherm of both **17-Li** samples verifies the permanent porosity, even after alkoxide formation within the pores, Figure 6.8. However, the total uptake and BET surface area of **17-Li_{2.62}** is much lower than the starting material, which could be a result of the visible loss of crystallinity during preparation. Several different activation methods were attempted to prepare fully desolvated **17-Li** which would present fully unsaturated lithium cations as binding sites for incoming H₂ molecules. Prior to alkoxide formation, pore-filling solvent molecules in as-synthesized **17** were completely exchanged by subjecting the material to reduced pressure at only room temperature after exchanging the original DMF solvent molecules for more volatile THF over approximately one day. Structural degradation was not observed before 200°C, and the optimal activation conditions found for **17** and **17-Li** is to heat at 200°C under reduced pressure for about 24 hours. By subjecting these alkoxide-functionalized structures to high heat and

reduced pressure, we hope to thermally remove any solvent molecules coordinated to the lithium cations. Several groups have prepared unsaturated metal centers at transition metal nodes in MOF materials, heating under vacuum at temperatures as low as 150°C have been sufficient to remove coordinated solvent molecules in some cases.

The H₂ isotherms of **17-Li** as compared to **17** did not display significant further uptake, Figure 6.9. However, the slight increase of **17-Li_{0.20}** over **17** at 1 atm corresponds to an additional 2 H₂ per Li⁺ cation (due to the low loading). This is fully consistent with computational reports that state an exposed lithium cation on carbon materials or MOFs can bind up to 6 H₂ molecules.¹⁴ The H₂ heats of adsorption of **17** and **17-Li** are presented in Figure 6.10. Note that the H₂ isosteric heat of adsorption of **17-Li_{0.20}** has a much different shape than what is typically observed in MOF materials. It has approximately the same zero-loading value as the hydroxylated material, **17**. However, instead of decreasing with loading, it *rises* slightly. This behavior is very unusual, and at first blush, non-physical. Typically the binding energy will be at a maximum at zero loading, that is, the first molecules to reach the surface bind at the sites with the highest interaction energy. After those high-energy sites are full, the rest of the surface can be filled, although at weaker interaction energy. Similar behavior has been reported in a series of Ti-decorated porous silicas.²¹⁻²³ The rising slope is rationalized as either adsorption at multiple sites or a change in H₂ ligand binding to the Ti center. The Ti centers decorating the surface can participate in Π -back bonding to the H₂ orbitals, or rather effect a Kubas interaction.²⁴ In the case of **17-Li**, the Li centers cannot invoke Kubas interactions necessarily, but they appear to be creating specific interactions that are definitely unique from the original material.

While the heat of adsorption plot **17-Li** is promising, the trend observed here is not terribly striking, and so it is difficult to definitively pinpoint the source of the rise in interaction energy.

Recall that at each pressure point of the isotherm the gas-solid is in equilibrium, with the adsorbate H_2 molecules able to sample all the available adsorption sites, albeit most likely the cation sites for longer and more frequently. Therefore, the adsorption measurements are not a *direct* observation of H_2 -specific site binding or heat of adsorption, such as can be obtained through variable temperature IR spectroscopy²⁵ or microcalorimetry. We reasoned that in addition to some residual solvent molecules blocking Li^+ binding sites, perhaps the H_2 -Li alkoxide interactions are simply not strong enough to detect within the pore interiors. Computational reports of the H_2 - Li^+ interaction strength in MOF materials ranges from 8 kJ/mol to 12 kJ/mol.^{17,26} To create even stronger H_2 -cation interactions which should be more readily observed in this complex material, we chose to attempt proton exchange with the Mg^{2+} cation, which will presumably induce stronger charge-quadrupole interactions.^{27,28}

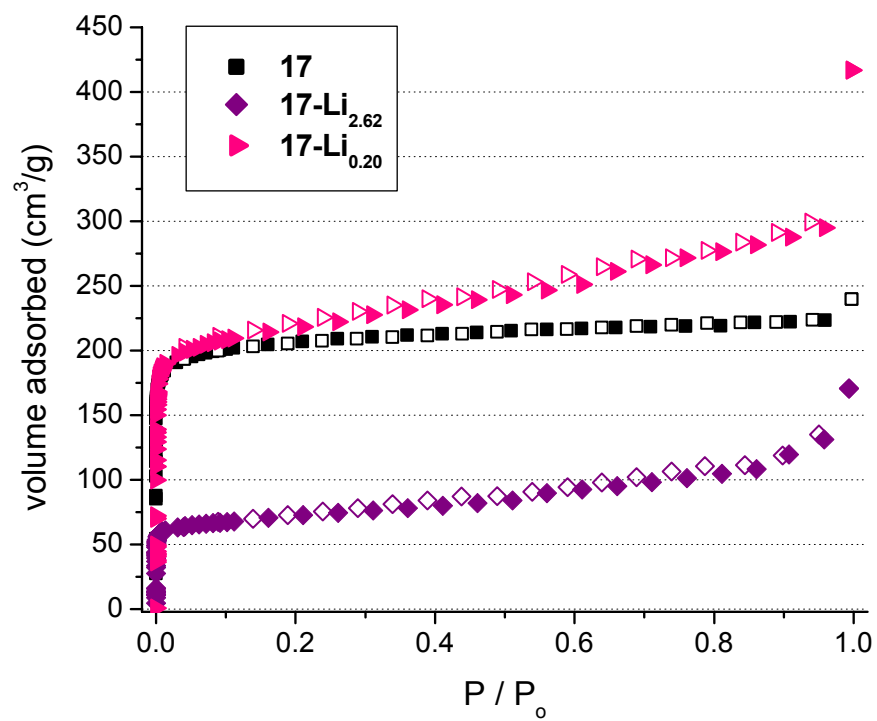


Figure 6.8 N₂ adsorption isotherms of **17** and **17-Li** materials. Closed symbols, adsorption; open symbols, desorption.

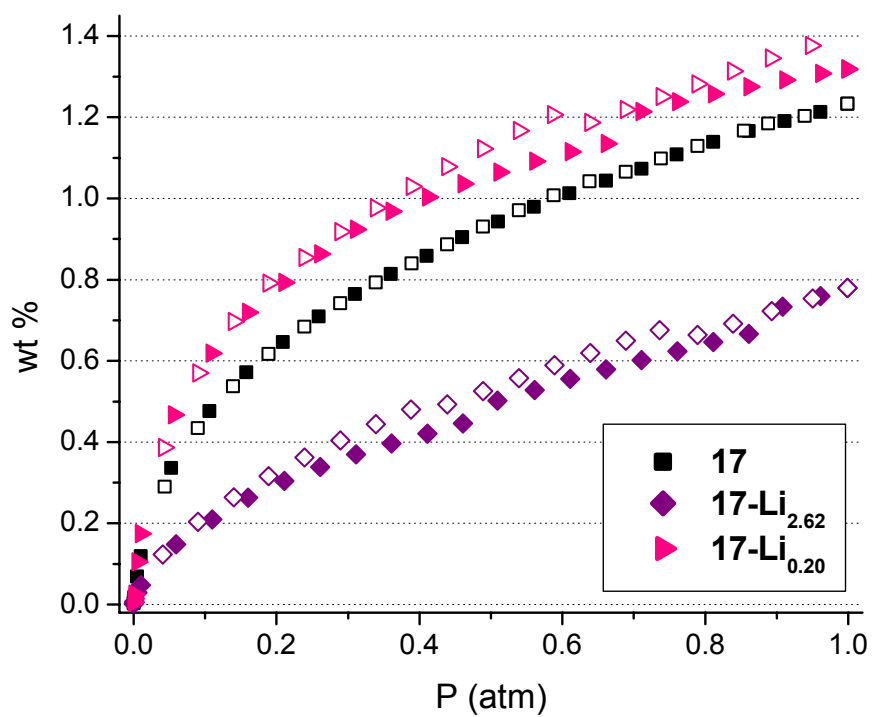


Figure 6.9 77K H₂ adsorption isotherms of **17** and **17-Li**.

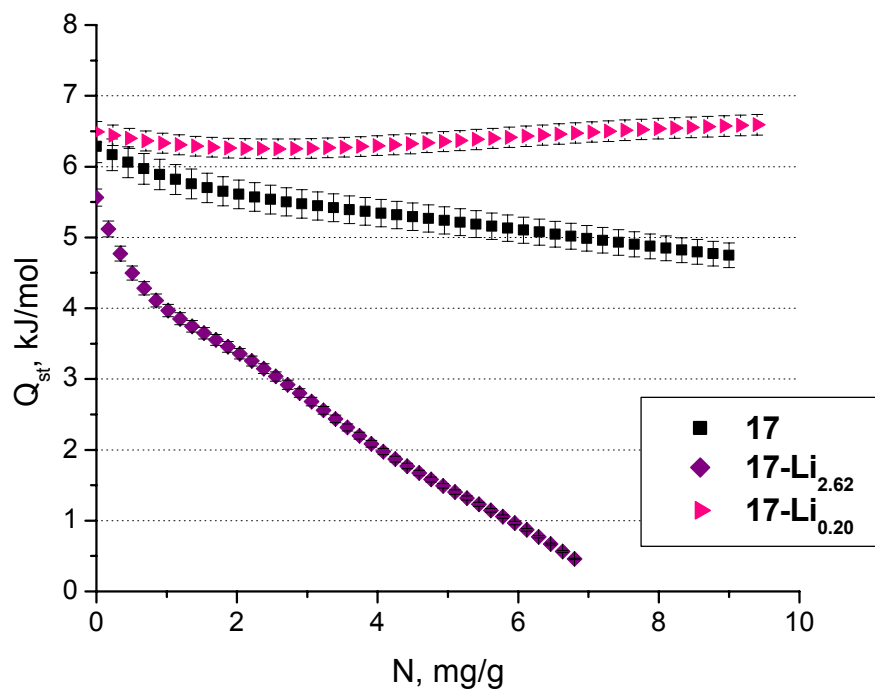
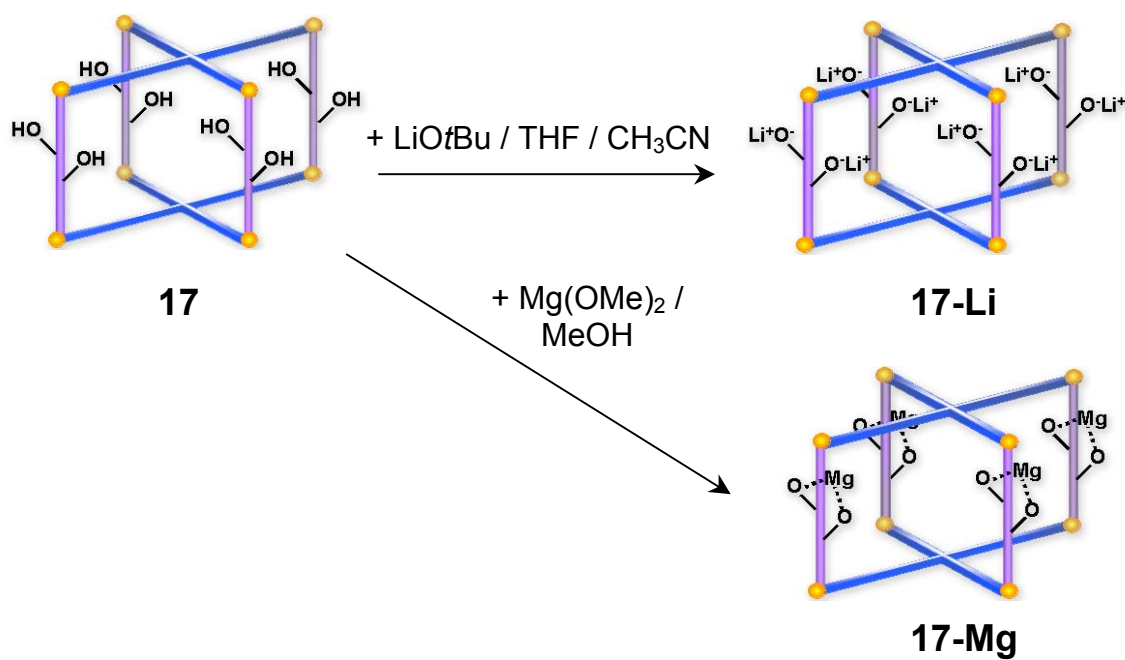


Figure 6.10 H₂ isosteric heat of adsorption of **17** and **17-Li** materials.

6.3.7 Formation and characterization of **17-Mg**

Initial attempts at hydroxyl-proton exchange of **17** with Mg^{2+} to form **17-Mg** were quite successful using a solution of $\text{Mg}(\text{OMe})_2$ in methanol as the magnesium source. Interestingly, ICP analysis of the washed and dried **17-Mg** materials gave a Mg:Zn ratio of $\sim 1:2$, rather than the $\sim 2:2$ Li:Zn ratio found in **16-Li** and **17-Li**. From these results, we propose here that rather than a single hydroxyl proton exchanged for a Mg^{2+} cation (which would necessitate another charge balancing anion, most likely the methoxide anion in this case), both protons on each DPG strut are removed per added divalent cation, see Scheme 6.1. Repeated attempts to obtain single crystals after magnesium functionalization and provide definitive structural characterization were unsuccessful.

N_2 adsorption of **17-Mg** confirms the permanent porosity after proton exchange with virtually no change in surface area or pore volume (Figure 6.11, Table 6.2). The low-pressure H_2 adsorption isotherms and isosteric heat of adsorption for **17** and **17-Mg** are shown in Figure 6.12. The H_2 uptake for **17-Mg** is actually just slightly below that of **17** at 1 atm. However, note the heat of adsorption plot for **17-Mg** as compared to **17**. Like that for **17-Li_{0.20}**, it has approximately the same value at zero loading and then slightly increases as loading increases. This behavior is more peculiar, since there is no increase in total uptake, only the observation of increasing heat of adsorption with loading. However, the one computational account that has proposed alkoxide formation within MOFs to boost H_2 uptake reports that largest increases are observed at room temperature and the enhancements at cryogenic temperatures are quite modest.¹⁸



Scheme 6.1. Proposed exchange scheme and structures of **17-Li** and **17-Mg**.

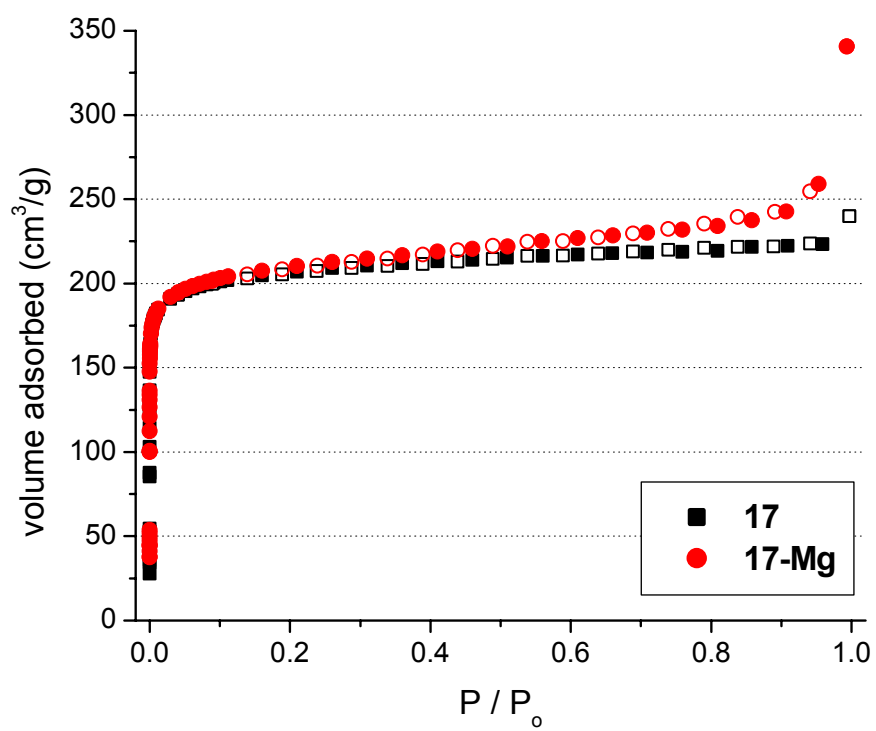


Figure 6.11 N₂ adsorption isotherms of **17** and **17-Mg**. Closed symbols, adsorption; open symbols, desorption.

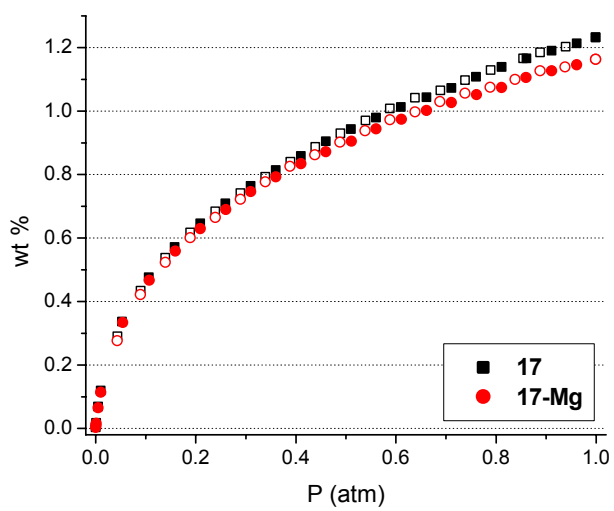
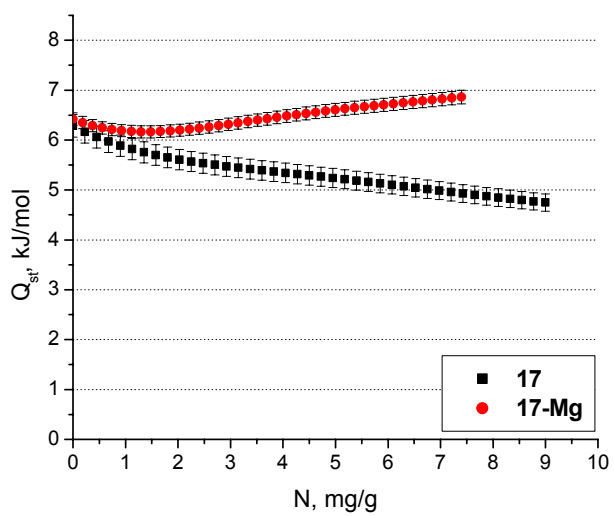
**A****B**

Figure 6.12. A) 77K H₂ adsorption isotherms of **17** and **17-Mg**. B) Isosteric H₂ heat of adsorption plots for **17** and **17-Mg**.

6.3.8 Atomic layer deposition of Mg^{2+} in **17**

Solution-phase alkoxide formation via simple proton/cation exchange proved to be quite efficient for obtaining alkoxide formation within the MOF pores. However, the H_2 isosteric heat of adsorption, particularly for **17-Mg**, although it demonstrates interesting behavior versus loading, was still not nearly as high as we expected for *direct* $\text{H}_2\text{-Mg}^{2+}$ interactions. H_2 binding energy of 17 kJ/mol in Mg-exchanged zeolites has been measured directly,²⁵ much higher than the 6 – 7 kJ/mol calculated from the adsorption measurements above. Using a technique such as atomic layer deposition (ALD)²⁹ will allow us to avoid the use of solvents completely and selectively deposit cations only at the hydroxyl sites within the framework. ALD is a gas-phase film deposition method that is used to grow conformal coatings via sequential self-terminating reactions. Most commonly, it is used to grow metal-oxide thin films from hydroxylated surfaces. It is unique among metal- and thin-film deposition techniques because the sequence of reactor pulses ensures deposition of only one atomic layer at a time. This results in an unprecedented level of control over film location, thickness, and composition.

Here, rather than growing a thin film on a flat surface, we wish to take advantage of the hydroxyl groups within the pores to deposit only one atomic layer of Mg^{2+} at the hydroxyl sites of the DPG strut. The first two attempts at alkoxide functionalization via ALD in **17** are not near stoichiometric formation, but the initial results are promising. The low loading level (3% and 6%, see Table 6.2) is most likely a factor of the large particle size of the MOF crystallites. Diffusion of the MgCp_2 precursor through these high aspect ratio crystallites will be very slow and is probably the reason for the low loading.

6.3.9 Nitrogen and hydrogen adsorption of **17-Mg-ALD**

The N₂ adsorption isotherms of the **17-Mg-ALD** materials are presented in Figure 6.13. There is a definite change in the materials structure, the isotherm of **17** is unquestionably Type I, with a very flat plateau and little condensation at the top of the isotherm. The isotherms of **17-Mg-ALD** are closer to Type II, which is more dramatic in the material prepared in the 200°C reactor, and the surface area decreases for both. The pristine material is stable at 200°C, but the water vapor pulse at 200°C following the MgCp₂ pulse may have an effect on the structure.

Despite the decrease in surface area of **17-Mg₁₀₀**, the H₂ uptake is substantially higher than **17**, Figure 6.14. The increase at one atmosphere corresponds to an additional 5.8 H₂ per Mg²⁺ cation. The heat of adsorption plot of **17-Mg₁₀₀** has a slight increase over **17** at zero loading, but not necessarily what one would expect for direct H₂-Mg²⁺ binding. The **17-Mg-ALD** samples were prepared with one pulse of MgCp₂ followed by a water pulse to “cap” the presumed O-Mg-O moieties with water ligands while in the reactor. These samples were activated at 200°C, which should remove the water ligands, but we have not yet devised a way to quantitatively detect any remaining water ligands. Water ligands that remain coordinated to the Mg cations would block H₂ access and obstruct the strong charge-quadrupole interactions we are attempting to engender in these materials.

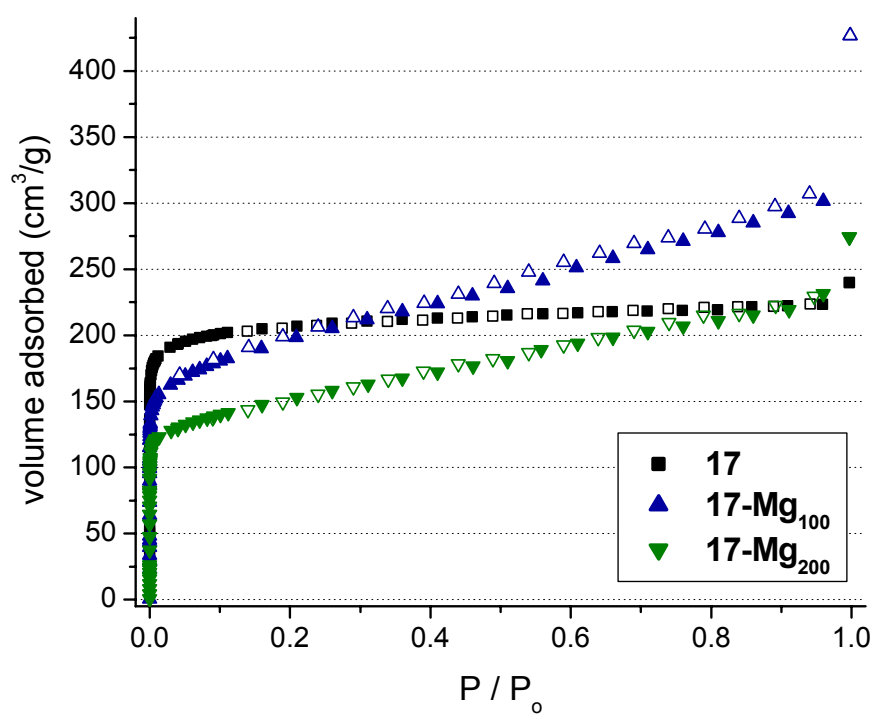
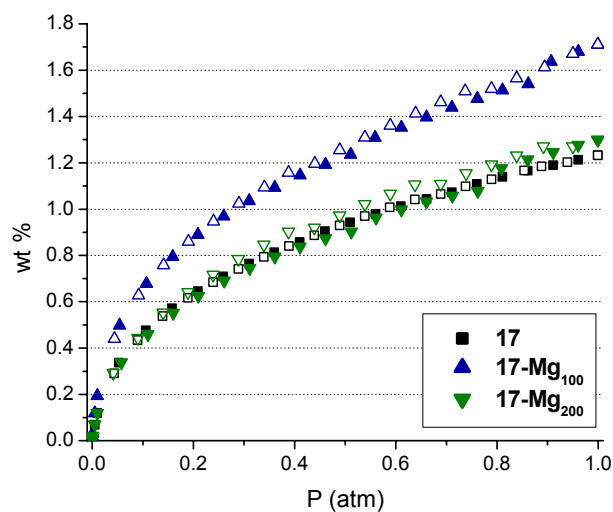
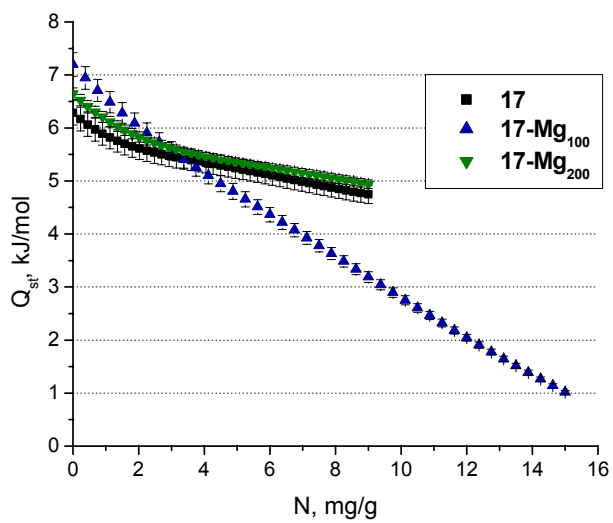


Figure 6.13. N₂ isotherms of Mg-ALD materials. Closed symbols, adsorption; open symbols, desorption.



A



B

Figure 6.14. A) 77K H₂ adsorption isotherms of Mg-ALD materials. B) H₂ isosteric heat of adsorption of Mg-ALD materials.

6.4 Conclusions

In summary, we have introduced two new hydroxyl functionalized mixed-ligand MOF structures and exchanged the hydroxyl protons for lithium and magnesium cations via solution exchange and ALD methods. Alkoxide formation by solution or gas phase methods provides yet another tool in the MOF chemist's arsenal to probe host-guest relationships within the pores. We expect the alkoxide functionalization to not only be a convenient method by which to introduce any number of cations within the framework, but also provide activated reaction centers for further post-synthetic modification.

Unlike the studies presented in Chapters 3 – 5, there are no major structural changes in **17** after alkoxide formation. The isotherm shape remains Type I, and for most samples there is very little difference in surface area and pore volume from the pristine material. And remarkably, for a lithium and magnesium exchanged material, we observe *increasing* heat of adsorption with loading. This phenomenon has been observed before in Ti-decorated porous silicas and in that system, the H₂ heat of adsorption reached a remarkable 22 kJ/mol.²²

These promising preliminary results have laid the foundation for extensive, systematic studies in which to probe the alkoxide formation in MOF materials via exchange monitoring temperature, solvent, metal source/precursor, solution or gas phase to achieve the optimal loading level for H₂ uptake. Also, variables in the activation conditions such as solvent exchange, temperature, and pressure should also be comprehensively examined to realize the preparation that will completely expose the metal centers toward incoming H₂ adsorbate molecules while maintaining structural integrity.

Additionally, the use of a gas-phase technique to selectively modify MOF materials is heretofore unprecedented. There have been reports of sputtering metals within MOFs to observe

a H₂ “spillover” effect,³⁰⁻³² but ALD is unique in that it *selectively* reacts with the hydroxyl groups. ALD is a relatively mature technique, so dozens of metals can be deposited within these or similar hydroxyl-containing framework materials. One can envision invoking extremely strong Kubas-type interactions with the appropriate metal center bound at the hydroxyl groups. Additionally, most transition metal centers can be desolvated fairly easily (as compared to lithium or magnesium) to then expose regularly spaced, abundant unsaturated metal centers to incoming H₂ molecules.

Chapter 6 concludes the studies of hydrogen storage in metal-organic frameworks. The promise of hydrogen storage rests in overcoming weak H₂-solid interactions. I have introduced new techniques to address this topic in 1) framework reduction, and 2) alkoxide formation, by which to controllably and reliably modify the charge and cation identity within MOF materials to attempt to augment the H₂-framework interaction energy.

**Chapter 7. An Interpenetrated Framework Material with Gated N₂ Sorption and
Hysteretic CO₂ Uptake**

7. Chapter Overview

The previous four chapters have specifically addressed methods by which to increase H₂ uptake and binding in MOF materials. From exploiting the inherent redox activity of the framework struts in Chapters 3-5 to the exchangeable hydroxyl protons in Chapter 6, the controlled introduction of framework charge and concomitant cations through modification of the MOF struts has been the underlying strategy to introduce specific cation binding sites for H₂ to increase heat of adsorption and thereby total uptake. However, particularly in Chapters 3-5, the experimental studies in which we intended to study solely H₂-cation or H₂-strut interactions by adsorption measurements were complicated by structural changes that accompanied framework reduction. In these examples, we demonstrated the enhancement of H₂ uptake, but it was near impossible to differentiate the effects of framework reduction and doping from the effects of structural changes that appeared to be induced by framework reduction and doping. Initiating these experimental studies, we did not anticipate significant structural changes upon reduction and doping since one of the immediate characteristics of most MOF materials is their well-ordered, crystalline structure.

The final chapter does not specifically address H₂ storage within MOF materials but rather concludes with a study of the adsorption behavior of an apparently flexible MOF structure. The structure examined here is a close relative of the structures described in Chapter 2 and those applied for H₂ adsorption studies in Chapters 3-5, rendering these studies relevant to the observations and conclusions from these previous chapters.

7.1 Introduction

The introduction and subsequent wide-reaching pursuit of new and exotic metal-organic frameworks (MOFs) has opened new doors into the structural possibilities of crystalline, porous solid-state materials.^{1,2} Perhaps hundreds of new MOF structures are published every year, and the ability to engender structural and chemical diversity with relative ease within MOFs has long been recognized. However, once the metal nodes and organic ligands are arranged into the crystalline framework, their structure is largely stagnant. More recently, the ability of some of these *crystalline* materials to demonstrate structural *flexibility* has been reported.³ For example, several of the MIL materials from the Férey group exhibit a “breathing” mechanism upon solvent removal and pore filling with gas adsorbates.⁴⁻⁷ Guest induced structural changes have been demonstrated via single-crystal to single-crystal transformations by several groups.^{8,9} Technologically exciting hysteretic H₂ uptake in flexible frameworks has been observed both at low pressure¹⁰ and high pressure.¹¹ The ability to effect guest-responsive structural behavior in traditionally crystalline MOF materials is becoming more apparent.¹²⁻¹⁷ However, very few of these reports examine three-dimensional frameworks,¹⁸ even fewer investigate catenated structures,¹⁹ and most often, the reported flexible behavior is observed only at high pressure. A guest-responsive, structurally flexible porous material that demonstrates dynamic performance under more subtle conditions of pressure and temperature could have application potential in gas separations or as highly selective sensors of guest adsorbates.

Here we describe a new two-fold catenated pillared paddlewheel framework based on mixed-ligand Zn(II) coordination of a tetratopic carboxylate ligand and a linear dipyridyl ligand. This structure is interpenetrated rather than interwoven, as the frameworks are maximally displaced from one another. The N₂ and Ar adsorption isotherms display a surprising gating effect,

whereas there is virtually *no* adsorption until the gate pressure. Notably, the low-pressure CO₂ isotherms display a prominent step and a substantial repeatable hysteresis loop. And perhaps most interestingly, high-pressure CO₂ isotherms indicate that these structural changes are also observed at technologically relevant conditions for CO₂ sequestration. Taken together, these remarkable adsorption results suggest dynamic structural behavior upon removal and re-adsorption of pore guests. Speculatively, this dynamic behavior may be reversible pore collapse or obstruction, the catenated frameworks shifting with respect to each other, or strut rotation.

7.2 Experimental

7.2.1 Materials and methods

General methods are detailed in Chapter 2.2.1. The syntheses of 4,4',4'',4'''-benzene-1,2,4,5-tetrayl-tetrabenzoic acid²⁰ (**L1**) and *N,N'*-di-(4-pyridyl)-1,4,5,8-naphthalenetetracarboxydiimide²¹ (**L2**) have previously been reported. All other reagents were purchased from Sigma Aldrich and used as received unless otherwise noted.

7.2.2 Synthesis of **18**

Dr. Omar K. Farha obtained single crystals of **18** suitable for X-ray crystallography and developed synthetic conditions for large scale preparation in a pure phase. A sample preparation of **18** follows: Zn(NO₃)₂·6H₂O (167 mg, 0.56 mmol), H₄TATPB (300 mg, 0.54 mmol), and diPyNI (120 mg, 0.28 mmol) were dissolved in 60 ml DMF. This solution was divided equally between sixteen two-dram screw cap vials and heated to 80°C for 2 days. The warm mother liquor was decanted, the yellow microcrystalline powder was washed with fresh DMF and the solid material was stored under fresh DMF until characterization by PXRD.

7.2.3 Crystallographic analysis of **18**

A single crystal of **18** was mounted on a BRUKER APEX2 V2.1-0 diffractometer equipped with a graphite-monochromated MoK α ($\lambda = 0.71073$ Å) radiation source in a cold nitrogen stream. All crystallographic data were corrected for Lorentz and polarization effects (SAINT). The structures were solved by direct methods and refined by the full-matrix least-squares method on F^2 with appropriate software implemented in the SHELXTL program package. Most of the guest DMF solvent molecules within the pores are severely disordered, which hindered satisfactory development of the model; therefore, the SQUEEZE²² routine in PLATON was applied to remove the contributions of electron density from disordered solvent molecules. The outputs from the SQUEEZE calculations are attached to the CIF file. All of the non-hydrogen atoms were refined anisotropically. A summary of the crystallographic data for **18** is given in Table 7.1.

Table 7.1 Summary of crystallographic analysis of **18**.

compound	18^a
empirical formula	C ₂₉ H ₁₃ N ₂ O ₆ Zn
formula weight	550.78
crystal color, habit	yellow, block
crystal dimensions (mm ³)	0.141 x 0.131 x 0.095
crystal system	Orthorhombic
space group	Imma
<i>a</i> (Å)	22.898(13)
<i>b</i> (Å)	15.668(9)
<i>c</i> (Å)	22.389(12)
<i>a</i> (deg)	90
<i>b</i> (deg)	90
<i>g</i> (deg)	90
<i>V</i> (Å ³)	8032(8)
<i>Z</i>	8
<i>r</i> (calcd, g/cm ³)	0.911
<i>m</i> (mm ⁻¹)	0.00016(4)
goodness-of-fit on <i>F</i> ²	1.107
<i>R</i> ^b	0.0659
<i>R_w</i> ^c	0.0792

^aThe SQUEEZE routine in PLATON was employed to mask diffuse electron density in the cavities due to disordered solvent (DMF) molecules. ^b $R(F) = (\Sigma F_o - F_c)/\Sigma F_o$. ^c $R_w(F_o^2) = [\Sigma[w(F_o^2 - F_c^2)^2]/\Sigma w F_o^4]^{1/2}$.

7.2.4 Low-pressure adsorption measurements

Prior to adsorption measurements, samples of as-synthesized **18** were submerged in THF for approximately one day to fully exchange DMF in the pores for a more volatile guest. The supernatant solution was exchanged several times for fresh THF. The yellow microcrystalline solid was then isolated via vacuum filtration and transferred to a sample tube of known mass. Low-pressure N₂, Ar, H₂, and CO₂ adsorption measurements were carried out on an Autosorb 1-MP from Quantachrome Instruments. Ultra-high purity grade He, H₂, and N₂ and research grade CO₂ were used for all adsorption measurements. The sample was fully activated at 25°C under dynamic vacuum of 10⁻⁵ torr for ~24 hours. N₂ adsorption isotherms were measured at 77K, Ar adsorption was measured at 87K and 77K, H₂ adsorption isotherms were measured at 77K and 87K, and CO₂ adsorption was measured at temperature points between 263K and 298K, maintained by an isothermal water bath.

7.2.5 High-pressure CO₂ adsorption measurements

High-pressure adsorption measurements were performed on an HPVA-100 from VTI Corporation. Detailed schematics and data analysis information has been reported elsewhere.²³ A sample of **18** (approximately 800 mg) was activated *ex situ* under the conditions outlined above and then transferred to the appropriate sample cell. The cell containing activated **18** was placed under vacuum for an additional two hours to remove any weakly physisorbed water adsorbed during sample transfer. After complete activation, the sample cell was closed and transferred to the analysis port, where the sample cell was maintained at constant temperature by a water bath.

7.3 Results and discussion

7.3.1 Structure of **18**

We have previously described a library of pillared paddlewheel MOFs based upon mixed-ligand Zn(II) coordination to linear dicarboxylates and dipyridyls²⁴ (see also Chapter 2). This approach has allowed us to introduce any number of chemical functionality into framework materials including redox-activity,^{25,26} catalytic behavior,²⁷ and readily modifiable struts.²⁸ In the present work, we have created a new structure containing a tetratopic carboxylate ligand, 4,4',4'',4'''-benzene-1,2,4,5-tetrayl-tetrabenzoic acid (**L1**). We reasoned that this long strut would result in a MOF structure with relatively large pores and that the four-point connectivity would produce a structure exceptionally stable to guest removal. The linear dipyridyl ligand *N,N'*-di-(4-pyridyl)-1,4,5,8-naphthalenetetracarboxydiimide (**L2**) was used here since MOF materials containing this ligand have previously formed very stable structures.

The static heating of **L1**, **L2**, and $\text{Zn}(\text{NO}_3)_2 \cdot 6\text{H}_2\text{O}$ in DMF at 80°C for 2 days resulted in single crystals suitable for X-ray diffraction. Analysis of the single crystal data reveals a framework formula of $\text{Zn}_2(\text{L1})(\text{L2})$ in two catenated networks, structure **18** (Figure 7.1). **L1** bridges the Zn(II) dimers and forms flat two-dimensional sheets; notably, this is different ligand geometry than previously reported for a single-ligand MOF structure with **L1**.²⁰ These perforated two-dimensional sheets are then pillared by **L2**. However, unlike most other pillared paddlewheel structures we have encountered, these networks are *interpenetrated* as opposed to *interwoven*, indicating that networks are maximally displaced from one another. The **L2** pillars reside directly in the center of the diamond-shaped cavities formed by two of the **L1** ligands, and the substantial steric bulk of **L2** completely fills this void space (Figure 7.2). This type of

catenation results in a pore volume that is essentially halved from what would be observed in a single, non-catenated network.

Despite the framework interpenetration, the structure retains 50% solvent accessible void volume as calculated by the SQUEEZE routine of PLATON. TGA of **18** demonstrates a solvent loss of 38% mass centered at 135°C and completely removed by 200°C (see Figure 7.3).

Framework decomposition does not begin until 350°C, indicating a high degree of stability for a large-pore paddlewheel-type MOF, most likely a direct result of the four-point binding of **L1**.

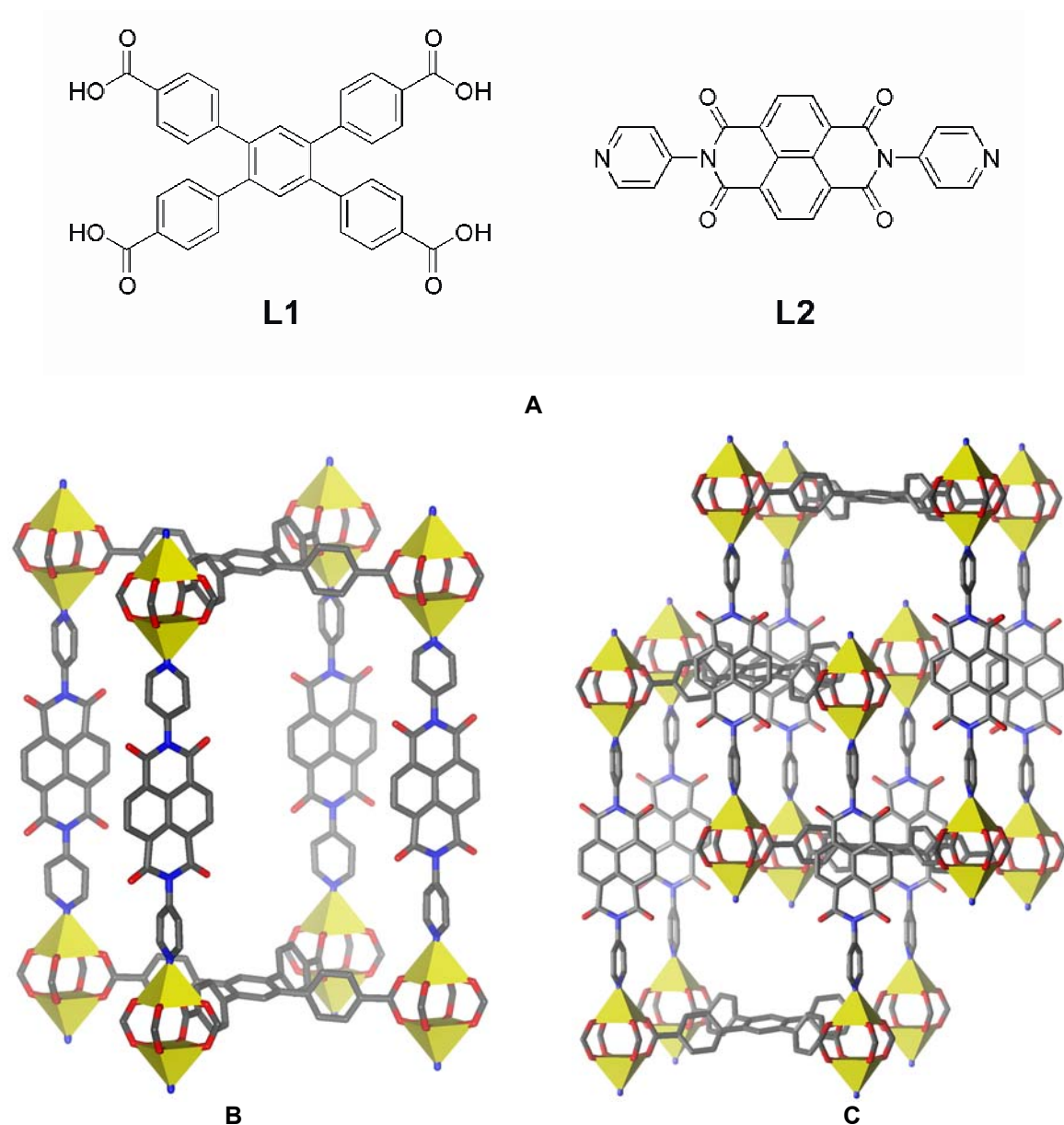


Figure 7.1. A) Chemical structure of **L1** and **L2**, B) Crystal structure of **18**, one level of interpenetration is omitted to illustrate connectivity. Yellow polyhedra represent zinc ions; gray, carbon; blue, nitrogen; red, oxygen. Hydrogens omitted for clarity. C) Catenation of **18**.

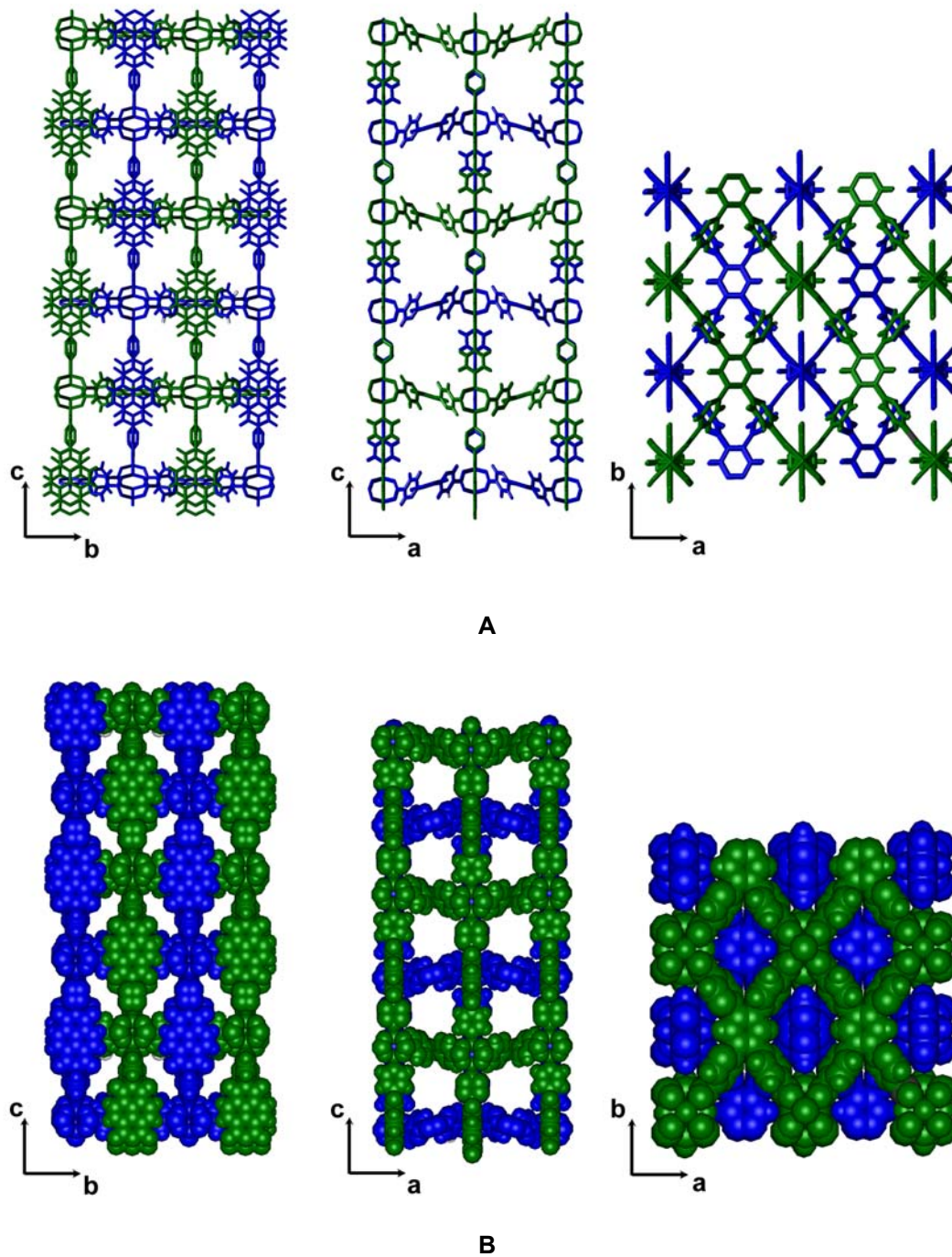


Figure 7.2. Packing diagrams of **18** to illustrate interpenetration. Individual frameworks are different colors. A) Stick models down a, b, and c axes. B) Spacefilling models down a, b, and c axes.

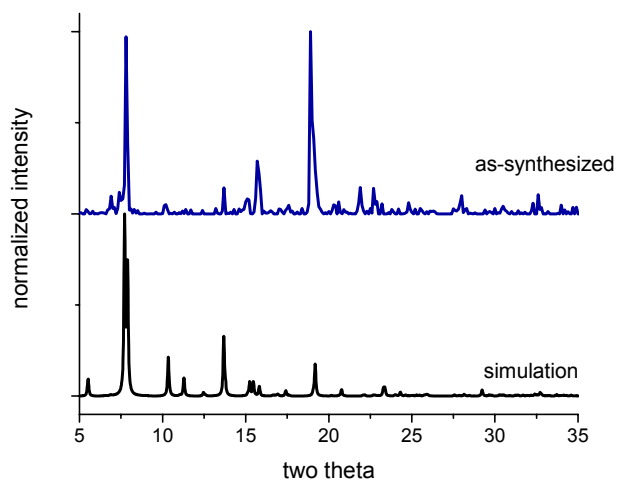
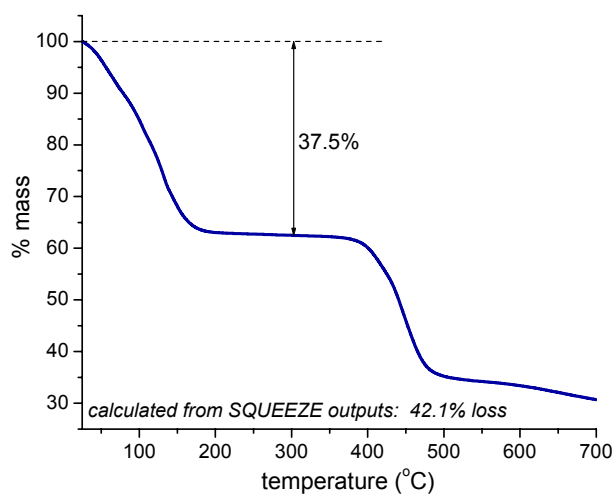
**A****B**

Figure 7.3. Characterization of bulk phase of **18** by (A) PXRD and (B) TGA.

7.3.2 Hydrogen adsorption of **18**

We initially targeted **18** as a material in which to study the effects framework reduction and cation doping on H₂ uptake and binding, since the inclusion of **L2** endows MOF materials with redox activity (as detailed extensively in Chapters 3²⁶ and 4²⁵). The 77K H₂ adsorption and isosteric heat of adsorption of pristine **18** are presented in Figure 7.4. The uptake at 1 atm (1.29 wt%) is comparable to other Zn(II) pillared paddlewheels. Like other MOF materials, the isosteric heat of adsorption reflects the heterogeneous nature of the surface, decreasing from 6.3 kJ/mol at zero loading to 2.4 kJ/mol at maximum loading. The framework reduction and cation doping of **18** was not comprehensively pursued although the **L2** strut is easily reduced by any number of redox agents. However, in this case, the interpenetration in the structure completely conceals the face of the **L2** strut, the most probable location for an accompanying extraframework cation. This structural aspect of **18**, coupled with the interpenetration, does not provide a structure in which to create and observe direct H₂-cation interactions.

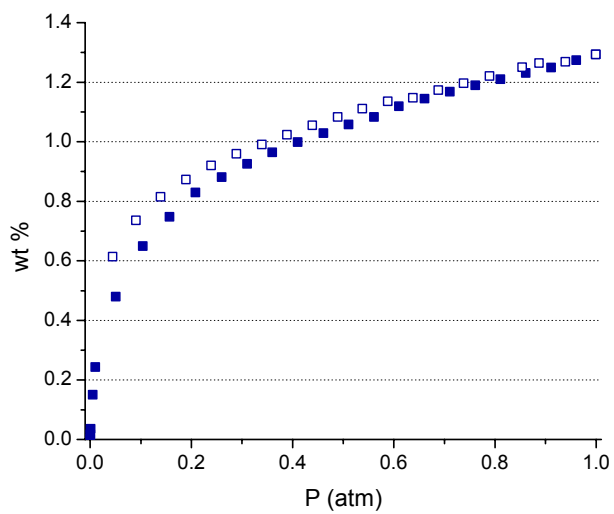
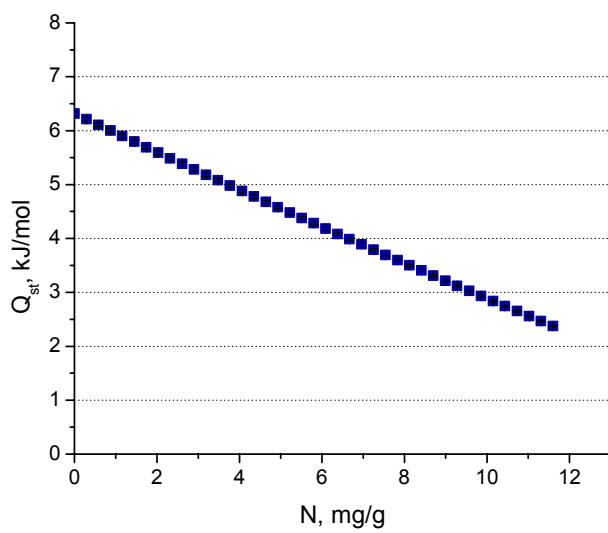
**A****B**

Figure 7.4. A) 77K H_2 adsorption and B) isosteric heat of adsorption of **18**.

7.3.3 Nitrogen and argon adsorption of **18**

The measurement of N₂ adsorption at 77K is a routine characterization technique for porous materials to extract structural data such as surface area, pore volume and pore size distribution.²⁹ Perhaps most importantly for MOF materials, N₂ isotherms verify the permanent porosity of these structures upon removal of guest solvents found in the pores upon crystallization. These isotherms can generally be classified as Type I, indicative of microporosity where the pores are filled very quickly at extremely low-pressure values. At first glance, the N₂ adsorption isotherm of activated **18** appears to be a typical Type I isotherm with a BET surface area of 751 m²/g (Figure 7.5). But upon closer inspection of the very low-pressure region a very unusual step is observed at $P/P_0 \sim 0.003$, which we will term the “gate pressure”. Stepped N₂ adsorption is not unprecedented, in fact the rare IUPAC Type VI isotherm does account for layered adsorption in porous solids and results in a stepped isotherm with no hysteresis. Conversely, the N₂ isotherm of **18** has effectively *no* adsorption until the gate pressure as opposed to an adsorbate layering behavior.

Gated N₂ adsorption as seen in **18** is quite peculiar behavior. There has only been one other example that displays virtually no initial adsorption followed by sharp uptake, observed in a two-dimensional coordination polymer where the gate “opening” is attributed to the breaking of hydrogen bonds between the layers.³⁰ At the gate pressure, the adsorbate pressure is strong enough to overcome the relatively weak hydrogen bonding and permit access to between the layers and around counterions in the structure. Notably, the structure observed crystallographically did not display any significant porosity. On the contrary, **18** is a three-dimensional framework whose crystal structure possesses large channel-like pores in two

directions (see Figure 7.2 and discussion above). N₂ gating behavior has been observed in three-dimensional framework structures, but only at substantially higher temperature and pressure.¹⁸

The gating behavior in the N₂ isotherm prompted us to examine this material by Ar adsorption as well, shown in Figure 7.6. Ar adsorption at 87K displays gating behavior much like the N₂ isotherm; practically no adsorption is observed until the gate pressure and subsequent dramatic uptake to give a BET surface area of 499 m²/g. It is noteworthy that the gate pressure for Ar is about an order of magnitude higher than that for N₂ ($P/P_o(\text{Ar}) \sim 0.05$, $P/P_o(\text{N}_2) \sim 0.003$). The BET surface area returned from the Ar isotherm is significantly lower than that from the N₂ isotherm (499 m²/g vs. 751 m²/g), but the appropriate analyses could not be performed in the same range as a result of the isotherm step.

The considerable difference in gate pressure between these two generally benign adsorbates indicates that fluid-fluid interactions are not the dominant factor that induces the gate opening mechanism. Additionally, the gate opening mechanism is not influenced by adsorbate size that is able to squeeze past and open the “gate”, as Ar has a smaller kinetic diameter than N₂, 3.4 and 3.64 Å, respectively.³¹ A possible explanation for the distinct difference between N₂ and Ar could be that fluid-*framework* interactions are the primary cause for the position of the gate pressure. The quadrupole moment of N₂ can favorably interact with the heterogeneous and highly polarizable framework structure, whereas Ar does not have a quadrupole moment and must amass a greater pressure on the exterior of the framework to “open” the gate.

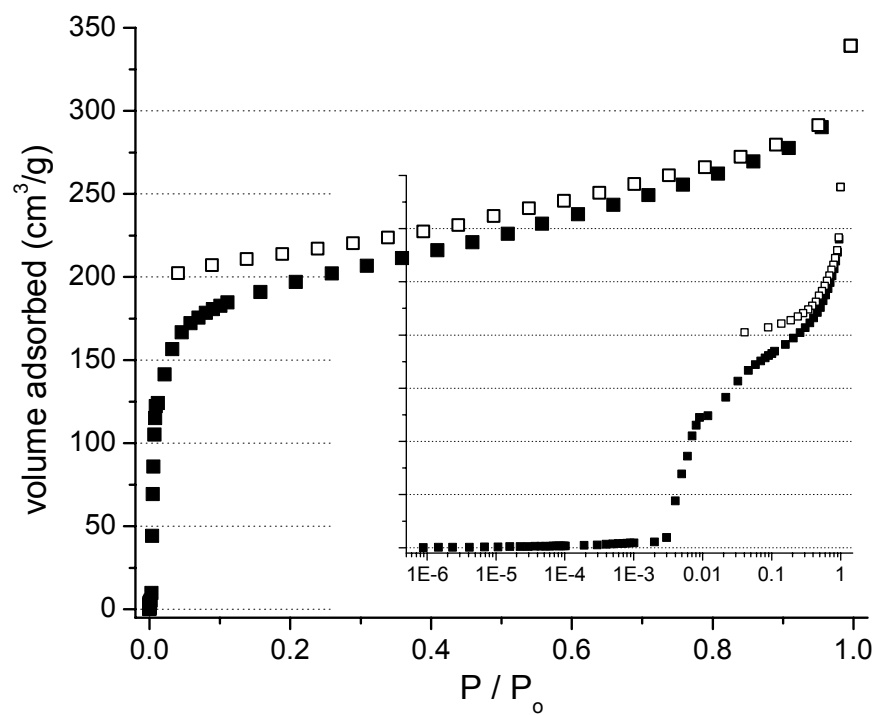


Figure 7.5. N₂ adsorption isotherm of **18**. Closed symbols, adsorption; open symbols, desorption. Inset depicts adsorption/desorption on a log scale.

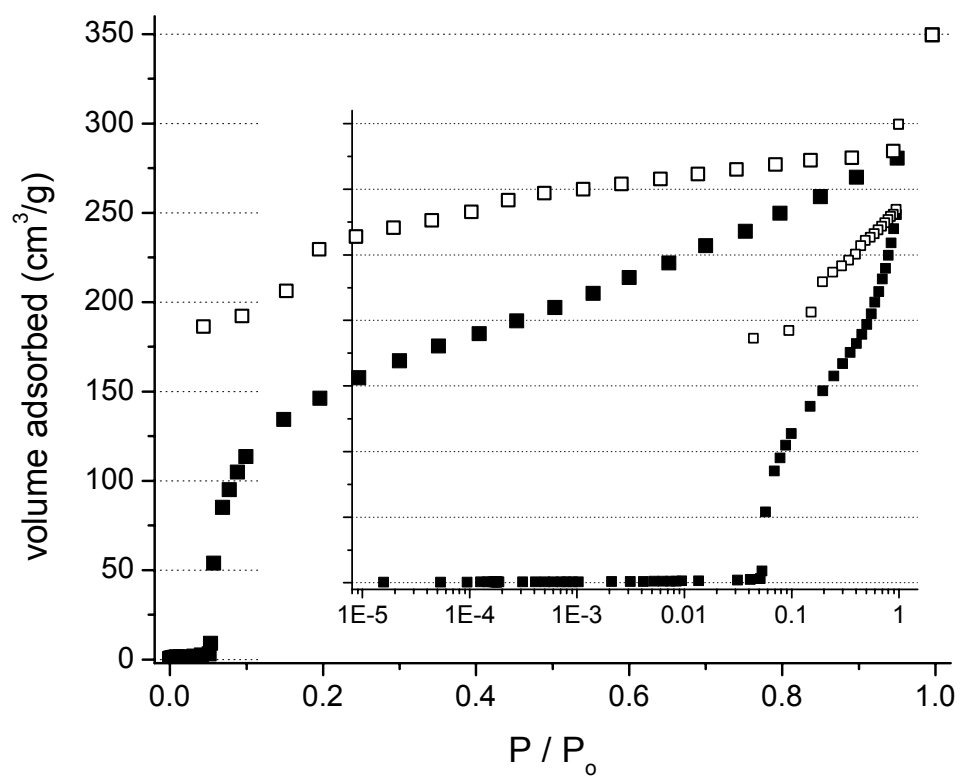


Figure 7.6. Ar adsorption isotherm of **18** at 87K. Closed symbols, adsorption; open symbols, desorption. Inset depicts adsorption/desorption on a log scale.

7.3.4 Low-pressure CO₂ adsorption of **18**

In addition to nitrogen and argon adsorption, CO₂ is becoming more routinely employed as an adsorbate in the characterization of porous materials.³² Since CO₂ adsorption is generally performed at higher temperatures than nitrogen or argon (273K as opposed to 77K or 87K), its kinetic energy is greater than the more traditional adsorbates and it can often access more surface area and pore volume. Moreover, at 273K, structures prone to dynamic behavior in the solid state should be more receptive to incoming adsorbate molecules than at cryogenic temperatures. The CO₂ isotherm of **18** at 273K up to 1 atm is presented in Figure 7.7. The step in the isotherm at ~0.5 atm is highly unusual, but not unprecedented. Stepped CO₂ isotherms have been observed in high-pressure experiments as well as computationally modeled in the IRMOF structures.³³ In these examples of stepped CO₂ adsorption, the large step in the isotherm is attributed to attractive CO₂-CO₂ interactions within the framework pores accompanied by a large and abrupt increase in adsorbate density which then approaches the density of liquid CO₂. However, hysteresis on the desorption curve was not observed in the experiments or in the simulations. Notably, the hysteresis is repeatable and not a function of incomplete instrument equilibration, see Figure 7.8.

The atypical CO₂ adsorption behavior at 273K encouraged us to measure the isotherm at several temperatures, shown in Figure 7.9. The adsorption step and hysteresis moves to lower absolute pressure and is much broader at lower temperatures. Looking first at only the 273K isotherm, it is difficult to judge if the jump in uptake is an effect of pore condensation or a true step in the isotherm. However, the isotherm measured at 263K clearly displays a leveling behavior at 1 atm which appears to be approaching a plateau in the uptake. In the isotherms that display the step and hysteresis, the hysteresis loop is fully closed to rejoin the adsorption branch;

all of the adsorbate molecules can be removed from the framework. Noticeably, at 298K, the adsorption step and hysteresis is not observed before the limit of these measurements. Plotting the adsorbed volume as a function of *relative* pressure (Figure 7.10) rather than absolute pressure reveals that we simply have not reached the relative pressure necessary to observe the stepped adsorption behavior at elevated temperatures.

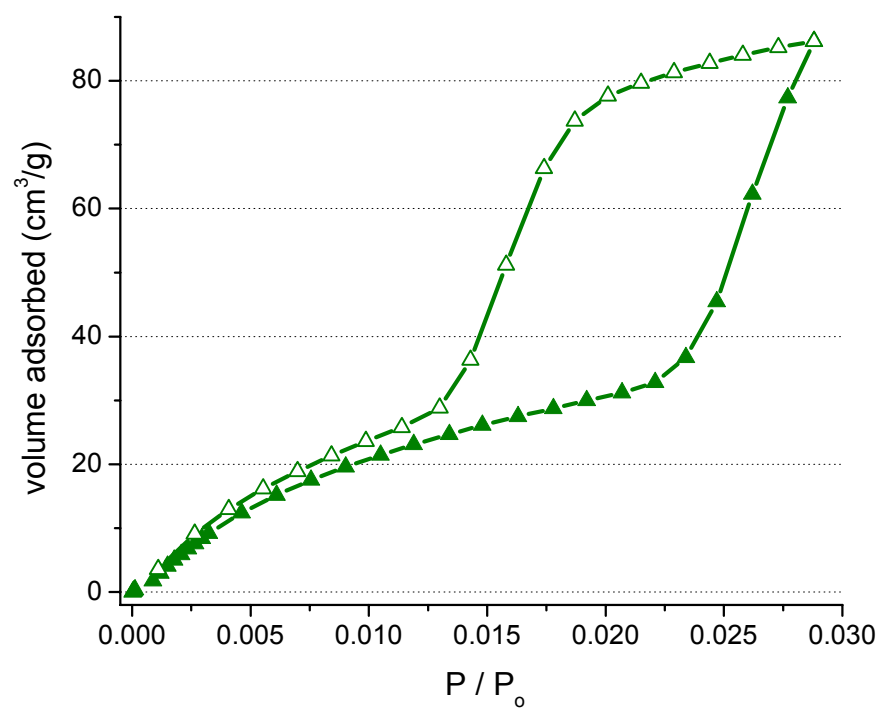
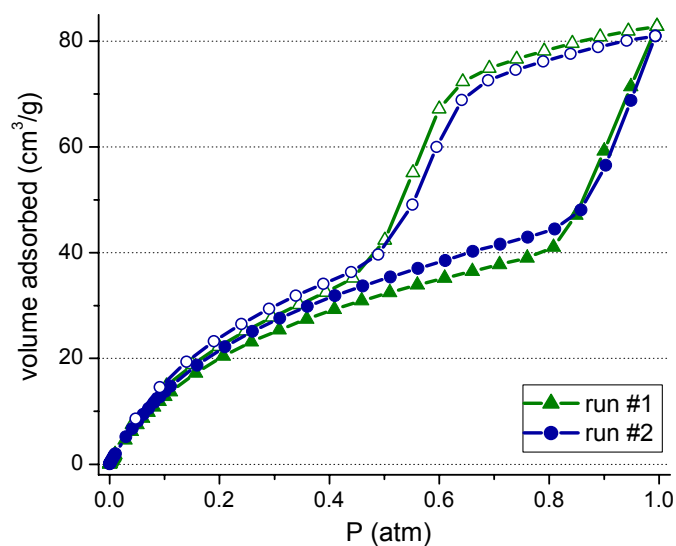
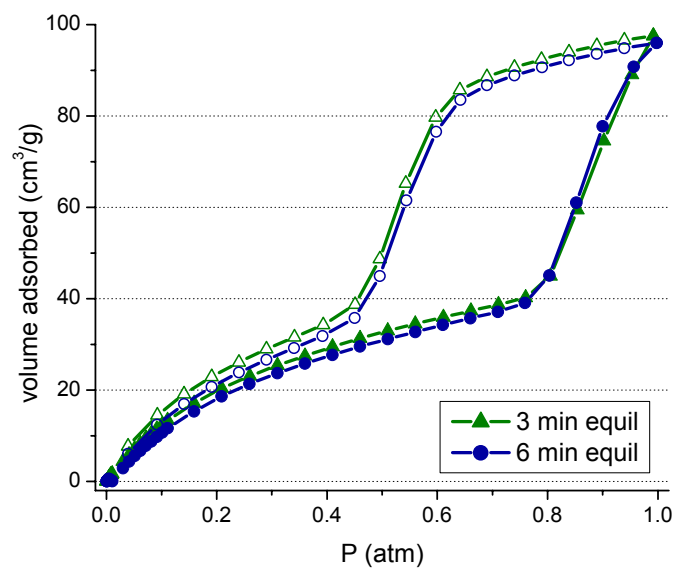


Figure 7.7. 273K CO₂ adsorption isotherm of **18**. Closed symbols, adsorption; open symbols, desorption. Lines connecting data points are intended to guide the eye.



A



B

Figure 7.8. 273K CO₂ adsorption isotherms of **18**. A) Back-to-back adsorption/desorption isotherms. B) Increase of equilibration time to verify width of hysteresis.

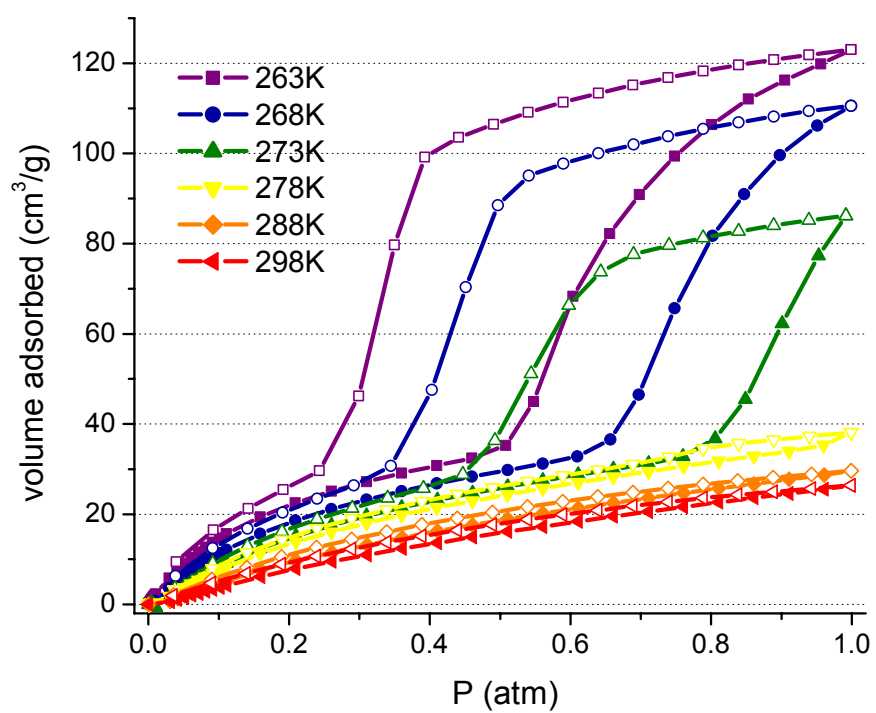


Figure 7.9. Low pressure CO₂ isotherms of **18** at various temperatures. Lines connecting data points are intended to guide the eye.

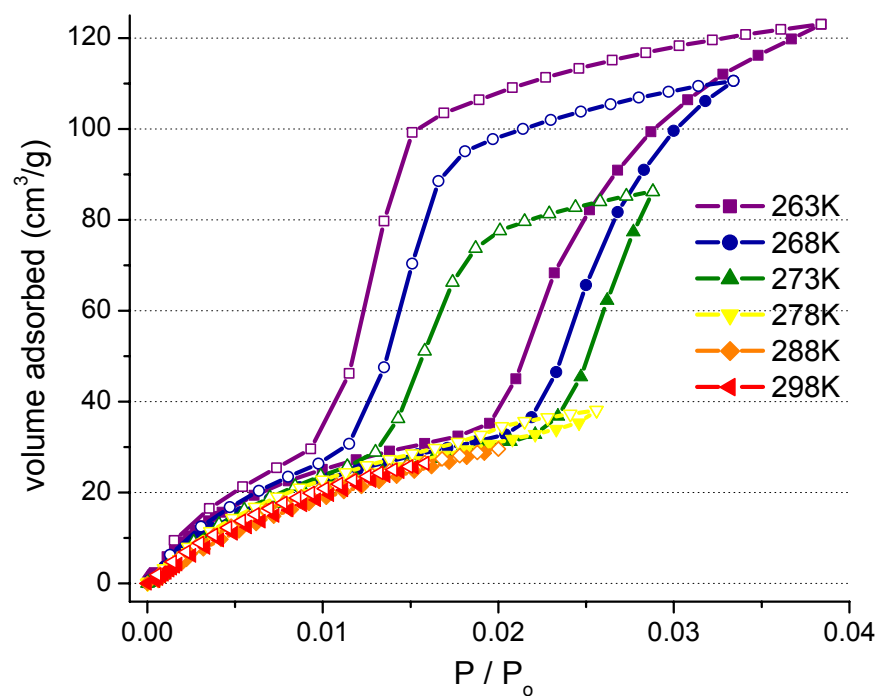


Figure 7.10. CO₂ adsorption of **18** at various temperatures as a function of relative pressure. Closed symbols, adsorption; open symbols, desorption. Lines connecting data points are intended to guide the eye.

7.3.5 High-pressure CO₂ adsorption of **18**

Ultra-high capacity CO₂ uptake has been demonstrated in several MOF structures and is of immense technological interest for CO₂ storage and sequestration.³⁴⁻³⁸ Additionally, a solid-state material that can selectively adsorb CO₂ in a mixture of other adsorbates such as CH₄ or N₂ has vast potential in separations, perhaps most relevant for flue gas decontamination. The hysteretic adsorption described in the previous section could provide a mechanism by which to selectively adsorb CO₂ from gas mixtures. To examine the CO₂ adsorption behavior of **18** at more technologically relevant conditions, we performed high-pressure CO₂ adsorption at various temperatures, Figure 7.11. Since the first pressure point (~1 bar) is already past the step pressure at 273K (~0.75 bar), the isotherm appears to be typically Type I, with slight hysteresis. (Unfortunately, our current equipment does not allow the collection of pressure points at intervals more frequent than approximately every 2 bar, so we were not able to suitably resolve the hysteresis behavior.) The high-pressure CO₂ adsorption isotherms at higher temperatures did indeed exhibit stepped adsorption, seen most clearly in the 318K and 328K isotherms. Like the low-pressure results, the position of the adsorption step is temperature dependent. This unusual stepped adsorption and hysteretic desorption, even at moderate pressures, has potential utility in separation processes.

The maximum loading at 298K, almost 120 cm³/g, corresponds to 5.6 mmol CO₂/g MOF. Admittedly, this is much lower than the highest CO₂ uptake reported for MOF materials.^{35,36} The total uptake of **18** is undoubtedly hindered by the two-fold interpenetration. However, the interpenetrated networks that occupy pore volume and ultimately reduce total uptake most likely initiate the stepped adsorption and hysteresis in the CO₂ isotherms and the gated behavior in the N₂ and Ar isotherms.

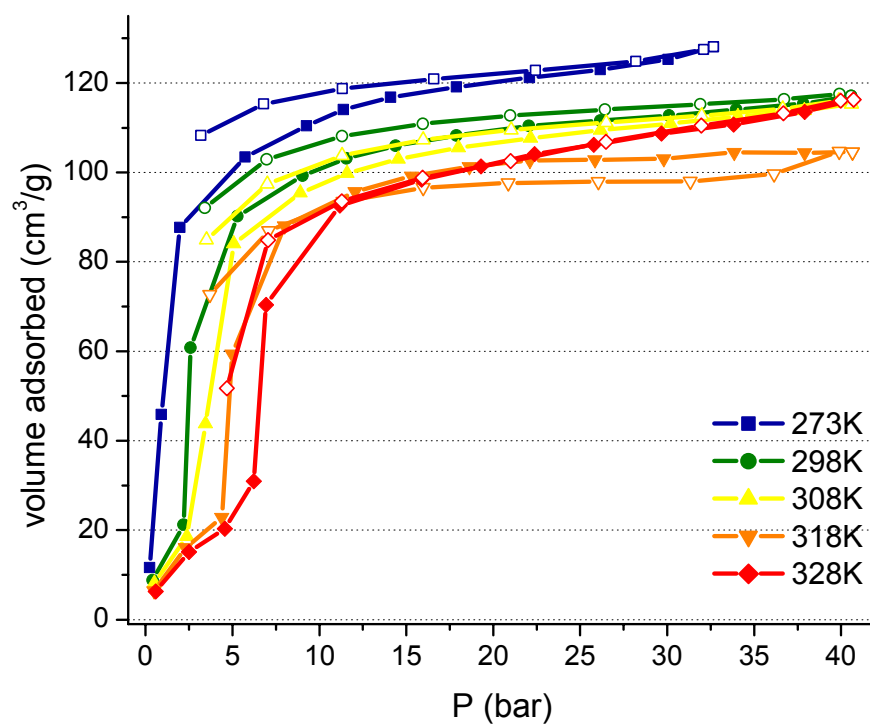


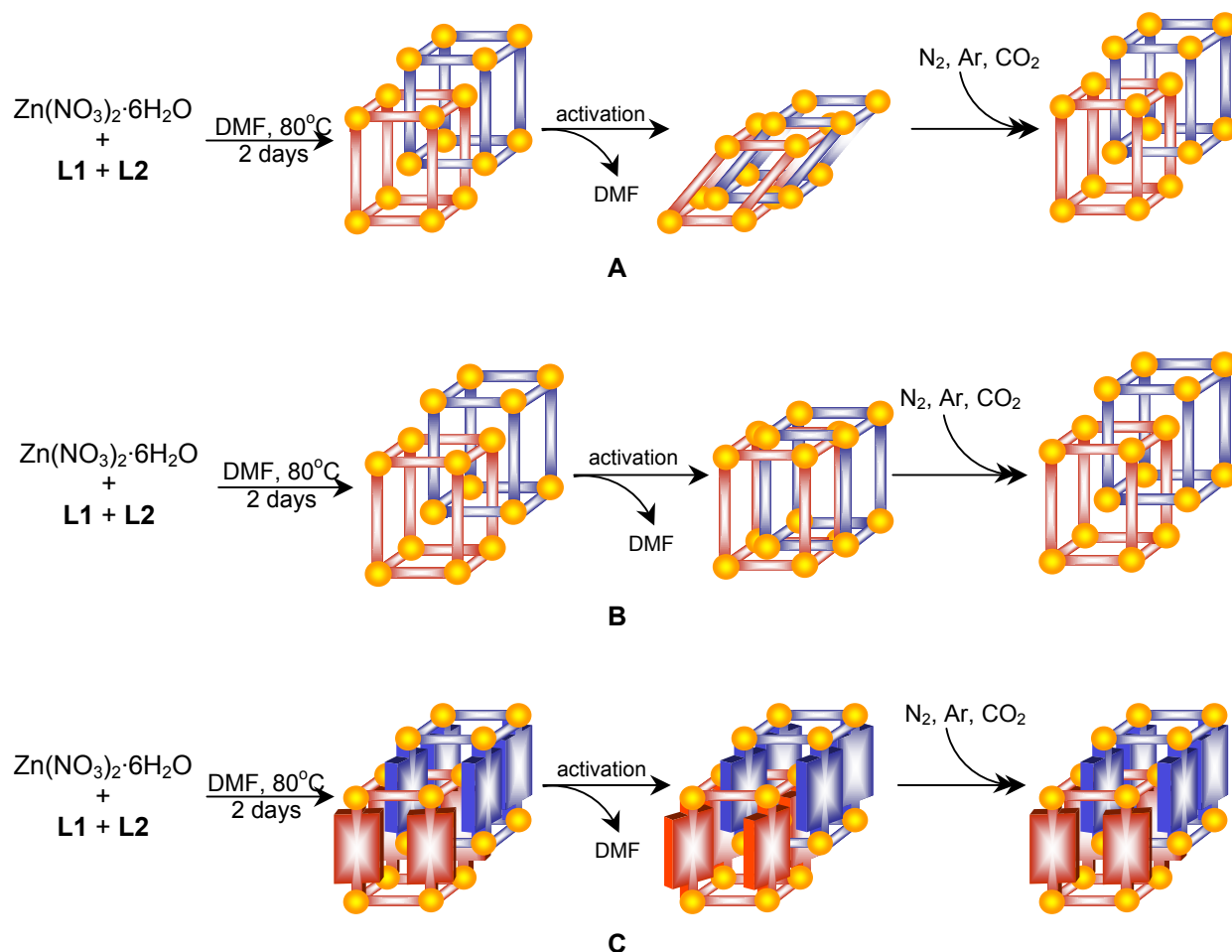
Figure 7.11. High-pressure CO₂ adsorption of **18**. Closed symbols, adsorption; open symbols, desorption. Lines connecting data points are intended to guide the eye.

7.3.6 Discussion of structural effects on adsorption behavior

The clear and broad hysteresis shown in Figure 7.7 is generally taken to be an indication of the presence of mesopores, as in the IUPAC Type IV isotherm classification. The step in the adsorption branch of the isotherm in mesoporous materials results from capillary condensation within the pores near the saturation pressure. This behavior is quite well understood for adsorption of N₂ and Ar adsorption at 77K and 87K up to 1 atmosphere where the top of the isotherm represents adsorbate saturation. By contrast, the pressure at which we observe the step and hysteresis in the CO₂ isotherm is far below the saturation pressure (34.3 atm at 273K), apparent in the high-pressure isotherms in Figure 7.11. Similar behavior has been observed in the nitrogen adsorption in a two-dimensional framework material³⁹ and a three-dimensional pillared paddlewheel structure.^{19,40} PXRD analysis of the structure under the isotherm conditions was employed to “watch” the dynamic behavior through the adsorption/desorption cycle.

A distinct step in CO₂ adsorption isotherms has been observed and accurately modeled in the IRMOF series.³³ In this case, the step in the isotherm is attributed to strong CO₂-CO₂ interactions within the framework pores. It is notable that these calculations accurately captured the step in the isotherm using only a *rigid* model for the frameworks, as opposed to one that is flexible and can structurally respond to incoming adsorbates. However, neither the experiments nor the calculations reported hysteresis upon desorption, which is clearly apparent in the CO₂ isotherms of **18** at each temperature point from 263K to 328K.

Dynamic framework behavior responsible for the stepped CO₂ adsorption as well as gated N₂ and Ar adsorption could conceivably take several different forms: 1) reversible framework collapse upon activation, 2) frameworks shifting between interpenetrated and interwoven, or 3) ligand rotation gating adsorption/desorption, see Scheme 7.1.



Scheme 7.1 Potential dynamic structural behavior of **18** upon framework synthesis, activation, and guest adsorption. A) Reversible framework collapse. B) Interpenetrated structure formed during synthesis; interwoven structure on removal of solvents to maximize framework-framework interactions; interpenetrated structure reformed on introduction of gaseous adsorbate. C) Ligand rotation upon removal of solvents to block pore access and further rotation on introduction of gaseous adsorbate.

Reversible framework collapse, Scheme 7.1a, is a plausible explanation for the behavior observed in the N₂ and Ar isotherms. From the N₂ isotherm (Figure 7.5), the pore volume and surface area calculated before the step, or gate, ($P/P_0 = 0.002$) are 0.0084 cm³/g and 29 m²/g, respectively, both suggest only external surface adsorption and no accessible internal surface area. However, after the gate pressure, the BET surface area is 751 m²/g and the pore volume at $P/P_0 = 0.95$ is 0.45 cm³/g, which are more typical for a microporous material as seen in the crystal structure of **18**. If the N₂ and Ar adsorption isotherms were the only structural characterization available, this would probably be the prevailing hypothesis of the dynamic structural behavior in **18**. However, the CO₂ adsorption isotherms do display significant initial uptake, which discounts this pathway somewhat.

The CO₂ adsorption isotherms shown in Figure 7.7 can be viewed as an approximate sum of two Langmuir isotherms, one that follows the adsorption branch and the other along the desorption branch, Figure 7.12. The surface area obtained from a simple Langmuir⁴¹ fit to the adsorption branch of the isotherm is 335 m²/g, that obtained from the desorption branch is 691 m²/g. (Note: NLDFIT analysis of the 273K CO₂ isotherm from $0 < P < 0.75$ atm gives a surface area value of 339 m²/g, in excellent agreement with the Langmuir fit.) The surface area value returned from the adsorption branch of the CO₂ isotherm indicates that there is substantial CO₂-accessible internal surface area. Also, the roughly doubling of the surface area on the desorption branch suggests that mechanism #2 in Scheme 7.1 is an adequate explanation for the CO₂ adsorption. Upon complete removal of guest solvent molecules, it is not unrealistic for the frameworks to shift towards each other to become *interwoven* (recall the crystal structure is fully *interpenetrated*) and maximize favorable framework-framework van der Waals interactions. Re-

introducing framework guests (in this case, CO₂ molecules, but potentially also N₂ and Ar), can restore the frameworks to the as-synthesized interpenetrated configuration.

The third possible mechanism outlined in Scheme 7.1, ligand rotation in the frameworks to initiate a gate effect under the isotherm conditions, will require substantially more in-depth structural characterization to detect. However, research groups interested in investigating MOFs for molecular-rotor applications have recently employed a suite of solid-state NMR techniques⁴² and dielectric spectroscopy⁴³ to monitor ligand dynamics within the solid frameworks. Additionally, the development of a flexible framework model⁴⁴ may be able to capture ligand dynamics and framework-adsorbate interactions that play an important role in the adsorption characteristics.

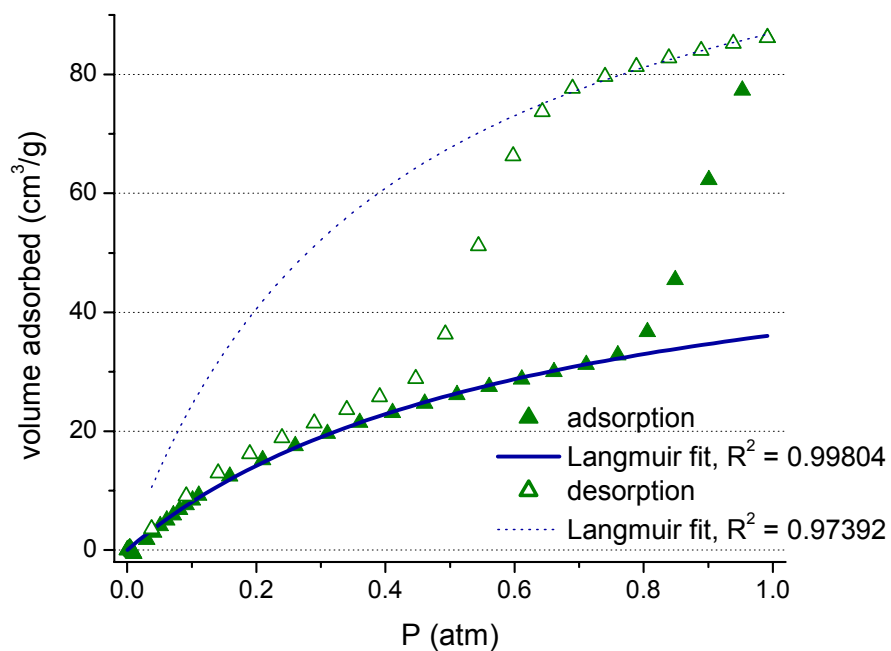


Figure 7.12. 273K CO₂ adsorption of **18** and Langmuir fits to adsorption and desorption branches of isotherm. Langmuir fit to adsorption branch gives surface area of 335 m²/g; Langmuir fit to desorption branch gives surface area of 691 m²/g.

7.4 Conclusions

While not entirely unprecedented, the adsorption behavior of **18** described here is quite uncommon in crystalline materials and not terribly well understood yet. The gating behavior observed in the N₂ and Ar isotherms has not previously been reported at low pressures for a three-dimensional MOF structure. Additionally, the CO₂ isotherms display stepped adsorption and hysteresis which has been observed at high pressures in MOF materials (generally above 5 – 10 bar) but this adsorption event begins much earlier in **18**, near $P/P_0 \sim 0.02$, or approximately 0.5 – 2 bar for all temperatures studied here. Taken all together, the adsorption results suggest dynamic framework behavior upon solvent removal (activation) and introduction of adsorbate molecules. Although the total CO₂ uptake of **18** cannot compete with the best-known MOFs, the hysteretic behavior could provide an interesting solution to safe and effective gas storage concerns.

Solely from the adsorption isotherm analysis presented in this chapter, a mechanism of structural behavior cannot be definitively identified. The N₂/Ar isotherms suggest reversible framework collapse or pore obstruction and the CO₂ data indicate that there is significant internal surface area available, even after complete activation. The differences between these three adsorbates could be largely due to specific fluid-framework interactions though, where the quadrupole moment of CO₂ can interact more strongly with the heterogeneous and highly polarizable framework than N₂ or Ar. Continuing structural characterization to identify the mechanism of adsorption will include PXRD analysis under the exact CO₂ isotherm conditions, VT-CPMAS solid state ¹³C NMR, and the development of a flexible model of **18** to visualize framework movements and adsorbate siting.

Notwithstanding the precise mechanism of adsorption of **18**, flexible frameworks such as this will continue to offer further tunability in solid framework materials with the ability to address exceptionally precise technological needs. However, the underlying mechanisms and interactions behind this flexibility in the solid state should be first characterized through a combination of adsorption techniques, traditional characterization methods applied to new materials, and molecular modeling. As technological requirements demand more specificity in materials properties, solid framework materials with the ability to demonstrate flexibility upon guest removal and adsorption will no doubt enjoy immense attention as solutions in selective adsorption or as highly responsive analyte sensors.

Chapter 1 References

- (1) Lewis, N. S. *MRS Bulletin* **2007**, 32, 808-820.
- (2) Schiermeier, Q.; Tollefson, J.; Scully, T.; Witze, A.; Morton, O. *Nature* **2008**, 454, 816-823.
- (3) IPCC, 2007: Summary for Policymakers. In: *Climate Change 2007: The Physical Science Basis. Contribution of Working Group I to the Fourth Assessment Report of the Intergovernmental Panel on Climate Change*. Cambridge University Press, Cambridge, United Kingdom and New York, NY, USA.
- (4) Zittel, Werner; Wurster, Reinhold. *Hydrogen in the Energy Sector*.
<http://www.hydrogen.org/Knowledge/w-i-energiew-eng.html>. (accessed September 1, 2008).
- (5) Crabtree, G. W.; Dresselhaus, M. S. *MRS Bulletin* **2008**, 33, 421-428.
- (6) *Hydrogen & Our Energy Future*; U.S. Department of Energy, 2007.
- (7) U.S. Department of Energy. *Hydrogen Production*.
http://www1.eere.energy.gov/hydrogenandfuelcells/production/natural_gas.html. (accessed September 1, 2008).
- (8) Lewis, N. S.; Nocera, D. G. *Proc. Natl. Acad. Sci.* **2006**, 103, 15729-15735.
- (9) Sanderson, K. *Nature* **2008**, 452, 400-403.
- (10) U.S. Department of Energy. *Hydrogen Delivery*.
http://www1.eere.energy.gov/hydrogenandfuelcells/delivery/current_technology.html. (accessed September 1, 2008).
- (11) Züttel, A. *Materials Today* **2003**, 6, 24-33.

- (12) Dillon, A. C.; Jones, K. M.; Bekkedahl, T. A.; Kiang, C. H.; Bethune, D. S.; Heben, M. J. *Nature* **1997**, *386*, 377-379.
- (13) Liu, C.; Fan, Y. Y.; Liu, M.; Cong, H. T.; Cheng, H. M.; Dresselhaus, M. S. *Science* **1999**, *286*, 1127-1129.
- (14) Froudakis, G. E. *Nano Letters* **2001**, *1*, 531-533.
- (15) Rowsell, J. L. C.; Yaghi, O. M. *Angew. Chem. Int. Ed.* **2005**, *44*, 4670-4679.
- (16) Lin, X.; Jia, J.; Hubberstey, P.; Schroder, M.; Champness, N. R. *CrystEngComm* **2007**, *9*, 438-448.
- (17) Collins, D. J.; Zhou, H.-C. *J. Mater. Chem.* **2007**, *17*, 3154-3160.
- (18) Dinca, M.; Long, J. R. *Ang. Chem. Int. Ed.* **2008**, *47*, 6766-6779.
- (19) Zhao, D.; Yuan, D.; Zhou, H.-C. *Energy Environ. Sci.* **2008**, *1*, 222-235.
- (20) Barcia, P. S.; Zapata, F.; Silva, J. A. C.; Rodrigues, A. E.; Chen, B. *J. Phys. Chem. B* **2007**, *111*, 6101-6103.
- (21) Chen, B. L.; Liang, C. D.; Yang, J.; Contreras, D. S.; Clancy, Y. L.; Lobkovsky, E. B.; Yaghi, O. M.; Dai, S. *Angew. Chem. Int. Ed.* **2006**, *45*, 1390-1393.
- (22) Bae, Y.-S.; Mulfort, K. L.; Frost, H.; Ryan, P.; Punnnathanam, S.; Broadbelt, L. J.; Hupp, J. T.; Snurr, R. Q. *Langmuir* **2008**, *24*, 8592-8598.
- (23) Cho, S.-H.; Ma, B.; Nguyen, S. T.; Hupp, J. T.; Albrecht-Schmitt, T. E. *Chem. Commun.* **2006**, 2563-2565.
- (24) Wu, C.-D.; Hu, A.; Zhang, L.; Lin, W. *J. Am. Chem. Soc.* **2005**, *127*, 8940-8941.
- (25) Seo, J. S.; Whang, D.; Lee, H.; Jun, S. I.; Oh, J.; Jeon, Y. J.; Kim, K. **2000**, *404*, 982-986.
- (26) James, S. L. *Chem. Soc. Rev.* **2003**, *32*, 276-288.
- (27) Kitagawa, S.; Kitaura, R.; Noro, S. *Angew. Chem. Int. Ed.* **2004**, *43*, 2334-2375.

- (28) Yaghi, O. M.; O'Keeffe, M.; Ockwig, N. W.; Chae, H. K.; Eddaoudi, M.; Kim, J. *Nature* **2003**, *423*, 705-714.
- (29) Eddaoudi, M.; Kim, J.; Rosi, N.; Vodak, D.; Wachter, J.; O'Keeffe, M.; Yaghi, O. M. *Science* **2002**, *295*, 469-472.
- (30) Frost, H.; Dueren, T.; Snurr, R. Q. *J. Phys. Chem. B* **2006**, *110*, 9565-9570.
- (31) Lin, X.; Jia, J.; Zhao, X.; Thomas, K. M.; Blake, A. J.; Walker, G. S.; Champness, N. R.; Hubberstey, P.; Schroeder, M. *Angew. Chem. Int. Ed.* **2006**, *45*, 7358-7364.
- (32) Ma, S. Q.; Sun, D. F.; Ambrogio, M.; Fillinger, J. A.; Parkin, S.; Zhou, H. C. *J. Am. Chem. Soc.* **2007**, *129*, 1858-1859.
- (33) Ryan, P.; Broadbelt, L. J.; Snurr, R. Q. *Chem. Commun.* **2008**, advance article.
- (34) Forster, P. M.; Eckert, J.; Heiken, B. D.; Parise, J. B.; Yoon, J. W.; Jhung, S. H.; Chang, J. S.; Cheetham, A. K. *J. Am. Chem. Soc.* **2006**, *128*, 16846-16850.
- (35) Dinca, M.; Dailly, A.; Liu, Y.; Brown, C. M.; Neumann, D. A.; Long, J. R. *J. Am. Chem. Soc.* **2006**, *128*, 16876-16883.
- (36) Kubas, G. J. *Proc. Natl. Acad. Sci.* **2007**, *104*, 6901-6907.
- (37) Dag, S.; Ozturk, Y.; Ciraci, S.; Yildirim, T. *Phys. Rev. B* **2005**, *72*, 155404.
- (38) Yildirim, T.; Iniguez, J.; Ciraci, S. *Phys. Rev. B* **2005**, *72*, 153403.
- (39) Han, S. S.; Goddard, W. A., III *J. Am. Chem. Soc.* **2007**, *129*, 8422-8423.
- (40) Blomqvist, A.; Araujo, C. M.; Srepusharawoot, P.; Ahuja, R. *Proc. Natl. Acad. Sci. U. S. A.* **2007**, *104*, 20173-20176.

Chapter 2 References

- (1) Bradshaw, D.; Claridge, J. B.; Cussen, E. J.; Prior, T. J.; Rosseinsky, M. J. *Acc. Chem. Res.* **2005**, *38*, 273-282.
- (2) Rowsell, J. L. C.; Yaghi, O. M. *Micro. Meso. Mater.* **2004**, *73*, 3-14.
- (3) Kesanli, B.; Lin, W. B. *Coord. Chem. Rev.* **2003**, *246*, 305-326.
- (4) Kitagawa, S.; Kitaura, R.; Noro, S. *Angew. Chem. Int. Ed.* **2004**, *43*, 2334-2375.
- (5) Pan, L.; Sander, M. B.; Huang, X.; Li, J.; Smith, M.; Bittner, E.; Bockrath, B.; Johnson, J. K. *J. Am. Chem. Soc.* **2004**, *126*, 1308-1309.
- (6) Dybtsev, D. N.; Chun, H.; Yoon, S. H.; Kim, D.; Kim, K. *J. Am. Chem. Soc.* **2004**, *126*, 32-33.
- (7) Zhao, B.; Chen, X.-Y.; Cheng, P.; Liao, D.-Z.; Yan, S.-P.; Jiang, Z.-H. *J. Am. Chem. Soc.* **2004**, *126*, 15394-15395.
- (8) Chen, B.; Ma, S.; Hurtado, E. J.; Lobkovsky, E. B.; Liang, C.; Zhu, H.; Dai, S. *Inorg. Chem.* **2007**, *46*, 8705-8709.
- (9) Cho, S.-H.; Ma, B.; Nguyen, S. T.; Hupp, J. T.; Albrecht-Schmitt, T. E. *Chem. Commun.* **2006**, 2563-2565.
- (10) Fujita, M.; Kwon, Y. J.; Washizu, S.; Ogura, K. *J. Am. Chem. Soc.* **1994**, *116*, 1151-1152.
- (11) Rao, C. N. R.; Natarajan, S.; Vaidhyanathan, R. *Angew. Chem. Int. Ed.* **2004**, *43*, 1466-1496.
- (12) Yaghi, O. M.; O'Keeffe, M.; Ockwig, N. W.; Chae, H. K.; Eddaoudi, M.; Kim, J. *Nature* **2003**, *423*, 705-714.
- (13) Eddaoudi, M.; Kim, J.; Rosi, N.; Vodak, D.; Wachter, J.; O'Keeffe, M.; Yaghi, O. M. *Science* **2002**, *295*, 469-472.

- (14) Kitaura, R.; Iwahori, F.; Matsuda, R.; Kitagawa, S.; Kubota, Y.; Takata, M.; Kobayashi, T.
C. Inorg. Chem. **2004**, *43*, 6522-6524.
- (15) Dybtsev, D. N.; Chun, H.; Kim, K. *Ang. Chem. Int. Ed.* **2004**, *43*, 5033-5036.
- (16) Dinolfo, P. H.; Williams, M. E.; Stern, C. L.; Hupp, J. T. *J. Am. Chem. Soc.* **2004**, *126*, 12989-13001.
- (17) Withersby, M. A.; Blake, A. J.; Champness, N. R.; Cooke, P. A.; Hubberstey, P.; Li, W.-S.; Schroder, M. *Inorg. Chem.* **1999**, *38*, 2259-2266.
- (18) Ahrens, M. J.; Sinks, L. E.; Rybtchinski, B.; Liu, W.; Jones, B. A.; Giaimo, J. M.; Gusev, A. V.; Goshe, A. J.; Tiede, D. M.; Wasielewski, M. R. *J. Am. Chem. Soc.* **2004**, *126*, 8284-8294.
- (19) Farha, O. K.; Mulfort, K. L.; Thorsness, A. M.; Hupp, J. T. *J. Am. Chem. Soc.* **2008**, *130*, 8598-8599.
- (20) Spek, A. L. *J. App. Cryst.* **2003**, *36*, 7-13.
- (21) Czepirski, L.; Jagiello, J. *Chem. Eng. Sci.* **1989**, *44*, 797-801.
- (22) Li, H.; Eddaoudi, M.; O'Keeffe, M.; Yaghi, O. M. *Nature* **1999**, *402*, 276-279.
- (23) Braun, M. E.; Steffek, C. D.; Kim, J.; Rasmussen, P. G.; Yaghi, O. M. *Chem. Commun.* **2001**, 2532-2533.
- (24) Seki, K. *Phys. Chem. Chem. Phys.* **2002**, *4*, 1968-1971.
- (25) Kondo, A.; Noguchi, H.; Carlucci, L.; Proserpio, D. M.; Ciani, G.; Kajiro, H.; Ohba, T.; Kanoh, H.; Kaneko, K. *J. Am. Chem. Soc.* **2007**, *129*, 12362-12363.
- (26) Connelly, N. G.; Geiger, W. E. *Chem. Rev.* **1996**, *96*, 877-910.
- (27) Go, Y. B.; Wang, X.; Jacobson, A. J. *Inorg. Chem.* **2007**, *46*, 6594-6600.

- (28) Xue, M.; Ma, S.; Jin, Z.; Schaffino, R. M.; Zhu, G.-S.; Lobkovsky, E. B.; Qiu, S.-L.; Chen, B. *Inorg. Chem.* **2008**, *47*, 6825-6828.
- (29) Wurthner, F. *Chem. Commun.* **2004**, 1564-1579.
- (30) Gadzikwa, T.; Zeng, B.-S.; Hupp, J. T.; Nguyen, S. T. *Chem. Commun.* **2008**, 3672-3674.

Chapter 3 References

- (1) Rowsell, J. L. C.; Yaghi, O. M. *J. Am. Chem. Soc.* **2006**, *128*, 1304-1315.
- (2) Latroche, M.; Surble, S.; Serre, C.; Mellot-Draznieks, C.; Llewellyn, P. L.; Lee, J. H.; Chang, J. S.; Jhung, S. H.; Ferey, G. *Angew. Chem. Int. Ed.* **2006**, *45*, 8227-8231.
- (3) Ma, S.; Zhou, H.-C. *J. Am. Chem. Soc.* **2006**, *128*, 11734-11735.
- (4) Zhao, X. B.; Xiao, B.; Fletcher, A. J.; Thomas, K. M.; Bradshaw, D.; Rosseinsky, M. J. *Science* **2004**, *306*, 1012-1015.
- (5) Seo, J. S.; Whang, D.; Lee, H.; Jun, S. I.; Oh, J.; Jeon, Y. J.; Kim, K. *Nature* **2000**, *404*, 982-986.
- (6) Cho, S.-H.; Ma, B.; Nguyen, S. T.; Hupp, J. T.; Albrecht-Schmitt, T. E. *Chem. Commun.* **2006**, 2563-2565.
- (7) Zhao, B.; Chen, X.-Y.; Cheng, P.; Liao, D.-Z.; Yan, S.-P.; Jiang, Z.-H. *J. Am. Chem. Soc.* **2004**, *126*, 15394-15395.
- (8) Wong-Foy, A. G.; Matzger, A. J.; Yaghi, O. M. *J. Am. Chem. Soc.* **2006**, *128*, 3494-3495.
- (9) Dinca, M.; Dailly, A.; Liu, Y.; Brown, C. M.; Neumann, D. A.; Long, J. R. *J. Am. Chem. Soc.* **2006**, *128*, 16876-16883.
- (10) Schlapbach, L.; Züttel, A. *Nature* **2001**, *414*, 353-358.
- (11) "Hydrogen, Fuel Cells and Infrastructure Technologies Program," U.S. Department of Energy, 2003.
- (12) Ma, B. Q.; Mulfort, K. L.; Hupp, J. T. *Inorg. Chem.* **2005**, *44*, 4912-4914.
- (13) Dinolfo, P. H.; Williams, M. E.; Stern, C. L.; Hupp, J. T. *J. Am. Chem. Soc.* **2004**, *126*, 12989-13001.
- (14) Seki, K. *Phys. Chem. Chem. Phys.* **2002**, *4*, 1968-1971.

- (15) Maji, T. K.; Matsuda, R.; Kitagawa, S. *Nature Materials* **2007**, *6*, 142-148.
- (16) Uemura, K.; Matsuda, R.; Kitagawa, S. *J. Solid State Chem.* **2005**, *178*, 2420-2429.
- (17) Chen, B.; Ma, S.; Hurtado, E. J.; Lobkovsky, E. B.; Liang, C.; Zhu, H.; Dai, S. *Inorg. Chem.* **2007**, *46*, 8705-8709.
- (18) Dinca, M.; Han, W. S.; Liu, Y.; Dailly, A.; Brown, C. M.; Long, J. R. *Angew. Chem., Int. Ed.* **2007**, *46*, 1419-1422.
- (19) Forster, P. M.; Eckert, J.; Heiken, B. D.; Parise, J. B.; Yoon, J. W.; Jhung, S. H.; Chang, J. S.; Cheetham, A. K. *J. Am. Chem. Soc.* **2006**, *128*, 16846-16850.

Chapter 4 References

- (1) Schlapbach, L.; Züttel, A. *Nature* **2001**, *414*, 353-358.
- (2) Collins, D. J.; Zhou, H.-C. *J. Mater. Chem.* **2007**, *17*, 3154-3160.
- (3) Furukawa, H.; Miller, M. A.; Yaghi, O. M. *J. Mater. Chem.* **2007**, *17*, 3197-3204.
- (4) Wong-Foy, A. G.; Matzger, A. J.; Yaghi, O. M. *J. Am. Chem. Soc.* **2006**, *128*, 3494-3495.
- (5) Lochan, R. C.; Head-Gordon, M. *Phys. Chem. Chem. Phys.* **2006**, *8*, 1357-1370.
- (6) Bhatia, S. K.; Myers, A. L. *Langmuir* **2006**, *22*, 1688-1700.
- (7) Dinca, M.; Long, J. R. *J. Am. Chem. Soc.* **2007**, *129*, 11172-11176.
- (8) Mulfort, K. L.; Hupp, J. T. *J. Am. Chem. Soc.* **2007**, *129*, 9604-9605.
- (9) Ma, B. Q.; Mulfort, K. L.; Hupp, J. T. *Inorg. Chem.* **2005**, *44*, 4912-4914.
- (10) Belof, J. L.; Stern, A. C.; Eddaoudi, M.; Space, B. *J. Am. Chem. Soc.* **2007**, *129*, 15202-15210.
- (11) Liu, Y.; Eubank, J. F.; Cairns, A. J.; Eckert, J.; Kravtsov, V. C.; Luebke, R.; Eddaoudi, M. *Angew. Chem., Int. Ed.* **2007**, *46*, 3278-3283.
- (12) Connelly, N. G.; Geiger, W. E. *Chem. Rev.* **1996**, *96*, 877-910.
- (13) Czepirski, L.; Jagiello, J. *Chem. Eng. Sci.* **1989**, *44*, 797-801.
- (14) Yildirim, T.; Iniguez, J.; Ciraci, S. *Phys. Rev. B* **2005**, *72*, 153403.
- (15) Dag, S.; Ozturk, Y.; Ciraci, S.; Yildirim, T. *Phys. Rev. B* **2005**, *72*, 155404.
- (16) Han, S. S.; Goddard, W. A., III *J. Am. Chem. Soc.* **2007**, *129*, 8422-8423.
- (17) Blomqvist, A.; Araujo, C. M.; Srepusharawoot, P.; Ahuja, R. *Proc. Natl. Acad. Sci. U. S. A.* **2007**, *104*, 20173-20176.
- (18) Dalach, P.; Frost, H.; Snurr, R. Q.; Ellis, D. E. *J. Phys. Chem. C* **2008**, *112*, 9278-9284.

- (19) Mavrandonakis, A.; Tylianakis, E.; Stubos, A. K.; Froudakis, G. E. *J. Phys. Chem. C* **2008**, *112*, 7290-7294.
- (20) Maji, T. K.; Matsuda, R.; Kitagawa, S. *Nature Materials* **2007**, *6*, 142-148.
- (21) Kondo, A.; Noguchi, H.; Carlucci, L.; Proserpio, D. M.; Ciani, G.; Kajiro, H.; Ohba, T.; Kanoh, H.; Kaneko, K. *J. Am. Chem. Soc.* **2007**, *129*, 12362-12363.
- (22) Frost, H.; Dueren, T.; Snurr, R. Q. *J. Phys. Chem. B* **2006**, *110*, 9565-9570.
- (23) Dinca, M.; Han, W. S.; Liu, Y.; Dailly, A.; Brown, C. M.; Long, J. R. *Angew. Chem., Int. Ed.* **2007**, *46*, 1419-1422.
- (24) Kaye, S. S.; Long, J. R. *Chem. Commun.* **2007**, 4486-4488.
- (25) Farha, O. K.; Spokoyny, A. M.; Mulfort, K. L.; Hawthorne, M. F.; Mirkin, C. A.; Hupp, J. T. *J. Am. Chem. Soc.* **2007**, *129*, 12680-12681.
- (26) Ma, S.; Zhou, H.-C. *J. Am. Chem. Soc.* **2006**, *128*, 11734-11735.
- (27) Palomino, G. T.; Carayol, M. R. L.; Arean, C. O. *J. Mater. Chem.* **2006**, *16*, 2884-2885.

Chapter 5 References

- (1) James, S. L. *Chem. Soc. Rev.* **2003**, 32, 276-288.
- (2) Kitagawa, S.; Kitaura, R.; Noro, S. *Angew. Chem. Int. Ed.* **2004**, 43, 2334-2375.
- (3) Rowsell, J. L. C.; Yaghi, O. M. *Microporous Mesoporous Mater.* **2004**, 73, 3-14.
- (4) Collins, D. J.; Zhou, H.-C. *J. Mater. Chem.* **2007**, 17, 3154-3160.
- (5) Latroche, M.; Surble, S.; Serre, C.; Mellot-Draznieks, C.; Llewellyn, P. L.; Lee, J. H.; Chang, J. S.; Jhung, S. H.; Ferey, G. *Angew. Chem. Int. Ed.* **2006**, 45, 8227-8231.
- (6) Lin, X.; Jia, J.; Hubberstey, P.; Schroder, M.; Champness, N. R. *CrystEngComm* **2007**, 9, 438-448.
- (7) Furukawa, H.; Miller, M. A.; Yaghi, O. M. *J. Mater. Chem.* **2007**, 17, 3197-3204.
- (8) Dinca, M.; Dailly, A.; Liu, Y.; Brown, C. M.; Neumann, D. A.; Long, J. R. *J. Am. Chem. Soc.* **2006**, 128, 16876-16883.
- (9) Lin, X.; Jia, J.; Zhao, X.; Thomas, K. M.; Blake, A. J.; Walker, G. S.; Champness, N. R.; Hubberstey, P.; Schroeder, M. *Angew. Chem., Int. Ed.* **2006**, 45, 7358-7364.
- (10) Dybtsev, D. N.; Chun, H.; Yoon, S. H.; Kim, D.; Kim, K. *J. Am. Chem. Soc.* **2004**, 126, 32-33.
- (11) Ma, S. Q.; Sun, D. F.; Ambrogio, M.; Fillinger, J. A.; Parkin, S.; Zhou, H. C. *J. Am. Chem. Soc.* **2007**, 129, 1858-1859.
- (12) Dinca, M.; Han, W. S.; Liu, Y.; Dailly, A.; Brown, C. M.; Long, J. R. *Angew. Chem., Int. Ed.* **2007**, 46, 1419-1422.
- (13) Forster, P. M.; Eckert, J.; Heiken, B. D.; Parise, J. B.; Yoon, J. W.; Jhung, S. H.; Chang, J. S.; Cheetham, A. K. *J. Am. Chem. Soc.* **2006**, 128, 16846-16850.

- (14) Georgiev, P. A.; Albinati, A.; Mojet, B. L.; Ollivier, J.; Eckert, J. *J. Am. Chem. Soc.* **2007**, *129*, 8086-8087.
- (15) Farha, O. K.; Spokoyny, A. M.; Mulfort, K. L.; Hawthorne, M. F.; Mirkin, C. A.; Hupp, J. T. *J. Am. Chem. Soc.* **2007**, *129*, 12680-12681.
- (16) Mulfort, K. L.; Hupp, J. T. *J. Am. Chem. Soc.* **2007**, *129*, 9604-9605.
- (17) Mulfort, K. L.; Hupp, J. T. *Inorg. Chem.* **2008**, *47*, 7936-7938.
- (18) Ma, B. Q.; Mulfort, K. L.; Hupp, J. T. *Inorg. Chem.* **2005**, *44*, 4912-4914.
- (19) Cho, S.-H.; Ma, B.; Nguyen, S. T.; Hupp, J. T.; Albrecht-Schmitt, T. E. *Chem. Commun.* **2006**, 2563-2565.
- (20) Spek, A. L. *J. Appl. Crystallogr.* **2003**, *36*, 7-13.
- (21) Dinolfo, P. H.; Williams, M. E.; Stern, C. L.; Hupp, J. T. *J. Am. Chem. Soc.* **2004**, *126*, 12989-13001.
- (22) Connelly, N. G.; Geiger, W. E. *Chem. Rev.* **1996**, *96*, 877-910.
- (23) Dinca, M.; Long, J. R. *J. Am. Chem. Soc.* **2007**, *129*, 11172-11176.
- (24) Kaye, S. S.; Long, J. R. *J. Am. Chem. Soc.* **2005**, *127*, 6506-6507.
- (25) Kaye, S. S.; Long, J. R. *Chem. Commun.* **2007**, 4486-4488.
- (26) Lochan, R. C.; Head-Gordon, M. *Phys. Chem. Chem. Phys.* **2006**, *8*, 1357-1370.
- (27) Bhatia, S. K.; Myers, A. L. *Langmuir* **2006**, *22*, 1688-1700.
- (28) Czepirski, L.; Jagiello, J. *Chem. Eng. Sci.* **1989**, *44*, 797-801.
- (29) Rosi, N. L.; Eckert, J.; Eddaoudi, M.; Vodak, D. T.; Kim, J.; O'Keeffe, M.; Yaghi, O. M. *Science* **2003**, *300*, 1127-1129.
- (30) Yildirim, T.; Hartman, M. R. *Phys. Rev. Lett.* **2005**, *95*, 215504.
- (31) Han, S. S.; Goddard, W. A., III *J. Am. Chem. Soc.* **2007**, *129*, 8422-8423.

- (32) Blomqvist, A.; Araujo, C. M.; Srepusharawoot, P.; Ahuja, R. *Proc. Natl. Acad. Sci. U. S. A.* **2007**, *104*, 20173-20176.
- (33) Yildirim, T.; Iniguez, J.; Ciraci, S. *Phys. Rev. B* **2005**, *72*, 153403.
- (34) Dag, S.; Ozturk, Y.; Ciraci, S.; Yildirim, T. *Phys. Rev. B* **2005**, *72*, 155404.
- (35) Zhao, Y. F.; Kim, Y. H.; Dillon, A. C.; Heben, M. J.; Zhang, S. B. *Phys. Rev. Lett.* **2005**, *94*, 155504.
- (36) Walton, K. S.; Snurr, R. Q. *J. Am. Chem. Soc.* **2007**, *129*, 8552-8556.
- (37) Brunauer, S.; Emmett, P. H.; Teller, E. *J. Am. Chem. Soc.* **1938**, *60*, 309-319.
- (38) de Boer, J. H.; Linsen, B. G.; van der Plas, T.; Zondervan, G. J. *Journal of Catalysis* **1965**, *4*, 649-653.

Chapter 6 References

- (1) Collins, D. J.; Zhou, H.-C. *J. Mat. Chem.* **2007**, *17*, 3154-3160.
- (2) Lin, X.; Jia, J.; Hubberstey, P.; Schroder, M.; Champness, N. R. *CrystEngComm* **2007**, *9*, 438-448.
- (3) Rosi, N. L.; Eckert, J.; Eddaoudi, M.; Vodak, D. T.; Kim, J.; O'Keeffe, M.; Yaghi, O. M. *Science* **2003**, *300*, 1127-1129.
- (4) Schlappbach, L. *MRS Bulletin* **2002**, *27*, 675-676.
- (5) Lee, Y.-G.; Moon, H. R.; Cheon, Y. E.; Suh, M. P. *Angew. Chem.* **2008**, *early view*, DOI: 10.1002/anie.200801488.
- (6) Bhatia, S. K.; Myers, A. L. *Langmuir* **2006**, *22*, 1688-1700.
- (7) Dinca, M.; Long, J. R. *J. Am. Chem. Soc.* **2007**, *129*, 11172-11176.
- (8) Kaye, S. S.; Long, J. R. *Chem. Commun.* **2007**, 4486-4488.
- (9) Mulfort, K. L.; Hupp, J. T. *J. Am. Chem. Soc.* **2007**, *129*, 9604-9605.
- (10) Mulfort, K. L.; Hupp, J. T. *Inorg. Chem.* **2008**, *47*, 7936-7938.
- (11) Farha, O. K.; Mulfort, K. L.; Hupp, J. T. *Inorg. Chem.* **2008**, submitted.
- (12) Ma, B. Q.; Mulfort, K. L.; Hupp, J. T. *Inorg. Chem.* **2005**, *44*, 4912-4914.
- (13) Spek, A. L. *J. Appl. Cryst.* **2003**, *36*, 7-13.
- (14) Barbatti, M.; Jalbert, G.; Nascimento, M. A. C. *J. Chem. Phys.* **2001**, *114*, 2213-2218.
- (15) Han, S. S.; Goddard, W. A., III *J. Am. Chem. Soc.* **2007**, *129*, 8422-8423.
- (16) Blomqvist, A.; Araujo, C. M.; Srepusharawoot, P.; Ahuja, R. *Proc. Natl. Acad. Sci. U.S.A.* **2007**, *104*, 20173-20176.
- (17) Mavrandonakis, A.; Tylisanakis, E.; Stubos, A. K.; Froudakis, G. E. *J. Phys. Chem. C* **2008**, *112*, 7290-7294.

- (18) Klontzas, E.; Mavrandonakis, A.; Tylianakis, E.; Froudakis, G. E. *Nano Lett.* **2008**, *8*, 1572-1576.
- (19) Hanna, T. A.; Liu, L.; Angeles-Boza, A. M.; Kou, X.; Gutsche, C. D.; Ejsmont, K.; Watson, W. H.; Zakharov, L. N.; Incarvito, C. D.; Rheingold, A. L. *J. Am. Chem. Soc.* **2003**, *125*, 6228-6238.
- (20) Czepirski, L.; Jagiello, J. *Chem. Eng. Sci.* **1989**, *44*, 797-801.
- (21) Hu, X.; Skadtchenko, B. O.; Trudeau, M.; Antonelli, D. M. *J. Am. Chem. Soc.* **2006**, *128*, 11740-11741.
- (22) Hamaed, A.; Trudeau, M.; Antonelli, D. M. *J. Am. Chem. Soc.* **2008**, *130*, 6992-6999.
- (23) Hu, X.; Trudeau, M.; Antonelli, D. M. *Inorg. Chem.* **2008**, *47*, 2477-2484.
- (24) Kubas, G. J. *Proc. Natl. Acad. Sci.* **2007**, *104*, 6901-6907.
- (25) Palomino, G. T.; Carayol, M. R. L.; Arean, C. O. *J. Mater. Chem.* **2006**, *16*, 2884-2885.
- (26) Mavrandonakis, A.; Klopper, W. *J. Phys. Chem. C* **2008**, *112*, 11580-11585.
- (27) Belof, J. L.; Stern, A. C.; Eddaoudi, M.; Space, B. *J. Am. Chem. Soc.* **2007**, *129*, 15202-15210.
- (28) Lochan, R. C.; Head-Gordon, M. *Phys. Chem. Chem. Phys.* **2006**, *8*, 1357-1370.
- (29) Puurunen, R. L. *J. Appl. Phys.* **2005**, *97*.
- (30) Li, Y.; Yang, R. T. *J. Am. Chem. Soc.* **2006**, *128*, 726-727.
- (31) Li, Y.; Yang, R. T. *J. Am. Chem. Soc.* **2006**, *128*, 8136-8137.
- (32) Li, Y.; Yang, F. H.; Yang, R. T. *J. Phys. Chem. C* **2007**, *111*, 3405-3411.

Chapter 7 References

- (1) Férey, G. *Chem. Soc. Rev.* **2008**, *37*, 191-214.
- (2) Kitagawa, S.; Kitaura, R.; Noro, S. *Angew. Chem. Int. Ed.* **2004**, *43*, 2334-2375.
- (3) Kitagawa, S.; Uemura, K. *Chem. Soc. Rev.* **2005**, *34*, 109-119.
- (4) Serre, C.; Bourrelly, S.; Vimont, A.; Ramsahye, N. A.; Maurin, G.; Llewellyn, P. L.; Daturi, M.; Filinchuk, Y.; Leynaud, O.; Barnes, P.; Férey, G. *Adv. Mater.* **2007**, *19*, 2246-2251.
- (5) Llewellyn, P. L.; Bourrelly, S.; Serre, C.; Filinchuk, Y.; Férey, G. *Angew. Chem. Int. Ed.* **2006**, *45*, 7751-7754.
- (6) Serre, C.; Mellot-Draznieks, C.; Surble, S.; Audebrand, N.; Filinchuk, Y.; Férey, G. *Science* **2007**, *315*, 1828-1831.
- (7) Bourrelly, S.; Llewellyn, P. L.; Serre, C.; Millange, F.; Loiseau, T.; Férey, G. *J. Am. Chem. Soc.* **2005**, *127*, 13519-13521.
- (8) Choi, H. J.; Suh, M. P. *J. Am. Chem. Soc.* **2004**, *126*, 15844-15851.
- (9) Maji, T. K.; Mostafa, G.; Matsuda, R.; Kitagawa, S. *J. Am. Chem. Soc.* **2005**, *127*, 17152-17153.
- (10) Zhao, X. B.; Xiao, B.; Fletcher, A. J.; Thomas, K. M.; Bradshaw, D.; Rosseinsky, M. J. *Science* **2004**, *306*, 1012-1015.
- (11) Choi, H. J.; Dinca, M.; Long, J. R. *J. Am. Chem. Soc.* **2008**, *130*, 7848-7850.
- (12) Cussen, E.; Claridge, J. B.; Rosseinsky, M. J.; Kepert, C. J. *J. Am. Chem. Soc.* **2002**, *124*, 9574-9581.
- (13) Fletcher, A. J.; Cussen, E. J.; Prior, T. J.; Rosseinsky, M. J.; Kepert, C. J.; Thomas, K. M. *J. Am. Chem. Soc.* **2001**, *123*, 10001-10011.

- (14) Onishi, S.; Ohmori, T.; Ohkubo, T.; Noguchi, H.; Di, L.; Hanzawa, Y.; Kanoh, H.; Kaneko, K. *Appl. Surf. Sci.* **2002**, *196*, 81-88.
- (15) Tanaka, D.; Nakagawa, K.; Higuchi, M.; Horike, S.; Kubota, Y.; Kobayashi, T. C.; Takata, M.; Kitagawa, S. *Angew. Chem. Int. Ed.* **2008**, *47*, 3914-3918.
- (16) Uemura, K.; Matsuda, R.; Kitagawa, S. *J. Solid State Chem.* **2005**, *178*, 2420-2429.
- (17) Ma, S.; Sun, D.; Wang, X.-S.; Zhou, H.-C. *Angew. Chem. Int. Ed.* **2007**, *46*, 2458-2462.
- (18) Culp, J. T.; Smith, M. R.; Bittner, E.; Bockrath, B. *J. Am. Chem. Soc.* **2008**, *130*, 12427-12434.
- (19) Kitaura, R.; Akiyama, G.; Seki, K.; Kitagawa, S. *Angew. Chem. Int. Ed.* **2003**, *42*, 428-431.
- (20) Farha, O. K.; Mulfort, K. L.; Hupp, J. T. *Inorg. Chem.* **2008**, submitted.
- (21) Dinolfo, P. H.; Williams, M. E.; Stern, C. L.; Hupp, J. T. *J. Am. Chem. Soc.* **2004**, *126*, 12989-13001.
- (22) Spek, A. L. *J. Appl. Crystallogr.* **2003**, *36*, 7-13.
- (23) Wong-Foy, A. G.; Matzger, A. J.; Yaghi, O. M. *J. Am. Chem. Soc.* **2006**, *128*, 3494-3495.
- (24) Ma, B. Q.; Mulfort, K. L.; Hupp, J. T. *Inorg. Chem.* **2005**, *44*, 4912-4914.
- (25) Mulfort, K. L.; Hupp, J. T. *Inorg. Chem.* **2008**.
- (26) Mulfort, K. L.; Hupp, J. T. *J. Am. Chem. Soc.* **2007**, *129*, 9604-9605.
- (27) Cho, S.-H.; Ma, B.; Nguyen, S. T.; Hupp, J. T.; Albrecht-Schmitt, T. E. *Chem. Commun.* **2006**, 2563-2565.
- (28) Gadzikwa, T.; Zeng, B.-S.; Hupp, J. T.; Nguyen, S. T. *Chem. Commun.* **2008**, 3672-3674.
- (29) Sing, K. S. W.; Everett, D. H.; Haul, R. A. W.; Moscou, L.; Pierotti, R. A.; Rouquerol, J.; Siemieniewska, T. *Pure Appl. Chem.* **1985**, *57*, 603-619.
- (30) Li, D.; Kaneko, K. *Chem. Phys. Lett.* **2001**, *335*, 50-56.

- (31) Breck, D. W. *Zeolite Molecular Sieves*; John Wiley & Sons: New York, 1974.
- (32) Lozano-Castello, D.; Cazorla-Amoros, D.; Linares-Solano, A. *Carbon* **2004**, *42*, 1233-1242.
- (33) Walton, K. S.; Millward, A. R.; Dubbeldam, D.; Frost, H.; Low, J. J.; Yaghi, O. M.; Snurr, R. Q. *J. Am. Chem. Soc.* **2008**, *130*, 406-407.
- (34) Banerjee, R.; Phan, A.; Wang, B.; Knobler, C.; Furukawa, H.; O'Keeffe, M.; Yaghi, O. M. *Science* **2008**, *319*, 939-943.
- (35) Caskey, S. R.; Wong-Foy, A. G.; Matzger, A. J. *J. Am. Chem. Soc.* **2008**, *130*, 10870-10871.
- (36) Llewellyn, P. L.; Bourrelly, S.; Serre, C.; Vimont, A.; Daturi, M.; Hamon, L.; De Weireld, G.; Chang, J.-S.; Hong, D.-Y.; Kyu Hwang, Y.; Hwa Jhung, S.; Ferey, G. *Langmuir* **2008**, *24*, 7245-7250.
- (37) Millward, A. R.; Yaghi, O. M. *J. Am. Chem. Soc.* **2005**, *127*, 17998-17999.
- (38) Wang, B.; Cote, A. P.; Furukawa, H.; O'Keeffe, M.; Yaghi, O. M. *Nature* **2008**, *453*, 207-211.
- (39) Kondo, A.; Noguchi, H.; Carlucci, L.; Proserpio, D. M.; Ciani, G.; Kajiro, H.; Ohba, T.; Kanoh, H.; Kaneko, K. *J. Am. Chem. Soc.* **2007**, *129*, 12362-12363.
- (40) Seki, K. *Phys. Chem. Chem. Phys.* **2002**, *4*, 1968-1971.
- (41) Langmuir, I. *J. Am. Chem. Soc.* **1918**, *40*, 1361-1403.
- (42) Gould, S. L.; Tranchemontagne, D.; Yaghi, O. M.; Garcia-Garibay, M. A. *J. Am. Chem. Soc.* **2008**, *130*, 3246-3247.
- (43) Winston, E. B.; Lowell, P. J.; Vacek, J.; Chocholousova, J.; Michl, J.; Price, J. C. *Phys. Chem. Chem. Phys.* **2008**, *10*, 5188-5191.

- (44) Dubbeldam, D.; Walton, K. S.; Ellis, D. E.; Snurr, R. Q. *Angew. Chem. Int. Ed.* **2007**, *46*, 4496-4499.

Appendix A. CO₂ adsorption of 9 and 9-M

A. Overview

The adsorption studies performed on structure **9** in Chapter 5 strongly suggest that in a highly catenated structure, framework reduction does indeed enhance H₂ uptake, but through structural effects rather than increasing H₂ heat of adsorption. To further explore how structure changes with framework reduction and effects H₂ uptake, structural parameters such as the micropore volume and pore size distribution are effective tools for understanding H₂ interactions in these complex materials. Unfortunately, we were unable to obtain satisfactory nitrogen adsorption data for the **9·M** samples at the very low adsorbate loading required for determination of micropore volumes.¹ Consequently, we repeated the isotherm measurements at 273K, substituting CO₂ for nitrogen.² Data were fit via the NLDFT method³ and yielded the micropore volumes and surface areas shown in Table A.1. Little difference in micropore volume is evident for the parent versus framework-reduced materials.

From the CO₂ isotherms themselves (Figure A.1) only very small differences in uptake are evident. As one would expect, these translate into only small differences in NLDFT surface areas for **9** vs. **9·Li**, **9·K**, or **9·Na** (Table A.1). This suggests that at the comparatively high temperature used for CO₂ measurements, sufficient thermal energy may be available to displace interwoven frameworks and enhance surface areas even without the assistance of strut reduction and cation incorporation. Comparison of absolute surface areas for N₂ (77K) versus CO₂ (273K) seems to support the suggestion. While the differences are relatively large, we note that measurements at 273K routinely return higher surface areas for microporous surface areas than do measurements at 77K. The explanations include: a) enhanced framework mobility at 273K, resulting in access to otherwise obstructed pores,⁴ and b) partial pore blocking at 77K, due to N₂ condensation and strong adsorption at channel bottlenecks.⁵

Table A.1 Summary of CO₂ and H₂ adsorption measurements for **9** and **9·M**.

	M / Zn ^[a]	M / diPyTz	Surface area (m ² /g) ^[b]	NLDFT micropore volume (cm ³ /g) ^[c]	H ₂ wt% ^[d]
9	0.00	0.00	801	0.25	1.12
9·Li	0.05	0.10	868	0.27	1.46
9·Na	0.12	0.24	822	0.24	1.60
9·K	0.07	0.14	779	0.22	1.51

[a] Determined by ICP analysis. [b] NLDFT derived surface area from CO₂ isotherm at 273K. [c] Calculated from NLDFT analysis of CO₂ isotherm at 273K. [d] 77K, 1atm.

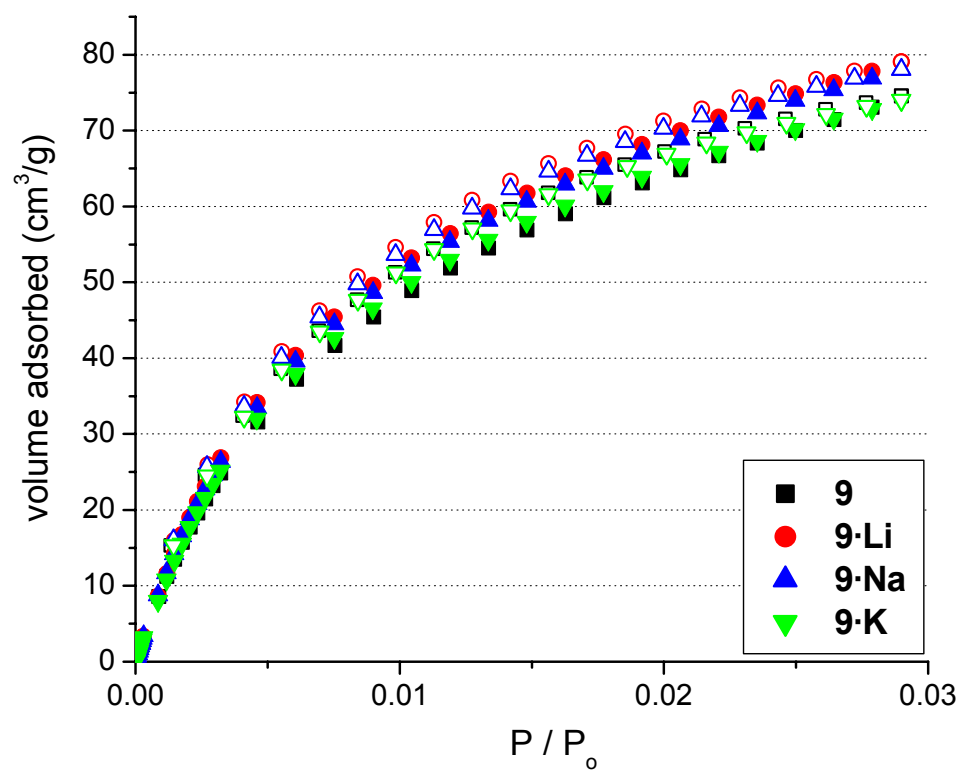


Figure A.1. 273K CO₂ adsorption isotherms of **9** and **9·M**.

Also, the comparatively small differences between NLDFT surface area and total uptake in the CO₂ isotherms is a further evidence of the conclusion that the dopant cations are completely shielded from incoming adsorbate molecules. CO₂ has a fairly strong quadrupole moment that can interact specifically with highly charged surfaces. The surface of the pristine **9** is fairly heterogeneous, but the presence of accessible alkali-metal cations would certainly alter the total uptake of CO₂ between **9** and **9·M**. To further verify the lack of specific CO₂-framework or CO₂-cation interactions in **9** and **9·M**, we measured CO₂ adsorption at 273K and 283K and calculated the isosteric heat of adsorption, see Figure A.2.

The isosteric CO₂ heat of adsorption for **9** and **9·Li** was calculated in the same manner as that for H₂ (see Chapter 2.2.6).⁶ If there were special sites accessible to incoming CO₂ adsorbate molecules, there would be a significantly larger Q_{st} value at very low loading (N = 0). Therefore, the NLDFT analysis can be employed to analyze the low-pressure CO₂ adsorption isotherms and compare the structural parameters between the neutral and doped materials.

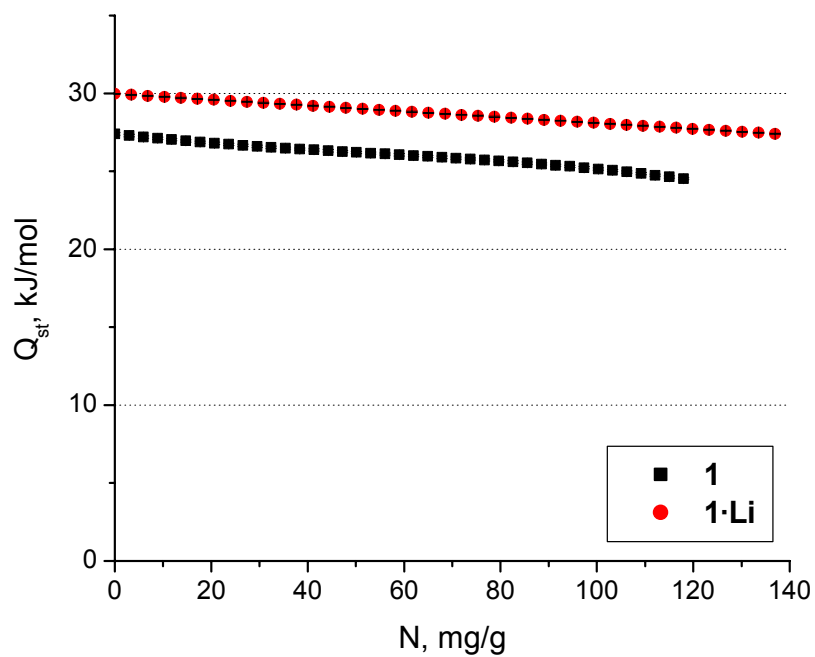


Figure A.2. Isosteric CO₂ heat of adsorption of **9** and **9·Li**.

Appendix A References

- (1) Dubinin, M. M.; Stoeckli, H. F. *J. Colloid Interface Sci.* **1980**, *75*, 34-42.
- (2) Lozano-Castello, D.; Cazorla-Amoros, D.; Linares-Solano, A. *Carbon* **2004**, *42*, 1233-1242.
- (3) Jagiello, J.; Thommes, M. *Carbon* **2004**, *42*, 1227-1232.
- (4) Chen, B.; Zhao, X.; Putkham, A.; Hong, K.; Lobkovsky, E. B.; Hurtado, E. J.; Fletcher, A. J.; Thomas, K. M. *J. Am. Chem. Soc.* **2008**, *130*, 6411-6423.
- (5) Noro, S.-i.; Kitaura, R.; Kitagawa, S.; Akutagawa, T.; Nakamura, T. *Inorg. Chem.* **2006**, *45*, 8990-8997.
- (6) Czepirski, L.; Jagiello, J. *Chem. Eng. Sci.* **1989**, *44*, 797-801.

KAREN L. MULFORT

Northwestern University, Department of Chemistry
2145 Sheridan Road, Evanston, IL 60208
email: k-mulfort@northwestern.edu

EDUCATION**Ph.D. Candidate, Materials Chemistry**

December 2008

Northwestern University, Evanston, IL

Research Advisor: Professor Joseph T. Hupp

*Metal-Organic Frameworks as Hydrogen Storage Materials:**Effects of Framework Reduction and Cation Doping***B.S. Chemistry and Bachelor of Chemical Engineering**

May 2001

University of Minnesota, Minneapolis, MN

EXPERIENCE**Laboratory Graduate Fellow**

2005-present

Argonne National Laboratory, Chemistry Division, Argonne, IL

Fellowship Advisor: Dr. David M. Tiede

Fellowship Research: Structurally characterize solution-phase supramolecular assemblies via solution X-ray scattering techniques with synchrotron radiation at the Advanced Photon Source.

Research Assistant

2003-present

Northwestern University, Department of Chemistry, Evanston, IL

Research Advisor: Professor Joseph T. Hupp

Thesis Research: Design and synthesize permanently porous metal-organic frameworks to function as hydrogen storage materials. Characterization of porous materials by single crystal structure determination, powder X-ray diffraction, thermal characterization, elemental analysis, and low-pressure gas adsorption measurements and analysis.

Staff Chemist

2001-2003

Elecon, Inc., Chelmsford, MA

Develop high quality conducting polymer resins and coating formulations for use in electronic devices such as OLEDs, PLEDs, touch screens, electrochromic windows, and flexible displays.

Technical Aide

1999-2001

3M, Advanced Materials Technology Center, St. Paul, MN

Synthesize and evaluate high performance inkjet imaging materials using several technologies including polymer melt processing, twin-screw extrusion, print testing and microscopy.

PUBLICATIONS

K. L. Mulfort, T. M. Wilson, M. R. Wasielewski, J. T. Hupp. Framework Reduction and Alkali-Metal Doping of a Triply Interpenetrating Metal-Organic Framework Enhances H₂ Uptake, *Langmuir*, **2008**, *submitted*.

O. K. Farha, A. M. Spokoyny, K. L. Mulfort, C. A. Mirkin, J. T. Hupp. Gas Sorption Properties of Cobalt(II) Carborane-Based Coordination Polymers as a Function of Morphology, *Angew. Chem. Int. Ed.*, **2008**, *submitted*.

O. K. Farha, K. L. Mulfort, J. T. Hupp. Node-based Post-Assembly Modification of a Hydrogen-Sorbing Metal-Organic Framework Material, *Inorg. Chem.*, **2008**, *submitted*.

S. J. Lee, S. H. Cho, K. L. Mulfort, D. M. Tiede, S. T. Nguyen, J. T. Hupp. Coordinative Self-Assembly of Supramolecular Porphyrin Catalytic Boxes for Selective Oxidation, *J. Am. Chem. Soc.*, **2008**, *in press*.

Y. S. Bae, K. L. Mulfort, H. Frost, P. Ryan, S. Punathanam, L. J. Broadbelt, J. T. Hupp, R. Q. Snurr. Separation of CO₂ from CH₄ Using Mixed-Ligand Metal-Organic Frameworks, *Langmuir*, **2008**, *24*, 8592-8598.

K. L. Mulfort, J. T. Hupp. Alkali Metal Cation Effects on H₂ Uptake and Binding in Metal-Organic Frameworks, *Inorg. Chem.*, **2008**, *47*, 7936-7938. *Cover feature*

O. K. Farha, K. L. Mulfort, A. M. Thorsness, J. T. Hupp. Separating Solids: Purification of Metal-Organic Framework Materials, *J. Am. Chem. Soc.*, **2008**, *130*, 8598-8599.

S. J. Lee, K. L. Mulfort, X. Zuo, A. J. Goshe, P. J. Wesson, J. T. Hupp, D. M. Tiede. Coordinative Self-Assembly and Solution-Phase X-ray Structural Characterization of Cavity-Tailored Porphyrin Boxes, *J. Am. Chem. Soc.*, **2008**, *130*, 836-838.

O. K. Farha, A. M. Spokoyny, K. L. Mulfort, M. F. Hawthorne, C. A. Mirkin, J. T. Hupp. Synthesis and Hydrogen Adsorption Properties of Carborane-Based Metal-Organic Framework Materials, *J. Am. Chem. Soc.*, **2007**, *129*, 12680-12681.

K. L. Mulfort, J. T. Hupp. Chemical Reduction of Metal-Organic Frameworks as a Method to Enhance Gas Uptake and Binding, *J. Am. Chem. Soc.*, **2007**, *129*, 9604-9605.

S. J. Lee, K. L. Mulfort, J. L. O'Donnell, X. Zuo, A. J. Goshe, S. T. Nguyen, D. M. Tiede, J. T. Hupp. Supramolecular Porphyrinic Prisms: Coordinative Assembly and Solution-phase X-ray Structural Characterization, *Chem. Commun.*, **2006**, *44*, 4581-4583.

B.-Q. Ma, K. L. Mulfort, J. T. Hupp. Microporous Pillared Paddle-Wheel Frameworks based on Mixed Ligand Coordination of Zinc Ions. *Inorg. Chem.*, **2005**, *44*, 4912-4914.

K. L. Mulfort, J. Ryu, Q. Y. Zhou. Preparation of Surface Initiated Polystyrenesulfonate Films and PEDOT Doped by the Films. *Polymer* **2003**, *44*, 3185-3192.

PATENT ACTIVITY

J. T. Hupp, K. L. Mulfort, Y. S. Bae, R. Q. Snurr. Mixed-Ligand Metal-Organic Frameworks for the Separation of CO₂ from CH₄, **2008**, provisional patent.

C. A. Mirkin, A. M. Spokoyny, K. L. Mulfort, J. T. Hupp, O. K. Farha. Metal-Organic Framework Materials Based on Icosahedral Boranes and Carboranes, **2007**, provisional patent.

Q. Zhou, J. Ryu, D. Freitag, K. Mulfort. Compositions Produced by Solvent Exchange Methods and Uses Thereof, **2003**, patent pending, application 20030164477.

HONORS AND AWARDS

Argonne National Laboratory Director's Postdoctoral Fellowship, 2008

Margaret C. Etter Student Lecturer Award, American Crystallographic Association, 2008

Intl. Center for Materials Research Summer School on Porous Materials, UCSB, August 2006

Argonne National Laboratory Lab-Grad Fellowship, August 2005-present

Argonne National Laboratory Summer School on Neutron and X-ray Scattering, August 2005

Presidential Scholarship, University of Minnesota—Twin Cities, 1997-2001

PRESENTATIONS

Poster. Karen L. Mulfort, David M. Tiede, Joseph T. Hupp. Metal-Organic Architectures for Energy Storage and Conversion. Postdoctoral Research Symposium, Argonne National Laboratory, September 2008.

Invited Oral. Karen L. Mulfort, Suk Joong Lee, David M. Tiede, Joseph T. Hupp. Solution X-ray Scattering: Characterization of Supramolecular Porphyrin Assemblies. American Crystallographic Association, Knoxville, TN, June 2008.

Invited Oral. Karen L. Mulfort, Suk Joong Lee, David M. Tiede, Joseph T. Hupp. Small-Angle X-ray Scattering of Metalloporphyrin Assemblies in Solution. APS User Meeting, Argonne, IL, May 2008.

Invited Oral. Karen L. Mulfort. Metal-Organic Architectures for Energy Storage and Conversion. Chemical Sciences and Engineering Division Seminar, Argonne National Laboratory, March 2008.

Poster. Karen L. Mulfort, Suk Joong Lee, David M. Tiede, Joseph T. Hupp. Solution Phase X-ray Scattering: Characterization of Supramolecular Porphyrin Assemblies. Japan-USA Joint Symposium on Chemistry of Coordination Space, Evanston, IL, June 2007.

Poster. Karen L. Mulfort, Joseph T. Hupp. Mixed-Ligand Metal-Organic Frameworks for Hydrogen Storage. 233rd ACS national meeting, Chicago, IL, March 2007.

Poster. Karen L. Mulfort, Joseph T. Hupp. Design and Synthesis of Metal-Organic Frameworks for Hydrogen Storage. International Center for Materials Research, Summer School on Porous Materials, UCSB, August 2006.

PROFESSIONAL AFFILIATIONS

American Chemical Society, Division of Inorganic Chemistry
Phi Lambda Upsilon National Chemistry Honor Society